Mitigation of Metal Dust Deflagrations via Thermal Analysis and Active Explosion Suppression

By
© 2019
Nicholas Reding

Submitted to the graduate degree program in Chemical and Petroleum Engineering Department and the Graduate Faculty of the University of Kansas in partial fulfillment of the requirements for the degree of Master of Science.

Chair: Mark B. Shiflett

Aaron M. Scurto

Alan M. Allgeier

Date Defended: 25 November 2019

The thesis committee for Nicholas Reding certifies that this is the approved version of the following thesis:

Mitigation of Metal Dust Deflagrations via Thermal Analysis and Active Explosion Suppression

_____

Chair: Mark B. Shiflett

Date Approved: 25 November 2019

Abstract

Explosions induced by ignition of combustible metal powders continue to present a significant threat to metal handling and refining industries. Addition of non-combustible inert material to combustible dust mixtures, either through pre-mixing or high-rate injection as the incipient flame front begins to develop, is common practice for preventative inhibition or explosion protection via active suppression, respectively.

Metal dusts demonstrate an extremely reactive explosion risk due to amplified heat of combustion, burning temperature, flame speed, explosibility parameters (K_{St} and P_{max}), and ignition sensitivity. Upon ignition in a contained enclosure volume and propagation to interconnected vessels, metal dusts exhibit augmented explosion severity relative to organic fuels. Inhibition efficiency of suppressant agents utilized for active mitigation is shown to be reliant on fuel explosibility, discrete burning mechanism, and combustion temperature range, and thus may be increasingly variable depending on the fuel in question. For this reason, mitigation of metal powder deflagrations at moderate total suppressed pressures (relative to the overall strength of the enclosure) and at low agent concentrations remains challenging.

The aim of this study is to propose a method for the characterization of the inhibition efficiency of five suppressant agents (sodium bicarbonate [SBC], potassium bicarbonate [PK], monoammonium phosphate [MAP], diammonium phosphate [DAP], and sodium chloride-based [Met-L-X]) when mixed with both organic (cornstarch) and metallic (zinc and iron) fuels, utilizing simultaneous thermal analysis (STA) techniques. In addition, this work validates lab-scale conclusions through metal dust suppression testing in Fike Corporation's 1 m^3 sphere combustion chamber and evaluates the efficacy of suppression agents with anticipated performance for the mitigation of iron and aluminum powder deflagrations.

Dedicated to my fiancé for her inspiring dedication,

And to my family for their constant love and unwavering support.

Acknowledgments

Above all, I would like to thank Dr. Mark Shiflett for his mentorship and for continuing to push me beyond the self-imposed limits of what I thought myself capable.

I would also like to express gratitude towards the entire faculty and staff of the Department of Chemical and Petroleum Engineering at the University of Kansas. This project distinguishes the efforts of Rachel Speckin, Edward Reyes, and David Treviño for their experimental contributions, as well as the efforts of Dr. David Minnick for his invaluable assistance with thermal analytical instrument training, calibration, and troubleshooting. Gilbert Ortiz is also recognized for the design and creation of remarkable graphics for journal cover art positions.

Additionally, I would like to acknowledge both the assistances of NETZSCH (Melinda Tucker and Mike Hsu) in providing simultaneous thermal analysis for high burning temperature fuels and the vital contributions of Fike Corporation's remote site testing staff and combustion test lab technicians in conducting open-air dispersion testing, fuel explosibility analysis, and 1 m^3 sphere active suppression experiments. I gratefully recognize the support of Fike Corporation in providing operational resources, continued funding of the test program, and consent to publish the results of this work.

Lastly, I would like to thank my family and my fiancé, Monia, for their unceasing support and reassurances. You have been my biggest advocates and have given me the strength to surpass all hurdles along my journey. I love you all deeply.

Additional Acknowledgements

Portions of this thesis have been previously published as articles in journals by the American Chemical Society (ACS). The publishers allow the author to reuse published works in the author's thesis which the author writes and is required to submit to satisfy the criteria of degree-granting institutions.

Portions reused from:

1. Reding, N. S.; Shiflett, M. B. Metal Dust Explosion Hazards: A Technical Review. *Ind. Eng. Chem. Res.* **2018**, *57* (34), 11473-11482. DOI: 10.1021/acs.iecr.8b02465
2. Reding, N. S.; Shiflett, M. B. Characterization of Thermal Stability and Heat Absorption for Suppressant Agent/Combustible Dust Mixtures via Thermogravimetric Analysis/Differential Scanning Calorimetry. *Ind. Eng. Chem. Res.* **2019**, *58* (11), 4674-4687. DOI: 10.1021/acs.iecr.8b06143
3. Reding, N. S.; Farrell, T.; Jackson, R.; Taveau, J.; Shiflett, M. B. Mitigation of Iron and Aluminum Powder Deflagrations Via Active Explosion Suppression in a 1 m^3 Sphere Vessel. *Ind. Eng. Chem. Res.* **2019**, *58* (38), 18007-18019. DOI: 10.1021/acs.iecr.9b04021

Table of Contents

List of Figures

List of Tables

Chapter 1: Introduction

1.1. Recent Metal Dust Explosion Incidents

Metal dust deflagrations continue to pose a critical threat towards plant safety. Upon ignition of a dispersed metal dust cloud containing sufficient oxidizer, serious dust explosions can occur, with extensive loss to life and property. Prominent growth in metal refining, processing, and storage industries demands for the development of more effective methods and materials for suppressing metal dust explosions. To fully appreciate the severity of such unpredictable hazards, this work begins with a general review of combustible metal dust deflagration incidents and resultant explosions.

Ignition of suspended combustible metal dust clouds remains an acute risk toward personnel and pneumatic conveyance equipment within an extensive range of metal refining and processing industries. As reported by a Chemical Safety Board (CSB) investigation on combustible dust hazards, there have been more than 281 combustible dust incidents within the United States between 1980 and 2005, resulting in 119 fatalities and 718 injuries to operating personnel. Due to the heightened ignition sensitivity and reactivity of many metal dust clouds in air, metallic fuels have contributed to a noticeable proportion of these statistics. According to the CSB's tabulation of these occurrences, dusts of metallic nature have accounted for approximately 20% of these 281 explosion incidents.[1] In more recent years, metal dust explosions have continued to exhibit catastrophic intensity. At the Hayes Lemmerz International-Huntington, Inc. facility in Indiana in 2003, ignition and flame propagation within an aluminum scrap dust collection equipment line led to one fatality and several injuries.[2] In December of 2010, AL Solutions, Inc. of New Cumberland, WV experienced a severe metal dust explosion following frictional heating within a defective zirconium blender unit, ultimately causing three fatalities and one serious injury.[3] Over a six month

period in 2011, the coupled effects of three separate iron powder flash fires and hydrogen explosions at the Hoeganaes scrap metal processing facility in Gallatin, TN resulted in five deaths and three injuries.[4] Another considerably more devastating incident occurred at an industrial metal polishing plant in Kunshan, China in 2014. Poor plant housekeeping and inadequate isolation techniques led to a succession of consecutive aluminum-alloy explosions and caused 146 fatalities, 114 injuries, and 351 million yuan (51 million USD) in direct economic losses.[5]

1.2. Combustion Fundamentals

In the presence of an oxidizer, combustion releases a variety of products depending on the fuel in question. Organic fuel decomposition during oxidative reactions yields predictable products including carbon dioxide, water vapor, and heat. Reaction R1 utilizes a simple sugar complex as an example of an organic dust combustion. Upon ignition under oxygen (O_2), pure metal dusts typically react to produce large quantities of heat and the respective metal oxide component. Reaction R2 utilizes magnesium as a metal combustion example.

$$C_{12}H_{22}O_{11} + 12O_2 \rightarrow 12CO_2 + 11H_2O + Heat \quad \text{(R1)}$$

$$2Mg + O_2 \rightarrow 2MgO + Heat \quad \text{(R2)}$$

Regardless of the fuel type, in order for an explosion to occur, there are several universal criteria that must be met: (1) combustible dust is present, (2) oxidizing agent is present (O_2 in air), (3) fuel is lofted (dispersed) in suspension, (4) adequate ignition source is available to initiate the reaction, and (5) combustion occurs in a contained enclosure. This concept, also known as the 'Explosion Pentagon', is shown in Figure 1.1. Expanding on these conditions, the fuel concentration must be within the upper and lower explosibility limits, and the particle size distribution must be able to support flame propagation. According to the stoichiometry of the

reaction mechanism, the atmosphere must provide sufficient oxygen to sustain combustion. Propagation of the combustion zone (flame front) through the unreacted medium at a velocity less than the speed of sound is referred to as a deflagration. If allowed to accelerate to velocities greater than the speed of sound, detonation occurs. Deflagration growth within a confined volume is required to produce the pressure effects associated with an explosion. Removal of any one of these five elements is enough to impede initiation of an explosion event.

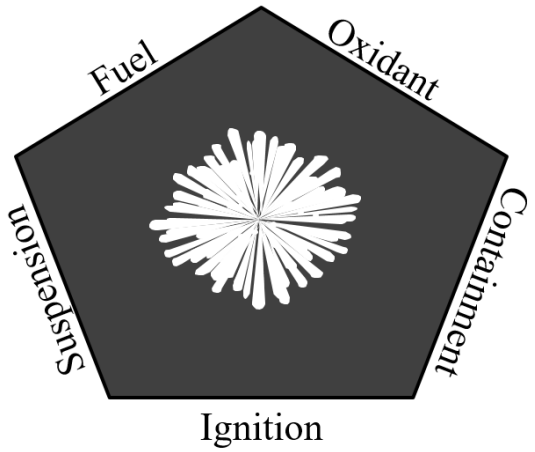

Figure 1.1. Explosion Pentagon

The severity or intensity of an explosion can be assessed from a fuel's explosibility index (K_{St}) as depicted in Table 1.1.

Table 1.1. Hazard Classifications for Combustible Dust Explosions[6]

K_{St} Range [barg-m/s]	Classification	Relative Intensity
$K_{St} = 0$	St_0	Non-combustible
$0 < K_{St} < 200$	St_1	Weak
$200 < K_{St} < 300$	St_2	Strong
$300 < K_{St}$	St_3	Very strong

Scaled by enclosure volume, K_{St} is directly proportional to the maximum rate of pressure rise as demonstrated by Equation E1:

$$K_{St} = \left(\frac{dP}{dt}\right)_{max} x\ V^{1/3} \quad \text{(E1)}$$

The maximum pressure observed during contained, unprotected combustion (P_{max}) represents another explosibility parameter. K_{St} and P_{max} correlate to the combustion kinetics and thermodynamics, respectively, for a given fuel. However, the reader must keep in mind that this cube root law (equation E1) may have limited validity in some cases. Accuracy of results for a certain fuel demand the following to be true: enclosures (test vessel and process vessel in which the fuel is conveyed) must be geometrically comparable, thickness of the flame front must be insignificant in comparison to the enclosure radius, and the burning rate as a function of temperature and pressure must be uniform in all considered volumes. Fuels of the same composition may exhibit varying explosibility due to differences in injection turbulence, moisture content, and effective particle size (specific surface area).[6]

Fuel combustion propagation mechanisms are complex and are unsteady in most industrial application settings. Although some metals (such as iron) combust in solely the solid-phase (homogeneous combustion), other metallic flame propagations with extensive heats of combustion and flame temperatures experience multi-phase decomposition. In such a heterogeneous environment, the fuel particulate first begins to absorb energy through conductive, convective, and/or radiative heat transfer methods. Following melting and vaporization of the fuel, the coexisting phases of the metal particle mix with available oxidizing molecules, leading to ignition and burning of the fuel. Once this fuel source has been exhausted, flame extinction occurs and preheating of subsequent particles begins as the flame front develops further. As observed by Gao et al., there are two types of flame propagation mechanisms relevant in dust explosions: kinetics-controlled propagation and devolatilization-controlled propagation.[7] Combustion has the potential to transition from one regime to another, depending on variances in bulk volatility or particle size. Metal dust flames are able to propagate via surface reactions, pre-volatilization, or both.

Upon ignition of a suspended dust cloud, metal dust fuels are capable of generating exceedingly high flame temperatures and substantial rates of pressure rise. Reding and Shiflett describe the full extent of the complexities and spontaneity associated with sustained metal dust combustion in a recent review article.[8] Taveau further illustrates the distinct combustion characteristics of metallic fuels and comments on the resultant challenges in designing effective explosion protection solutions.[9] As shown in a multitude of extensive comprehensive works, metal dust combustion regimes are considered to be extremely dangerous hazards unless proper prevention and/or protection techniques are established.[6,10] The overarching goal for any plant safety engineer would ideally be to prohibit combustion altogether, effectively eliminating the risk of explosion completely. Section 1.3 will begin with discussion of methods for explosion prevention for metal dust conveyance processes.

1.3. Review of Current Explosion Prevention Techniques

1.3.1. Housekeeping

The risk of primary explosions within process equipment remains high when the five criteria of the explosion pentagon (shown in Figure 1.1) are met. The initial deflagration event generates a pressure front which can disturb settled dust that has accumulated on the floor and other horizontal surfaces. Once this dust buildup is lofted and ignited, a chain reaction of secondary explosions can occur. One key finding from the hazard study performed by the CSB from 1980 to 2005 was as follows: “Secondary dust explosions, due to inadequate housekeeping and excessive dust accumulations, caused much of the damage and casualties in recent catastrophic incidents.”[1]

Dust layer accumulation has quite an important influence on the amount of dust able to be suspended. According to studies carried out by Eckhoff, a one-millimeter layer of dust with a bulk

density of 500 kg/m^3 is capable of generating a 100 g/m^3 dust cloud if fully dispersed through a room five meters in height. Partial dispersion up to only one meter can produce a lofted concentration of 500 g/m^3, as illustrated in Figure 1.2.[6] Based on this analysis, it is clear that it takes very little accumulation to reach minimum explosible concentrations if lofted properly. Therefore, suitable housekeeping techniques (such as preventing dust leaks, effectively utilizing dust collection units, and eliminating flat surfaces where dust can collect) are vital towards reducing the risk for secondary explosions.

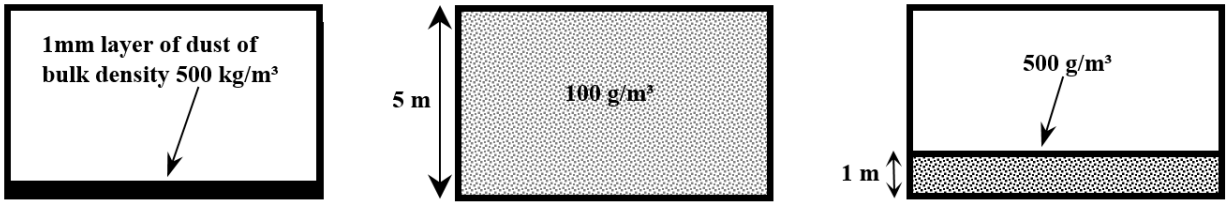

Figure 1.2. Hazard Potential for thin layers of dust accumulation

Assuming combustible material cannot be reliably contained within process equipment during operations, the National Fire Protection Agency (NFPA) provides guidance on appropriate strategies to maintain housekeeping standards. For example, NFPA 654 offers direction on preventive housekeeping practices such as recommended cleaning frequency, proper cleaning methods, and requirements for portable vacuum usage.[11] According to NFPA 484, however, metal particulate fuels require a more refined approach. In addition to covering the housekeeping measures as depicted in NFPA 654 for organic dusts, NFPA 484 guides the user to refrain from water-based cleaning in areas exposed to alkali or highly reactive metal particulates.[12] Even trace amounts of moisture cause concerns when dealing with such materials. Effects of particle moisture content and aggressive reactivity of burning metals with water will be discussed in detail in Section 2.1.3 and 2.2.3, respectively.

1.3.2. Ignition Control

According to the explosion requirements described in Section 1.2, a dispersed combustible dust will only begin to burn once it has been subjected to an ignition source with sufficient energy. Removal of such ignition sources can eliminate the risk of explosions; however, depending solely on ignition source prevention methods is unreliable for fuels with low minimum ignition energies (<10 mJ), as is the case with certain reactive metals. For many hydrocarbon dusts with higher minimum ignition energies, the control of potential ignition sources can have a positive impact on internal risk hazard analysis. Exposure to the following ignition sources can be largely avoided by mandating proper workplace standards and enforcing modifications to existing process operations:[6]

- Open flames (smoking, welding, etc.)
- Hot surfaces due to process overheating or inadequate cooling mechanisms
- Self-heating and smoldering nests (porous dust deposits may contain oxidation pockets, generating a high temperature internal reaction zone)
- Exothermic decomposition reactions (release of combustible volatiles)
- Heat produced through mechanical impact (sparks induced by abrupt metal/metal contact)
- Electrical failure and/or electrostatic discharge

Taking precaution regarding the ignition sources mentioned above will not completely guarantee that fire or explosion will not occur. With that said, a firm stance on process safety principles, such as grounding all process equipment or establishing intrinsically safe electrical components, is, nevertheless, a noteworthy facet to a thorough prevention design.

1.3.3. Inerting with Non-Flammable Gas

Gas inerting is often utilized as a technique to prevent the formation of an explosive atmosphere by lowering the volume percentage of oxidant within a given operation. Assuming that

there are no compatibility concerns between the purge gas and the conveyed process media, introduction of inert gases such as nitrogen (N_2), carbon dioxide (CO_2), or conditioned flue gases into an enclosed process volume can effectively quench the continuance of combustion oxidation reactions. The system should be properly designed to maintain oxidant concentrations low enough that the dust cloud is unable to sustain flame propagation, even if all other criteria of the explosion pentagon (as illustrated in Figure 1.1) are satisfied. The degree to which the oxygen content must be limited is dependent on both the ignition energy provided and the fuel being conveyed. This correlation was studied in further detail by Schwenzfeuer et al., who developed fitted relationships for limiting oxygen content (LOC) within an enclosed atmosphere as a function of ignition source capacity and fuel minimum ignition energy (MIE).[13]

As one might anticipate, the severity and sensitivity rise with increasing oxygen content of the gas in which the fuel is processed. This trend continues until saturation is reached, at which point O_2 is in excess. This relationship is presented by Eckhoff for various metal fuels and for organic carbon, as shown in Figure 1.3.[6,14]

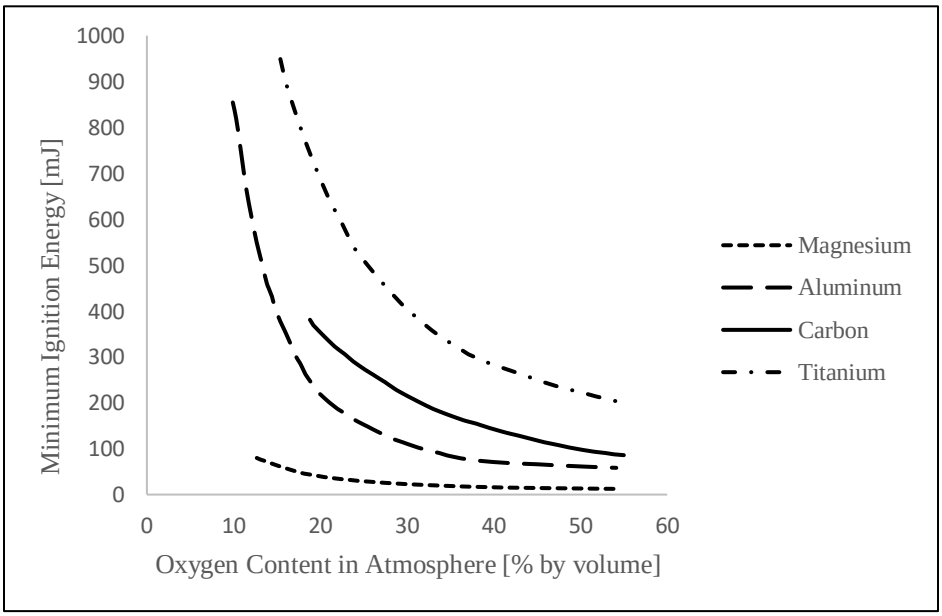

Figure 1.3. Minimum ignition energy as a function of oxygen content for dust clouds of various fuels (mean particle size: 40 µm, initial pressure: 0.2 bar, equivalence ratio: 0.65, MIE defined for 80% ignition probability).[6]

As oxygen content decreases, the corresponding rate of rise of the MIE increases accordingly. The curves for aluminum and titanium most clearly demonstrate this consequence. Oxygen content nears the lower threshold for sustained flame propagation, making the energy requirements of ignition progressively higher.

Despite the clear benefits, gas inerting has some drawbacks. The cost of purchasing the inert gas (or possibly conditioning of pre-existing process flue gas) may be too high to maintain on a large scale. Furthermore, gas inerting may pose unforeseen asphyxiation hazards to personnel in the operations area due to leaks or purges from the process. In addition, the selection of the proper inert gas for a specific application is another complication to consider. For example, nitrogen gas is usually appropriate for inerting of aluminum explosion hazards, but rare inert gases such as argon or helium are required for inerting of magnesium dust to prevent nitride formation. For dust storage applications with a larger than normal bulk volume (silos, bins, or hoppers), an inert gas with low permeation may be unsuccessful at preventing the occurrence of internal smoldering combustion zones.[6]

1.3.4. Inerting with the Addition of Non-Combustible Dust

Another form of inerting, known as substitution, involves rendering a combustible mixture non-ignitable through addition of a non-combustible dust. This process essentially allows for control of the mixture composition in order to retain non-combustible bulk properties and keep dust cloud fuel concentrations saturated with solid inertant. If a hazardous material cannot be completely removed or replaced from the process, this approach could act as a viable alternative. Completed in a 20 L sphere test vessel, a case study performed by Myers depicts a significant reduction in ignition sensitivity when flame-retardant material was added to fine aluminum buffing

residue.[15] Ignition sensitivity compares properties of Pittsburgh Seam Coal (reference material) to properties of the dust in question, as shown in Equation E2:

$$Ignition\ Sensitivity = \frac{[MIExMITxMEC]_{Pittsburgh\ Seam\ Coal}}{[MIExMITxMEC]_{Test\ Dust}} \quad \text{(E2)}$$

where MIE represents the minimum ignition energy of a dust cloud, MIT represents the minimum ignition temperature of a dust cloud, and MEC represents the minimum explosible concentration of a dust cloud. As noticed by Myers, most impactful on the lowering of ignition sensitivity was the influence of the flame-retardant additive on the MIE and MIT. Compared to the unadulterated sample with recorded MIE of 34 mJ and MIT of 350°C, certain fuel/flame-retardant mixtures yielded MIE and MIT values as high as 452 mJ and 532°C, respectively. However, this analysis was performed on buffing pad residue which was largely organic, containing only trace aluminum content (<10% of the overall mixture). Due to the aggressive nature of metallic dusts, one would expect similar inerting studies on pure metals to return markedly different results. Miao et al. describes this through investigations of the inerting effect of calcium carbonate on the ignition characteristics (MIE and minimum auto-ignition temperature, MAIT) of metal dusts generated during machining operations. With minimum inerting criteria roughly set at MIE > 1000 mJ and MAIT > 450°C, this study witnessed the effective inerting of Fe alloy and Fe-Al alloy dust using 50% calcium carbonate by mass and the effective inerting of Al alloy dust using 75% calcium carbonate by mass. However, injection of calcium carbonate into pure atomized aluminum, atomized magnesium, or Mg-Al alloy did not demonstrate sufficient increase in MIE or MAIT to qualify successful minimization of ignition risk.[16] Fuels such as aluminum or magnesium are considered highly reactive metals and can be relatively difficult to inert in contrast to normally reactive metal fuels such as irons or other common alloy metals.

An alternate way to exploit non-combustible dusts for the inerting of hazardous metals is to introduce sizeable concentrations of a metal's corresponding metal-oxide, often through mild surface oxidation at low volume percentages of O_2. Oxide content decreases the overall reactivity of the mixture upon potential ignition at a later point by absorbing thermal energy away from a developing combustion. Baudry et al. demonstrates this through studies confirming the increase in ignition energies of commercial aluminum powder with increasing Al_2O_3 content (increase in oxide content from 0.46 wt % to 6.3 wt % yields a two-fold rise in required ignition energy).[17] As with aluminum powder, pure titanium can be characterized by comparable explosion severity and sensitivity. Yuan et al. illustrates the inerting effect of nano-TiO_2 powder on the MIT of nano and micro titanium dust clouds. The nano metal-oxide inert induced much greater increases in MIT (and equivalent decrease in sensitivity) when mixed with the micro titanium fuel particles.[18] Physical adsorption of the smaller nano-TiO_2 onto the surface of the larger micro titanium particles contributed to limited combustion kinetics by occupying active reaction sites. This substrate inhibition effect was likely not present in the nano-TiO_2/nano-Ti mixtures, as made apparent through minimal increases in MIT even at 90% metal-oxide concentrations.

Studies performed by Bernard et al. exhibit reduction in flame speed through aluminum dust clouds upon introduction of increasing Al_2O_3 concentrations. The flame velocity experienced an approximate 40% decrease (seemingly linear) when the ignited sample was subjected to mixing with 10 wt % oxide content.[19] A similar effect of decreased flame speed was observed (Gao et al.) for pure 30 μm size zirconium particles coated with iron oxide (Fe_2O_3).[20]

The applicability of chemical suppressants for explosion prevention and suppression of metal dust deflagrations was further investigated by Chatrathi and Going.[21] Monoammonium phosphate (MAP) and sodium bicarbonate (SBC) were ineffective at inerting aluminum ignition, even at

minimum inerting concentrations (MIC) as high as 2750 g/m^3. Upon injection of SBC and potassium bicarbonate (PK) into the combustion test vessel (1 m^3 sphere chamber) following ignition of suspended fuel, aluminum deflagrations (1750 g/m^3 fuel concentration) were suppressed at exceedingly saturated concentrations of agent (average total suppressed pressures as high as 2.08 barg [30.2 psig] at 4.54 kg/m^3 [10 lb/m^3] SBC concentration and 0.035 barg [0.5 psig] activation pressure).[21] Note that pressure is also denoted in gauge pressure units, as is common industry practice. The discussion on explosion protection through active suppression will end here, so as to not distract the reader from the primary directive of this section (prevention techniques). However, further research is required to properly characterize suppressant agents with greater affinity towards metal dust deflagration suppression. Mitigation of a deflagration through active suppression will be defined in detail within Section 1.4. Understanding of this topic (explosion protection through mitigation) will be vital toward the experimental analysis performed and discussed within Chapter 4.

These prevention techniques do not come without their disadvantages. Not only does this demand large quantities of what could be a costly inert material, but customers are typically unwilling to sacrifice the purity of their product through contamination with an inert. Depending on the tendency of the fuel to agglomerate, constant attention must be paid to ensure that the inert material and fuel are well-mixed. Differences in particle properties between the fuel and inert substances could lead to significant segregation, leaving some areas exposed to inert concentrations too low to properly impede ignition.[6]

Inherently safe process designs demand emphasis on the following key principles: minimization, substitution, moderation, and simplification. For metal dusts especially, institution

of such practices requires comprehensive diagnosis of the complexities associated with the hazard in question.

1.4. Inhibitor Properties and Explosion Mitigation Techniques

Inert additives prevent propagation of sustained deflagration through the protected volume via physical or chemical methods. Physical suppressants, such as rock dust, operate by absorbing both thermal and radiant energy from the developing deflagration and by diluting the fuel and oxygen content per unit volume. Energy removed from the ongoing combustion reaction significantly reduces the rate at which unburnt particles are preheated. As the concentration of physical inert increases, the system has less free energy available for unburnt fuel particles to preheat, thus impeding combustion growth and further propagation of the flame front. Depending on the composition of the inhibition material, thermal decomposition may additionally release water and inert gases (such as carbon dioxide emitted during calcium carbonate decomposition), which act as heat sinks and heighten the physical inerting mechanism. Chemical inhibition implies that the suppressant agent directly hinders the combustion reaction kinetically through disruption of branch chain reactions and detention of free combustion radicals, obstructing standard linear propagation of flame. Certain dry powder suppressant agents, such as sodium bicarbonate and monoammonium phosphate, allow for flame extinction via both physical and chemical means.[21]

The efficacy of a dust explosion inhibitor improves with equivalent increase in three key properties of the agent: specific heat capacity, thermal conductivity, and absorptivity.[22] Optimization of these factors allows for increased absorption of the heat and radiant energy generated during combustion, which limits heating of surrounding unburnt fuel particulates. Heat capacity at the particle level is closely related to the characteristics of the inertant chemical

composition; however, heat capacity on a bulk scale is directly proportional to the amount of inert introduced into the application. A higher concentration of inert material within the fuel/agent mixture effectively increases the heat capacity of the system. Thermal conductivity represents the rate at which heat is transferred by conduction through a unit cross-section of a given material, with greater inhibition performance corresponding to increased overall resistance to heat flow. The degree of heat absorptivity is a function of the inert particle surface area, with larger particle surface area promoting greater rates of heat absorption. Surface area itself is a function of both particle shape and size. Irregular, small-sized suppressant agent particles are identified as having greater surface areas. Following analysis of experiments with coal and rock dust mixtures (fuel and inhibitor, respectively) in a 20 L spherical vessel, Dastidar et al. conclude that decreased suppressant particle sizes yield a reduction in the MIC required to prevent initiation of oxidative combustion.[22] The aforementioned suppressant properties are applicable to the performance of all solid inhibitors. However, the effectiveness of the material for inerting or suppressive mitigation is also dependent on the properties of the fuel (combustible dust composition, fuel reactivity, particle size, degree of surface oxidation, and suspended concentration). This presents an issue when dealing with reactive metal dust fuels, which commonly exhibit extremely high adiabatic flame temperatures and significant heats of combustion.

In a separate review, Amyotte discusses complementary parameters influencing the efficacy of non-combustible dusts for the inerting (prevention) or suppression (mitigation) of dust explosions.[23] The variables under investigation include factors representative of the inert material (composition, particle size) and of the application (co-existence of flammable gas, ignition energy, size/geometry of combustion vessel). Even though the large-scale application factors indeed play a role in assessment of the agent's performance, it must be noted that the motivation for this paper

is to examine the effect of material composition on heat of absorption and combustion rate inhibition during fuel oxidation. Inertant powders with varying compositions have fundamental differences in their specific heats, heats of reaction, decomposition temperature range(s), and decomposition rates. As previously mentioned, certain inertant materials with high heat capacities act through physical mechanisms by absorbing thermal energy away from the developing deflagration and restraining continued propagation to other unburnt regions outside of the combustion zone. Depending on the onset of inert decomposition and rate of endothermic decomposition over a specific temperature range, certain inert materials may also exhibit improved performance due to extended "residence time" within the fuel combustion zone. This concept will act as the foundation for the theory of chemical inhibition effectiveness, on which much of the subsequent thermal analytical experiments were based (Chapter 3).

Active suppression involves the hindering of deflagration propagation by chemically participating in the combustion reaction and/or physically absorbing heat released from fuel oxidation. Introduction of inert material via active chemical suppression consists of timely, rapid injection of suppressant agent into the protected volume after ignition of the combustible dust cloud has occurred, with the objective of extinguishing the incipient flame front early in the deflagration development, thereby limiting the explosion pressure below the design strength of the vessel. The key stages of suppression system activation can be summarized as follows: (1) Ignition occurs, and the heat of combustion begins to develop pressure within the system. During suppression experiments, full payload of fuel is dispersed into suspension within the contained volume and ignited via chemical igniter. (2) As the deflagration develops, the resultant pressure growth is monitored. Pressure buildup is detected via electronic pressure transducer. Once set point pressures are achieved, system controller triggers high-rate injection and complete dispersion of

suppressant agent into the protected volume via responsive opening of a High-Rate Discharge (HRD) container pre-loaded with suppressant and pressurized under nitrogen. (3) The suppressant agent absorbs heat from the developing combustion, quenching the flame front and promptly limiting further pressure growth. Once released into the enclosure, the suppressant agent has primary functions of absorbing heat generated by the incipient explosion and of inerting the unburnt region of the suspended dust cloud. The maximum pressure observed within the vessel during a suppressed deflagration event is reported as the total suppressed pressure (TSP). Explosion protection application design practices require that the TSP be lower than the protected enclosure design strength in order to prevent rupture of the vessel during an event. All powder loading procedures, HRD container pressurization, and actuation firing mechanism will be discussed in experimental context within Chapter 4 (Section 4.1.1). This technique must be properly designed based on the appropriate capabilities of the hardware (time delay between detection and system activation, injection distribution profile, discharge rate, discharge duration, etc.) and is restricted by its specificity to the application in question.

The measured TSP acts as a direct indicator of the inhibition performance of the suppressant agent during deflagration mitigation and consists of the following components:

$$TSP = P_{act} + P_{N_2} + P_{comb} \tag{E3}$$

where P_{act} signifies the activation pressure (or system response set point) of the detector, P_{N_2} represents the pressure due to injection of nitrogen from the HRD container, and P_{comb} indicates the generation of combustion pressure between system activation pressure and complete extinction of the deflagration.

1.5. Scope of Work & Primary Objectives

Current design techniques for reactive metal deflagration suppression rely predominantly on physical heat absorption properties of the inert material. For industrial applications requiring protection, this suggests injection of conservatively high concentrations of suppressant agent into the protected volume, essentially over-designing the payload of inertant to compensate for the agent's lack of chemical inhibition effectiveness. As investigated by Reding and Shiflett through thermogravimetric and differential scanning calorimetry analysis of zinc powder oxidation, overlap of the fuel combustion temperature region and the agent decomposition range allows for increased consumption of free combustion radicals, amplified chemical inhibition effect, and increased absorption of fuel oxidation exotherms.[8] Greater degree of overlap results in a kinetically dampened combustion rate and inhibited volatilization of surrounding fuel particles in the preheat zone. Selection of inert materials with increased chemical inhibition could allow for lower agent concentrations required to achieve equivalent total suppressed pressures (TSPs) within the equipment being protected. However, depending on the exact composition of the metal fuel, combustion may occur in different phases (or more than one phase, as in the case of aluminum powder) and at variable temperature ranges. The objective of this study is to investigate the large-scale performance of five agents (SBC, PK, MAP, DAP, and Met-L-X) for the suppression of iron and aluminum dust deflagrations, thus potentially enabling development of more efficient mitigation solutions specifically tailored for certain types of metal dust fuels. Before generating a test plan for suppression experiments at scale, the likely hazards corresponding to metal powder deflagration propagation must be appropriately qualified. Chapter 2 offers complete analysis of the unique risks and characteristic hazards associated with metal powder combustion mechanisms.

Chapter 2: Metal Dust Combustion Hazards

2.1. Inherent Properties of Combustible Dusts (and their Impacts on Metal Explosibility)

If preventative measures cannot be exercised (or are carried out unsuccessfully), it is crucial that plant engineers fully comprehend the hazards involved with metal dust deflagrations. All combustible dusts have intrinsic properties (propagation behavior, particle size, moisture content) that have the potential to increase the degree of explosibility for that specific fuel. However, the unique presentation of these properties in metal dusts contributes significantly to their complexity and well-developed severity.

2.1.1. Flame Propagation Behavior and Turbulence Effects

The fundamental structure of a particle's propagation mechanism is directly connected to the intensity of its systematic flame growth. For metallic particulates, there are two relevant regions surrounding the particle during combustion: the preheat zone and the combustion zone. The flame propagation pathway through a dispersed aluminum cloud (0.42 kg/m^3 concentration, pure aluminum with a particle size of <18 µm) was experimentally observed by Sun et al. using high-speed cameras with a microscopic optical system.[24] Based on the results of this study, the burning process of aluminum is depicted as follows. First, the unburnt solid metal particle begins to heat as the oncoming flame front grows near. Once oxidation temperatures are reached, an oxide layer begins to form on the particle surface. As the localized temperature rises further, the solid aluminum particle becomes a liquid/vapor mixture as its melting point is surpassed and the boiling point is approached. The developing vapor phase then positions itself between the liquefied aluminum and the oxide coating. As temperatures continue to increase, prompt liquid expansion within the oxide layer generates pressures and internal stress strong enough to crack the oxide shell. This allows for escape of the vapor phase through the oxidation layer, leading to gas-phase

reactions in the combustion zone and an extremely asymmetric burning pattern. This mechanism has significant dependence on combustion temperatures and further qualifies the spontaneity and unpredictability typically associated with reactive metal deflagration propagation. Other noteworthy mechanism proposals for the combustion of aluminum dust are depicted by Puri.[25]

In validation of the aforementioned mechanism by Sun et al., Gao et al. similarly depicted the flame propagation behaviors of 40-nm titanium, aluminum, and iron dust clouds.[26] Combustion reaction was noted to occur in the liquid phase, gas phase, and solid phase, respectively. Average propagation flame speeds were obtained as follows: 0.565 m/s for titanium, 0.189 m/s for aluminum, and 0.035 m/s for iron. During liquid- and gas-phase metal particle combustion, Gao et al. noticed the occurrence of "micro-explosions" due to spontaneous interactions with the oxidation products which had formed. Furthermore, through constant pressure combustion, Dreizin and Hoffmann observed the propagation mechanism for a magnesium dust cloud in a microgravity setting. This study demonstrated the reaction rates within the preheat and combustion zones as having an oscillatory, cyclic pattern; Dreizin and Hoffmann also observed the abnormality of secondary ignition of single-particles following the original propagation.[27]

Combustion duration and flame speed are other factors which illustrate the full profile of a fuel's propagation behavior. In a study by Broumand and Bidabadi, the one-dimensional combustion of micron-sized iron dust was modelled based on energy balances in both the preheat and combustion zones. As a result, correlations for combustion time and flame velocity were derived as a function of particle diameter (combustion time $\propto d^2$; laminar flame velocity $\propto d^{-1}$).[28] In addition, demonstrated within the above-mentioned study by Sun et al. is the effect of concentration and combustion time on flame speed during aluminum dust propagation.[24] Assuming that the saturation fuel concentration (above which combustion would have been

dampened) had not been reached, flame speed is expected to rise with higher fuel concentrations. Moreover, the flame speed seems to increase exponentially for greater time durations following initial ignition. For applications in which more fuel is available or in which the contained combustion volume is substantial, this could be problematic. In other words, it would take longer for the combustion to run its course, signifying the potential for extremely high flame speeds and amplified likelihood for deflagration to detonation transition (DDT). At the moment at which the flame front catches up with the preceding pressure front, a DDT can result. Deflagrations tend to propagate through direct heat transfer; on the other hand, detonations propagate by means of pre-compression. Detonations are differentiated from deflagrations due to their devastating properties including accelerated flame speed growth, increased rate of pressure rise, and maximum resultant pressures as high as 20 to 80 barg. Pipeline flame propagation data described by Going and Snoeys clearly depict the flame speed effects as a function of distance from ignition volume.[29] Commonly transitioning within interconnecting ductwork, deflagrations can easily accelerate to detonation velocities if left unprotected. Ideally, in the absence of effective prevention, an additional solution would be to block propagation pathways via mechanical isolation or timely injection of a chemical suppressant. Further details regarding isolation requirements are described in NFPA 69, the Standard on Explosion Prevention Systems.[30] However, large-scale validation testing (activation times, device placement, injection quantities, etc. must be confirmed to provide a stable protection design) is necessary prior to direct application of such guidance to metal dusts in particular.

Turbulence is known to have a prominent impact on deflagration combustion rate. From an application standpoint, internal baffles, partitions, pipeline fittings, and elbows all can act as means of adding turbulence to the system. Completed in a 20 L spherical test vessel, Zhang et al. illustrates the influence of turbulence and uniformity of dispersion on aluminum powder

explosions, as a function of nominal fuel concentration.[31] Agitating the sample within the test vessel prior to ignition, this study revealed direct correlation between turbulence and maximum rate of pressure rise at lower nominal dust concentrations. At higher nominal fuel concentrations, dust dispersion uniformity replaced turbulence as the driving force. Increasing turbulence at higher concentrations often left some localized regions too concentrated with fuel to support combustion, exceeding the upper flammability limit of the aluminum/air mixture. The influence of turbulence on combustion rate and flame propagation can be modeled analytically. Christill et al. established a model for the prediction of propagation and pressure growth mechanisms in gas explosions and has established the foundation for the development of a comparable model capable of determining effects of turbulence in dust explosions.[32]

2.1.2. Particle Size & Specific Surface Area

Under ideal dispersion conditions, particle size has a primary influence on the overall surface area available for combustive heat generation. As a general trend for most dusts, decreasing particle size demonstrates an inverse relationship with ignition sensitivity and explosion severity. For most organics, however, this relationship will not continue indefinitely. Depending on the fuel, there is a limiting particle size below which the dust will not exhibit augmented combustion rate. As described by Eckhoff, the reasoning behind this phenomenon can be illustrated through examination of the steps of a typical organic combustion process: pyrolysis (or devolatilization), gas-phase mixing, and gas-phase combustion.[6] The first step, devolatilization, is considerably influenced by particle size. Yet, if this step is not the rate limiting step, then further decrease in particle size would have no impact on the overall rate. As described in Section 2.1.1, metal dusts do not devolatilize, but rather exhibit a dissimilar combustion mechanism which encompasses melting, evaporation, and burning of distinct particulates. As a result, the limiting particle size is

much larger for organics than for metals. Therefore, further decrease in size of atomized metal powders (or equivalent increase in specific surface area) tends to yield exponential increase in severity parameters such as maximum rate of pressure rise. In Figure 2.1, Eckhoff reviews this effect for silicon/air and aluminum/air mixtures, while allowing for comparison to natural organic materials such as dry starch and protein.[6,33,34]

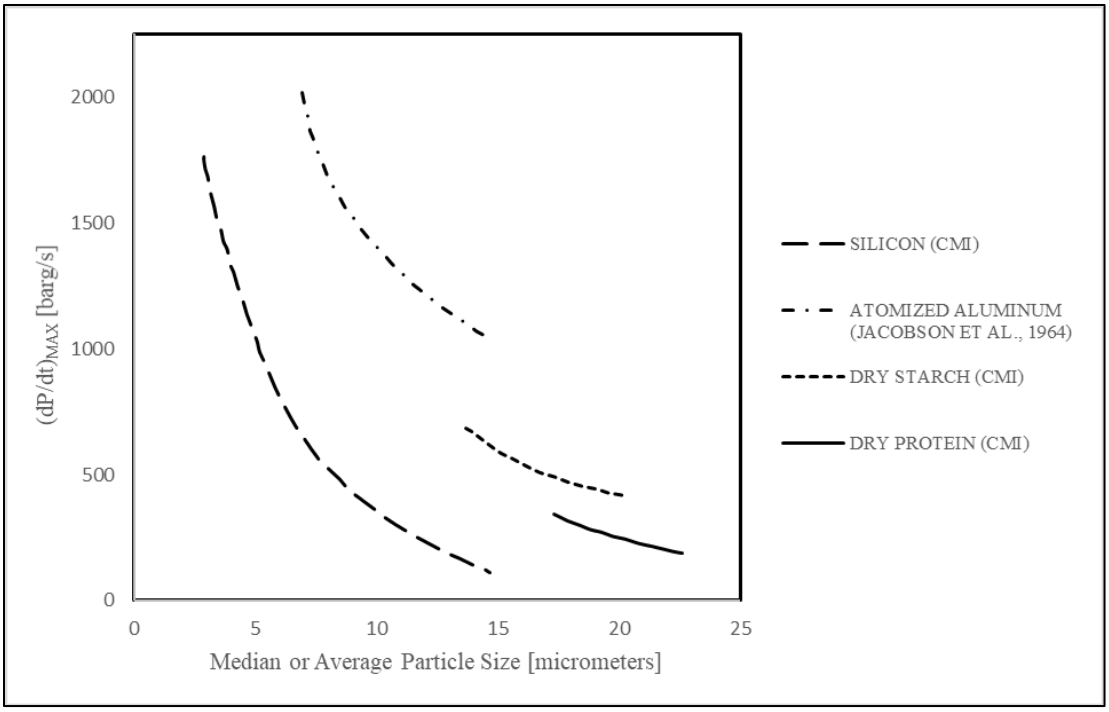

Figure 2.1. Maximum rate of pressure rise as a function of particle size for silicon, aluminum, and organic dust clouds in air; results from Hartmann bomb explosibility vessel (Eckhoff et al. and Jacobson et al.).[33,34]

Explosibility as a function of particle size was further explored in a research study led by Kadir et al.[35] Upon testing nano- and micro-sized aluminum particles in a 20 L spherical vessel, the study was able to confirm the increase of K_{St}, MEC, and MIE with decreasing particle size. More notably, this group proceeded to validate their explosibility testing through transient three-dimensional Computational Fluid Dynamic (CFD) model simulation, further supporting their claims of higher turbulent kinetic energy during deflagrations of samples with reduced particle size. Boilard et al. investigated similar concepts, except through analysis of micro- and nano-size titanium powders.[36]

In this study, nano-titanium particles exhibited extremely high ignition sensitivity, demonstrating pyrophoric tendencies as soon as the fuel was brought into contact with O_2 concentrations large enough to support combustion (auto-ignition without external ignition source). Krietsch et al. presents comparable results for a wide variety of metal types, including nano-sized titanium, aluminum, zinc, copper, and iron.[37]

Size alone is not enough to properly define the severity of the hazard. The shape and nature of the dust must also be considered. According to BIA Report 13/97, micrometer-sized aluminum powder has the capability of displaying K_{St} values as high as 1100 barg-m/s, maximum explosion overpressure as high as 12.9 barg, and minimum ignition energies as low as < 1 mJ. In addition, this report collects explosibility parameters for a multitude of other metals and metal alloys of varying particle size, shape, and processing consistencies.[38] Even aluminum flakes, with a much larger nominal particle size, were able to produce a K_{St} of 600 barg-m/s when utilized in explosion suppression testing investigated by Moore and Cooke.[39]

A variable often overlooked when characterizing the degree of the hazard, dispersity (defined as the heterogeneity of particle sizes in a mixture) can have nearly as dominating of an effect on explosibility as particle size. Centered on a mean size, dispersity represents the magnitude of the full particle size distribution and is pertinent to a majority of dust conveyance applications, in which the particle size of the process media is either unfixed or unknown. Studies carried out on this subject by Castellanos et al. report the influence of particle size dispersity on the explosibility parameters (K_{St} and P_{max}) of aluminum dust propagation. At constant mean particle diameter of 15 µ, samples of varying dispersity were prepared and tested in a 36 L explosion test vessel. The sample most concentrated around the mean particle size (lowest dispersity) yielded a K_{St} of 179 barg-m/s and a P_{max} of 9.15 barg. The sample with the largest dispersity represented an increased

explosion hazard, with resultant K_{St} and P_{max} values of 413 barg-m/s and 10.25 barg, respectively.[40] High dispersity in a sample provides increased likelihood for the presence of fine particulates, which have lower ignition temperatures, and escalates the combustion rate due to their considerable specific surface area.

2.1.3. Moisture Content

In consideration of organic dusts, increasing moisture content of an explosible dust powder reduces the ignition sensitivity and explosion severity. As described by Eckhoff, the ability of moisture to inhibit explosibility stems from three major concepts.[6] First, water acts as an inert heat sink, pulling energy away from the developing combustion. Second, upon evaporation the water vapor combines with the pyrolysis vapor, allowing for a less reactive mixture in the combustion zone. Third, high moisture content causes the powder to agglomerate together which impedes full particulate dispersion. However, the influence of relative humidity is more complex for metallic dust deflagrations. By examining the impact of aluminum humidity (Case 1) and atmosphere humidity (Case 2) on explosibility, investigations made by Traoré et al. provide some clarification on these intricacies.[41] As presented by Case 1, results indicate that storage conditions have a detrimental effect on explosion severity. In comparison to dry aluminum powder (median diameter of 7 microns) with a maximum rate of pressure rise of 1530 barg/s, experiments conducted for the same fuel concentration (250 g/cm^3) at 76% relative humidity yielded a maximum rate of pressure rise of more than 2150 barg/s. After treating the aluminum at high humidity for long periods, the water has time to adequately adsorb onto the surface and, upon ignition, reacts with the solid aluminum particle to produce gaseous hydrogen (H_2), as demonstrated in Reaction R3.

$$2Al_{(s)} + 3H_2O_{(g)} \rightarrow Al_2O_{3\,(s)} + 3H_{2\,(g)} \quad \text{(R3)}$$

Once the oxide shell is broken (as explained in Section 2.1.1), release and combustion of H_2 contributes another fuel source to what is already an extremely reactive metal deflagration. In Case 2, explosion testing of dry aluminum powder was performed with no humidity pretreatment. Instead, the test atmosphere was injected with specific water volumes immediately prior to ignition, with the objective of creating a saturated atmosphere but impeding adsorption of water onto the particle surface. Unlike Case 1, by limiting the water-metal contact time to the explosion duration exclusively (approximately 20 to 70 milliseconds), the explosion severity is significantly reduced. This study saw a decrease in the maximum rate of pressure rise, from 900 barg/s for the dry aluminum powder to 400 barg/s for the aluminum powder in a fully water-saturated atmosphere (0.3 mL in a 20 L sphere test vessel).

These claims can be further supplemented through work performed by Bernard et al. When examining the inhibition effect of partially oxidized aluminum dust, Bernard noticed an interesting phenomenon concerning moisture content. At constant oxide concentration, increases in water concentration from 1.4 to 1.7 wt % coincided with a corresponding rise in flame speed (from 0.25 to 0.30 m/s) and decrease in MIE. Although pre-ignition oxide concentrations generally induce mitigation of the combustion rate, oxides in the presence of saturated water are unable to dampen combustion. On the contrary, increased residual water content within the oxide shell seemed to reflect augmented flame speed and ignition sensitivity.[19]

The above discussion involves elementary properties whose variance reveals an exceptional consequence when dealing with metal dusts. Section 2.2 will explore hazards specific only to combustible metals.

2.2. Hazards Specific to Combustible Metals

Propagation behavior, turbulence, particle size, and moisture content are not the only characteristics capable of enhancing the magnitude of a metal-induced explosion. The following exclusive metal properties qualify metal dusts deflagrations as unique explosion hazards: high heats of combustion, high flame temperature, radiation heat transfer tendencies, and aggressive interactions between water and burning metallic particles.

2.2.1. Heats of Combustion & Flame Temperatures

Heat of combustion represents the energy liberated, per mole of O_2 consumed, during metal oxidation and combustion decomposition. Assuming the fuel concentration is maintained throughout combustion, the total amount of heat released is directly limited by the presence (or lack thereof) of O_2 within a contained volume. For this reason, standard practice is to scale heat of combustion based on the number of moles of O_2 available to sustain the combustion reaction. Table 2.1 depicts heats of combustion for several of the more common industrial metals. The more reactive metals, such as calcium, magnesium, and aluminum, have heats of combustion as high as 1270, 1240, and 1100 kJ/mole of O_2, respectively. The energy released during the oxidation of these metals is more than twice that of the heat released during combustion of organic fuels (starch at 470 kJ/mole of O_2; carbon at 400 kJ/mol of O_2).[6]

Table 2.1. Heats of combustion per mole of oxygen consumed for common metallic substances[6]

Material	Oxidation Product(s)	Heat of Oxidation (kJ/mole of O_2)
Calcium	CaO	1270
Magnesium	MgO	1240
Aluminum	Al_2O_3	1100
Silicone	Si_2O_3	830
Chromium	Cr_2O_3	750
Zinc	ZnO	700
Iron	Fe_2O_3	530
Copper	CuO	300

The amount of heat liberated during combustion is in direct correlation with the derived adiabatic flame temperature for a given fuel. A constant volume adiabatic flame temperature represents idealistic conditions in which the combustion is complete and in which no internal energy changes occur within the system (in other words, no transfer of heat, work, kinetic energy, or potential energy through the system boundary). As tabulated by NFPA 484, "The Standard on Combustible Metals", maximum adiabatic flame temperatures for a variety of metals are shown in Table 2.2, with calculations performed by Cashdollar and Zlochower.[12,42] As a result, aluminum and hafnium exhibit the highest maximum adiabatic flame temperatures of 3790 °C and 4580 °C, respectively.

Table 2.2. Maximum adiabatic flame temperatures (MAFT) for various metals[12]

Metal	Copper	Zinc	Iron	Tungsten	Chromium	Silicon	Boron
MAFT (°C)	1250	1800	2220	2830	2900	2970	3030
Metal	Niobium	Magnesium	Tantalum	Titanium	Aluminum	Hafnium	
MAFT (°C)	3270	3340	3490	3720	3790	4580	

Higher flame temperatures have the tendency to result in larger heat fluxes and signify the thermodynamic potential of a combustion, as previously mentioned. According to ideal gas law relationships, temperature is in direct proportionality with system pressure. With that said, one could expect a significant rise in maximum explosion pressure (P_{max}) for fuels that display increased burning temperatures. Cashdollar and Zlochower also compare adiabatically calculated flame temperatures to experimentally determined values. As a general trend, this study noticed that experimental temperatures begin to approach adiabatic temperatures as particle size decreases, revealing that finer metallic samples are more characteristic of intrinsic combustion properties.[42] Increased metal particle volatility and spontaneity of the flame propagation mechanism are a major byproduct of higher flame temperatures.

2.2.2. Radiation Heat Transfer & Harmful Combustion Products

Particle emissivity contributes significantly to the radiative heat flux that exists throughout the combustion zone. As described in experiments by Elsner et al., the particulate emissivity of solid organic fuels (ash and quartz sand) is complex and dependent on a variety of factors including dust cloud thickness, primary particle specific surface area, solid loading (or dust concentration), adsorption factors, and scatter coefficients.[43]

As demonstrated in Equation E4, the Stefan-Boltzmann law describes the flux of energy (j) radiated across all wavelengths per unit surface area of a black body per unit time:

$$j = \sigma T^4 \tag{E4}$$

where σ represents the Stefan-Boltzmann constant. This relationship directly relates radiant emittance to the fourth power of temperature. Therefore, the influence of radiative heat transfer observed during combustion propagation increases considerably for metals with higher burning temperatures. In a series of qualitative studies by Leuschke, the significance of radiation heat transfer within metal dust clouds was confirmed.[44] In his experimental setup, two transient dust clouds were dispersed at the same time on opposite sides of an insulated double-pane glass window. Upon immediate ignition of one dust cloud, it was observed whether or not the radiation from the ignited dust cloud was sufficient to initiate combustion in the other non-ignited dust cloud. As a result, open-air deflagrations of zirconium, titanium, aluminum, and magnesium generated adequate radiative energy, transmitted through the glass pane, to induce ignition in the other adjacent dust cloud. Primarily dominated by conductive and convective heat transfer mechanisms, low burning temperature metals such as iron and organics such as coal were unable to produce a similar effect. This effectively demonstrates the principal role of radiation heat transfer in combustion growth for high burning temperature metals. As a means of quantifying this concept,

Christophe et al. designed experiments to effectively measure the radiated flux during flame propagation through aluminum/air mixtures (particle size = 100 μ, fuel concentration = 270 g/m^3, and radiated flux = 40 kW/m^2).[45]

Other groups have investigated this topic from a theoretical, numerical solution perspective. Utilizing a discrete element method (DEM), investigations by Moussa et al. successfully simulate the radiative heat transfer between dust cloud particulates as well as the heat transfer which occurs in the bulk preheat zone. Although some assumptions are made in this methodology (ignition temperature is kept constant; particle motion is ignored; heat generation due to chemical reaction is neglected), DEM presents the basis of what could be a viable alternative for flame propagation modeling of metal dust deflagrations.[46]

The influence of radiation in heat transfer during propagation has been found to be dependent on the scale of the experiment, according to studies performed by Julien et al. For small-scale studies on ignited aluminum dust clouds, as dust loading increases, there is an absence of equivalent rise in flame speed. This demonstrates negligible effects of radiation heat transfer for small-scale aluminum dust cloud propagation, in which radiation release acts merely as a heat loss mechanism. For large-scale open-air deflagration experiments, the size of the dust cloud is much larger than the effective radiation absorption span, signifying that radiation emitted by the combustion will be sufficiently absorbed by the unburnt metal particles. Along with the effects of localized eddy turbulence, radiative preheating mechanisms contributed to a six-fold increase in flame speed.[47]

Another factor to consider is the toxicity level of the byproducts released during metal fuel decomposition. Unlike organics, which primarily emit carbon dioxide and water during combustion, metal oxidation can produce a wide variety of toxic reaction products. As an example,

several types of magnesium alloys produced in industry contain trace amounts of thorium, a low-level radioactive element. The decay process of thorium is generally isolated within the alloy until the metal is melted or burned. Volatiles of the radioactive thorium are present in the gaseous products released during burning of the alloy particles. Although the half-life of thorium is significantly greater than other more unstable radioactive elements, this factor nevertheless contributes to the severity of lung tissue damage upon inhalation during burning of magnesium alloys.[12]

2.2.3. Reactivity with Water

In Section 2.1.3, the discussion was centered around the effect of moisture content on metal dust explosibility. Here, that dialogue is expanded to include discussion of the high reactivity that results when water is introduced to molten metal or pre-existing metal fires. Typically, water on an organic fire will act as a heat sink, depriving heat (and oxygen, if enough water is present) from the ongoing combustion. However, burning metals present a different case in which they react with water at high temperatures to produce explosive volatiles, including diatomic hydrogen. This can lead to violent explosions in a variety of industries, with particular concern in nuclear and metallurgical processes where wet dust collection and water deluge systems are utilized. This was the situation that led to the explosion incident at AL Solutions, as described by the CSB investigation report.[3] In this circumstance, the milling process removed much of the protective oxide coating surrounding zirconium particulates, leading to the exposure of a metal-water interface and promoting increased H_2 formation. Previous risk assessments acknowledged the hazards of water reactivity with burning metals, but no action was taken to improve housekeeping or challenge the existence of a water-based fire suppression system in the production area.[3]

Studies performed by Wang et al. demonstrate a viable pretreatment technique to be exploited specifically for wet dust removal applications. Through preparation of the aluminum dust via introduction of dilute chromium potassium sulfate solution, the hydrogen inhibition method (HIM) describes the use of alumina and chromium oxide (Cr_2O_3) inhibition films to successfully prevent the interaction between water and the metallic core.[48] This process treatment procedure offers a relatively inexpensive prevention technique for the inhibition of H_2 formation during wet metal dust removal processes.

Unfortunately, H_2 production is only part of the reason for the violence of this reaction. Although the intensity of the interaction between water and molten metal is not fully understood, *Lees' Loss Prevention in the Process Industries: Hazard Identification, Assessment and Control* describes superheat theories which serve as a potential explanation.[49] Another explanation for the violent nature of such reactions comes from experiments performed by Mason et al.[50] Using high-speed cameras and molecular dynamics simulation, Mason and his team justify the spontaneity of the heterogeneous reaction between alkali metals (Na/K) and water. Otherwise known as a 'Coulombic Explosion', Mason suggests that instantaneous electron transfer to water molecules leaves an extremely positive alkali ion surface. This instability in charge results in extensive fragmentation of the alkali particle within milliseconds, with increased surface area contributing further to the violent nature of the reaction.

Chapter 3: Inhibitor Analysis via Simultaneous Thermal Analytical Techniques

3.1. Inerting & Mitigation Studies on Key Suppressant Agent Materials

Sodium bicarbonate (SBC; $NaHCO_3$), potassium bicarbonate (PK; $KHCO_3$), monoammonium phosphate (MAP; $NH_4H_2PO_4$), diammonium phosphate (DAP; $(NH_4)_2HPO_4$), and sodium chloride (Met-L-X; NaCl) have been selected as the suppressant agents to be tested analytically. SBC (CASRN 144-55-8) was acquired from Ansul in the form of the suppressant agent "Plus-Fifty C Dry Chemical" (product code 009336), which is primarily composed of SBC with trace amounts of calcium carbonate, attapulgite, and other inert flow-promoting additives. PK (CASRN 298-14-6) is acquired from Ansul in the form of suppressant agent "Purple-K Dry Chemical" (product code 009335), which is primarily composed of PK with trace amounts of flow-promoting additives. MAP (CASRN 7722-76-1) was acquired from Amerex in the form of "ABC Dry Chemical Fire Extinguishant" (product code CH555) and contains 90-98% MAP, with trace amounts of inert chemical additives and flow-promoting materials. DAP (CASRN 7783-28-0) was purchased from Parchem at high purity. Met-L-X was also acquired from Ansul (product code 009328) and is composed of 80-90% sodium chloride (CASRN 557-04-0), with trace amounts of a heat-absorbent polymer additive, used for desiccation and fluidization of the agent. Decreased particle size yields increased surface area and corresponds to greater inhibition performance of the agent; thus, to eliminate particle size as a potential parameter affecting inhibitor performance, all suppressant agents were ground and sieved to a similar mean size (20 ± 5 μm). Such material pretreatment allowed for adequate consistency in the degree of particle dispersity. Particle size distributions for all suppressant agents were assessed using a laser diffraction particle size analyzer (CILAS 990) and are documented within the Appendix (Figures A.5, A.6, A.7, A.8, and A.9). All

relevant statistical data related to suppressant agent particle size are also documented within the Appendix (Table A.1).

3.1.1. Carbonates (Sodium Bicarbonate and Potassium Bicarbonate)

With the use of 20 L sphere testing, Jiang et al. investigated the effects of sodium bicarbonate particle size on the mitigation and preventative inerting of 5 and 30 μm aluminum dust explosions.[51] This study found a gradual decrease in maximum explosion pressure through increased SBC concentrations and at smaller suppressant particle sizes. For a 5 μm aluminum dust concentration of 300 g/m^3, the MIC of SBC was found to be 1900 g/m^3 and 2100 g/m^3 for suppressant particle diameters of 53 to 75 μm and 110 to 212 μm, respectively. For a 30 μm aluminum dust concentration of 800 g/m^3, the MIC of SBC was found to be 1200 g/m^3 and 1000 g/m^3 for suppressant particle diameters of 53 to 75 μm and 110 to 212 μm, respectively. The inhibition mechanism for sodium bicarbonate occurs in four determinant steps. Firstly, suppressant particles undergo heating due to initiated fuel combustion. Secondly, the agent begins to decompose. Thirdly, gas and solid phase decomposition products are produced. Fourthly, combustion propagation inhibition occurs. The total duration of these four events is designated by t_i. In the case of 5 μm aluminum combustion, since the burning time (t_b) is exceedingly brief in comparison to the aforementioned SBC inhibition process (t_i), particle size reduction had a minimal effect on lowering of the MIC (9.5% decrease in MIC for 5 μm aluminum; 16.7% decrease in MIC for 30 μm aluminum). For situations such as this, in which $t_b << t_i$, the inhibition of flame becomes increasingly dependent on thermal mechanisms to account for the relatively slow rate of chemical inhibition modes. Although the chemical decomposition duration may not be optimum for smaller fuel particle sizes, SBC nevertheless appears to play a pivotal function in impeding gas phase aluminum combustion propagation. For the mitigation of aluminum combustion, the role of

SBC in reducing the fuel burning rate is found to rely primarily on thermal heat absorption and oxygen dilution mechanisms. This speculated deficiency in chemical inhibition is expected considering the low-temperature decomposition of sodium bicarbonate (Appendix B; Figure B.1) relative to the high oxidation temperature range and high maximum adiabatic flame temperature (reported at 3790 °C) of aluminum.[12]

In another study, Chen et al. investigated the effect of sodium bicarbonate with varying granulometric distributions (particle dispersity) on 15 μm aluminum dust cloud propagation intensity. Inerting through the addition of suppression agent with wider particle size dispersity yielded limited flame temperatures, destabilized the overall combustion reaction, and inhibited development of the combustion reaction front. Fluctuating suppressant agent agglomeration patterns generated an increasingly non-uniform preheat zone thickness and decreased flame speeds when compared to agents characterized by a specific particle diameter.[52]

Through both burner and 20 L sphere analysis methods, Rockwell and Taveau investigated the influence of SBC on hybrid flame propagation. In this case, the hybrid mixture under evaluation consisted of 27 μm mean particle size iron powder and gaseous methane-air with an equivalence ratio of one. At fuel concentrations between 25 and 75 g/m^3, this study found a noticeable decrease in turbulent burning velocity and maximum rate of pressure rise (K_{St}) upon addition of 27 μm SBC at concentrations between 25% and 75% of the initial iron concentration.[53] During SBC decomposition, the agent effectively interferes with the expansion of the hybrid flame zone by releasing water vapor and carbon dioxide decomposition products, which participate thermally as heat sinks.

Going and Snoeys examine and contrast the efficacy of inert powders SBC and PK for the mitigation of silicon and aluminum metal dust deflagrations using 1 m³ explosion suppression

testing.[29] Following explosibility testing at optimum fuel concentration, silicon dust demonstrated a K_{St} of 120 barg-m/s and a maximum pressure developed during a contained deflagration (P_{max}) of 8.16 barg. At 1000 g/m³ suspended silicon concentration, deflagration suppression testing(at 0.05 barg activation pressure demonstrated similar TSPs of 0.33 and 0.27 barg for SBC and PK, respectively, at 2.3 kg/m³ agent concentration. Even at increased PK concentration of 4.5 kg/m³, results indicate no further enhancement of the suppression performance. On the contrary, the resultant TSP under these conditions increased slightly due to greater injection pressures, implying that the protected volume was fully suppressed at 2.3 kg/m³ agent concentration. Although minimal differences between SBC and PK suppression performance were apparent for silicon dust deflagration mitigation, the testing for aluminum dust (K_{St} = 300 barg-m/s, P_{max} = 8.50 barg) proved aluminum deflagrations more difficult to suppress but displayed noticeable trends in agent performance. For aluminum dust at 1750 g/m³ fuel concentration (0.05 barg activation pressure), SBC and PK at 4.5 kg/m³ agent density yielded TSP values of 2.05 barg and 1.25 barg, respectively. Although PK appears to be more effective at 4.5 kg/m³, both SBC and PK required a much higher agent concentration in order to induce complete suppression (at 9.1 kg/m³, TSPs for SBC and PK were reported at 0.84 barg and 0.89 barg, respectively). For metal dust deflagrations, the TSP is shown to correlate strongly with the suspended fuel concentration. Increased heat liberation and pressure generation over the combustion duration require improved physical inhibition (i.e., greater concentrations of suppressant agent) in order to maintain moderate TSPs. On a large-scale application setting, the effectiveness of the agent toward complete suppression of metal dust deflagrations depends on additional factors other than the agent composition. Bulk material flow limitations such as inverse velocity at specific throw distances, discharge velocity, and injection profile will also exhibit an appreciable influence on system performance and the

ability of the agent to suppress deflagrations at higher fuel concentrations.[54,55] Aside from this work, PK has not been investigated as extensively as SBC from an explosion inhibition standpoint; however, it does demonstrate adequate inerting performance when employed as a fire suppressant.[56]

3.1.2. Phosphates (Monoammonium Phosphate and Diammonium Phosphate)

Flame retardants containing nitrogen compounds are excellent options for preventative inerting of bulk combustible solids. Nitrogen and nitrogen-phosphorous based solid inertants and their decomposition products exhibit substantially lower toxicity, decreased corrosion, and increased efficiency in comparison to common metallic hydroxide alternatives. The relatively low activity of metal hydroxide flame retardants necessitates higher minimum concentrations to meet equivalent inhibition performance. Utilized in many polymer and plastic manufacturing industries, nitrogen-based compounds possess high decomposition temperatures, allowing the inert material to be recycled within the process without concern of potential degradation of the physical properties of the polymeric material. Use of halogen flame retardant puts the plastic production process in jeopardy by limiting the potency of polymer stabilizer additives.[57]

Studies by Jiang et al. compared the inhibition of 5 and 30 μm aluminum dust explosions with MAP and SBC. As the concentration of inert material increased, the flame front became increasingly irregular, resulting in restricted flame propagation velocity. At a constant 1000 g/m^3 fuel concentration, MAP exhibited a greater impact on average flame propagation velocity reduction relative to SBC. Flame propagation through a 30 μm aluminum dust cloud was fully inhibited by addition of MAP at an agent concentration of 1300 g/m^3, while SBC did not completely impede the deflagration until the agent concentration exceeded 2200 g/m^3. Similar performance trends were measured for propagation inhibition through a 5 μm aluminum dust

cloud. MAP was able to fully suppress the propagation at an agent concentration of 1600 g/m^3, whereas the minimum inerting concentration for SBC was not obtained, even at agent concentrations as high as 2200 g/m^3. Both agents utilize physical endothermic decomposition within the flame front, absorbing combustion heat used to volatilize nearby particles in the preheat zone. The presence alone of the inert particles within the dispersed fuel/air cloud adds resistance to the direct diffusion of oxygen, blocking further gas-phase single element oxidative combustion. Using kinetic modeling techniques for stoichiometric mixtures of aluminum/air and inhibitor, Jiang et al. demonstrate that the MAP inhibition mechanism more effectively competes for oxygen and oxygen radicals, which chemically interrupts the combustive aluminum oxidation and limits temperature rise within the mixture.[58] Luo et al. examined the effects of ammonia on methane gas combustion dynamics and arrived at similar conclusions regarding the suppressive mechanism of ammonia compounds. For specific volumes of air mixed with of 7, 9.5, and 11 vol % methane, increased ammonia content correlated directly with narrowed fuel explosibility limits, reduced maximum explosion pressures, and decreased rates of pressure rise. Ammonia and amino groups readily consume radicals required to sustain methane combustion due to significantly lower activation energies when compared to methane and methyl group chain reactions.[59]

In other inhibitor inerting investigations, Chatrathi and Going measured the MIC of SBC and MAP with a variety of fuels. At constant ignition energy and system turbulence, SBC and MAP demonstrated similar minimum agent concentrations required to prevent the development of the flame front (625 g/m^3 and 875 g/m^3 for SBC and MAP, respectively) at the ideal concentration of suspended cornstarch. However, even at inerting concentrations as high as 2750 g/m^3, SBC and MAP were both unable to prevent sustained deflagration growth upon ignition of aluminum powder at optimal fuel concentration.[21] Despite some accounts of reported ineffectiveness for the

mitigation of aluminum dust explosions, MAP demonstrates promise as a candidate for the suppression of iron powder deflagrations, as discussed in the subsequent Section 3.4 through thermogravimetric analysis (TGA) and differential scanning calorimetry (DSC) of iron powder and iron/inhibitor mixtures. Analogous analytical studies on zinc powder combustion directly support claims of amplified chemical inhibition due to alignment of the agent decomposition range with the fuel oxidation temperature range.

Studies by Moore compare the efficacy of multiple dry chemical powder suppressants, including MAP, SBC, and Dessikarb® (food-grade sodium bicarbonate), for the mitigation of maize dust (K_{St} = 200 barg-m/s) deflagrations via active explosion suppression. At various system activation pressures between 0.05 and 0.3 barg, MAP continued to demonstrate amplified suppression efficiency, as well as equal or lower reduced pressures following complete agent injection into the protected volume.[60] However, tests performed by Amrogowicz and Kordylewski expose conflicting conclusions regarding suppression of organic fuels. The effectiveness of MAP and SBC were compared for both inerting and suppression of a variety of deflagration fuels (melamine, wheat flour, wood dust, and coal dust). MAP was found to be more effective for preventative inerting of organic deflagrations, while SBC was more effective for explosion mitigation application.[61]

Unlike MAP, DAP has not been thoroughly studied for either preventative explosion inerting or explosion mitigation. DAP is a suitable fire retardant additive material and shows potential as an effective explosion inhibitor based on its substantial energy absorption capabilities upon endothermic decomposition to ammonia and water.[62] Castellanos et al. evaluated the efficiency of MAP and DAP for the inhibition of cornstarch combustion propagation using TGA and DSC analytical techniques. Performed under a nitrogen atmosphere and at a 1:1 wt % fuel to agent

mixture ratio, analysis of DSC profiles demonstrated that the addition of MAP and DAP limited the heat released during fuel decomposition by 65.5 and 71.5%, respectively. In addition, upon constant heating of the cornstarch and MAP mixture, it was apparent that MAP induced a shift in the onset of exothermic decomposition to lower temperatures, suggesting that this agent may be better suited for explosion mitigation and less appropriate for preventative inerting. Explosibility testing in the 36 L combustion vessel found that DAP yields reduced fuel K_{St} at all inert loading weights/particles sizes and depicts DAP as having greater cornstarch combustion inhibition performance. The amplified heat absorption capacity of DAP can be explained in part by the increased ammonia content released during inertant decomposition in comparison to MAP. The higher vapor pressure of gaseous inert decomposition products generates an oxygen dilution mechanism which reduces the rate of sustained fuel combustion by limiting oxygen diffusion into the flame zone.[63]

3.1.3. Sodium Chloride-Based Suppressant Agent (Met-L-X)

As reported by Zalosh, Met-L-X is a certified Class D fire suppression agent, capable of extinguishing a variety of metal hydride fires.[64] According to NFPA 484, Met-L-X is the preferred extinguishing agent for the suppression of combustible metal fires involving the following pure metals: alkali metals, aluminum, magnesium, niobium, tantalum, titanium, and zirconium.[12] Unlike fire suppression agents consisting of water, carbon dioxide, or halogenated material, Met-L-X does not exhibit reactivity concerns when inhibiting metal hydride fires. Met-L-X is comprised primarily of sodium chloride and a thermoplastic polymer. The polymer additive increases sodium chloride cohesion and allows for more complete agent coverage of the burning metal to prevent further diffusion of oxygen. Many Class D agents such as Met-L-X demonstrate efficiency in extinguishing the initial metal fire; however, they differ in their inability to produce prolonged

cooling effects following the preliminary incident, which allows for the possibility of secondary ignition upon reintroduction to the oxidizing atmosphere.[64] Although it shows prevalence as an effective fire suppression material, sodium chloride has rarely been investigated for use as an explosion suppressant. However, agent decomposition shifted to higher temperatures makes Met-L-X a respectable candidate for aluminum deflagration mitigation due to increased probability for chemical inhibition, as described in Section 3.4.

Cao et al. explored the influence of NaCl on methane/air explosion suppression using ultrafine water mist in closed vessel combustion experiments. Following addition of 5% NaCl by mass, the water mist suppression technique was noticeably improved due to decreased combustion temperatures within the flame and preheat regions. Additionally, Cao et al. demonstrated that this consequence ultimately resulted in inhibited reaction kinetics and underdeveloped flame propagation velocities. The presence of sodium and chloride ions within the protected volume actively capture free radicals (·O, ·H, and ·OH) which would normally participate in the chain reactions of persistent methane explosion propagation.[65]

3.2. Instrument and Experimental Procedure

When appropriately predicting the efficacy of suppressant materials with increased affinity toward mitigation of large-scale flame propagation, two analytical techniques are noteworthy. The first, thermogravimetric analysis (TGA), measures the sample weight change as a function of increasing system temperature. The second, differential scanning calorimetry (DSC), measures the heat flow into or out of the system as a function of increasing temperature. The area beneath a DSC curve indicates the amount of heat released (or absorbed) during exothermic (or endothermic) sample decomposition, which provides an opportunity to quantify the relative capability of

compositionally unique inert materials to absorb heat released as a result of metal powder oxidation and to dampen continued fuel combustion.

The use of a TA Instruments SDT Q600 provided simultaneous TGA and DSC measurements from ambient temperature to a maximum operating temperature of 1500 °C. Such measurements were used to predict inhibition viability of the suppressant materials considered in this study, as well as to analyze the combustion characteristics of the candidate fuels. All experiments were performed with ceramic sample pans, under atmospheric pressures, and at a constant heating rate of 10 °C/min. Dust layer thickness for all thermal analytical experiments was maintained below 2 millimeters to maximize sample exposure to oxygen and to minimize the influence of thermal gradient through the powder. All equipment signals, including TGA weight, DTA baseline, heat flow, temperature, and cell constant, were recalibrated regularly to ensure accuracy of the measurements. Zinc was the metal standard used for all temperature calibrations, and calorimetric precision was confirmed to be within ±2%. Average sample loading weights are provided in Table 3.1, with a fuel to inhibitor mixture ratio held constant at 1:1 by weight. Each mixture trial was thoroughly blended during sample preparation prior to loading; however, the authors acknowledge non-uniform solids mixing as a potential degree of uncertainty. To account for this, all trials were repeated a minimum of three times to ensure the reproducibility of results.

Heat flow signatures from DSC analysis provide a predictive technique for characterizing the performance of an agent based on its “capacity” to absorb heat. This method was used to rank the effectiveness of the suppressant agents with respect to their ability to absorb heat away from both organic and metallic dust combustion. Before these results are discussed in Section 3.4, subsequent Section 3.3 offers background on the fuel candidates selected for this study.

Table 3.1. Average TGA/DSC sample loading weights.

Sample Type	Loading Weight [mg]
Inhibitor	10
Fuel	10
Mixture*	20

*Note: Regardless of total sample weight, mixture solids composition was maintained at a 1:1 ratio by weight. Slight variation in total loading weight is acceptable, as all TGA/DSC results are appropriately scaled by mass.

3.3. Fuels under Analysis

Food grade cornstarch $(C_6H_{10}O_5)_n$ was purchased from Ingredion (CASRN 9005-25-8). Cornstarch was selected as the organic fuel for the purpose of establishing a baseline for comparison. Large-scale suppression and preventative inerting results with cornstarch as the fuel are widely publicized in the explosion protection industry. Based on categorized data of existing explosion protection solutions designed by Fike Corporation between 2015 and 2018, greater than 90% of all metal dust active suppression and/or isolation systems involve either iron (steel) or aluminum powder fuels. To satisfy this application demand, pure iron and aluminum powder were thus chosen as clear candidate fuels for the study. Zinc powder was additionally selected as a fuel candidate because its melting and boiling temperatures (420 and 907 °C, respectively) fit well within the maximum temperature limitations of the instrument. However, due to lesser application demand, zinc powder was utilized for lab-scale analysis exclusively; resources were not available for further large-scale suppression testing with zinc powder. In comparison to normally reactive metal fuels (zinc and iron), processes conveying aluminum powder are considered to be highly reactive explosion risks. Analysis of alloy-type metals was avoided in order to prevent misidentification of the fuel combustion temperature range. Additionally, partially oxidized metals were not considered due to the inert tendencies of a metal oxide (limited contribution toward fuel combustion). Zinc powder (Zn-101; CASRN 7440-66-6), iron powder (Fe-101; CASRN 7439-89-

6), and aluminum powder (Al-100; CASRN 7429-90-5) were all purchased from Atlantic Equipment Engineers, a division of Micron Metals, Inc. Prior to explosibility or suppression testing, mean particle sizes for each metal fuel were determined using laser diffraction particle size analysis (CILAS 990). Particle size distributions and statistical particle size results for all fuel powders are provided in the Supplemental Information (Figures A.1, A.2, A.3, A.4, and Table A.1).

For fuels, the area beneath the exothermic curve measures the quantity of heat released (J/g) during oxidative combustion. This quantity can be obtained through integration of the fuel DSC signature over the temperature range specific to the fuel combustion zone. For the organic fuel, cornstarch, this combustion region occurs from approximately 250 to 575 °C and is illustrated by TGA and DSC shown in Figures 3.1 and 3.2, respectively. The TGA profile for cornstarch combustion depicts products commonly volatilized during organic fuel decomposition.

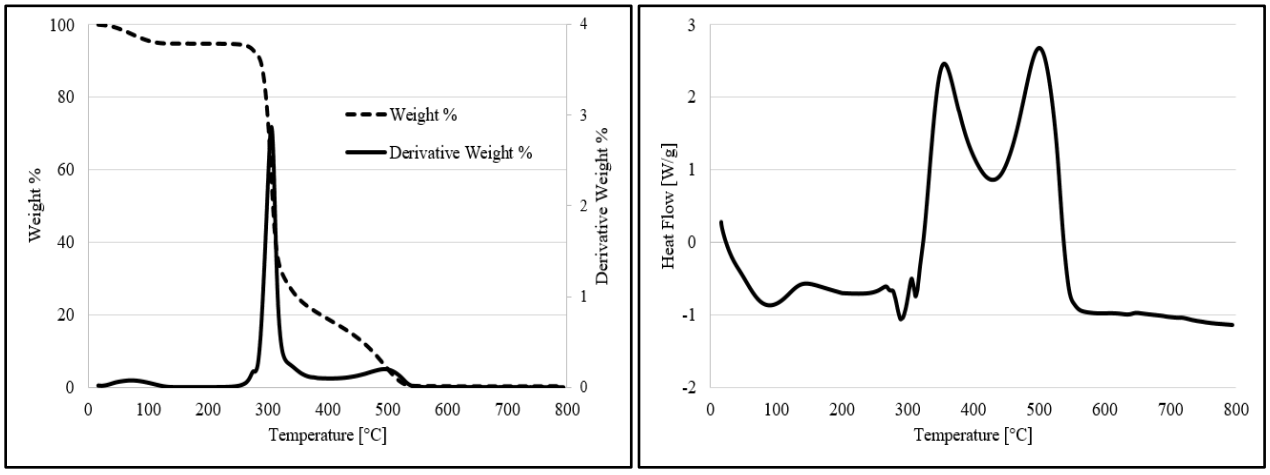

Figure 3.1 (left) & Figure 3.2 (right). Thermogravimetric profile (left) and differential scanning calorimetry profile (right) for cornstarch fuel. Increase in temperature, from room temperature to 800 °C, at a constant 10 °C/min heating rate (in air).

The first weight loss peak, at approximately 100 °C, represents the evaporation of water from the sample (1.34 wt % moisture content). Reliant on the dynamic oxygen availability at the reaction surface, the release of complete and incomplete combustion volatiles (CO_2 and CO, respectively)

occurs next with maximum derivative weight percentages at approximately 305 °C and 490 °C, accounting for approximately 95% of the total initial sample weight. Integration of the DSC profile over the fixed combustion region for cornstarch yielded 659±41 J/g of heat emitted during $(C_6H_{10}O_5)_n$ oxidation.

The zinc combustion mechanism is distinct in comparison to other pure metals, in that flame propagation occurs exclusively in the liquid phase.[66] Therefore, the combustion region of interest for zinc powder can be narrowed to the temperatures immediately succeeding the onset of melting, from approximately 420 to 750 °C, as shown by TGA and DSC analysis in Figures 3.3 and 3.4, respectively.

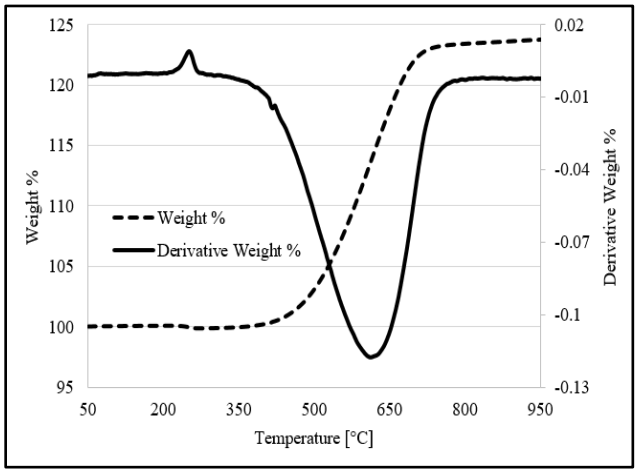

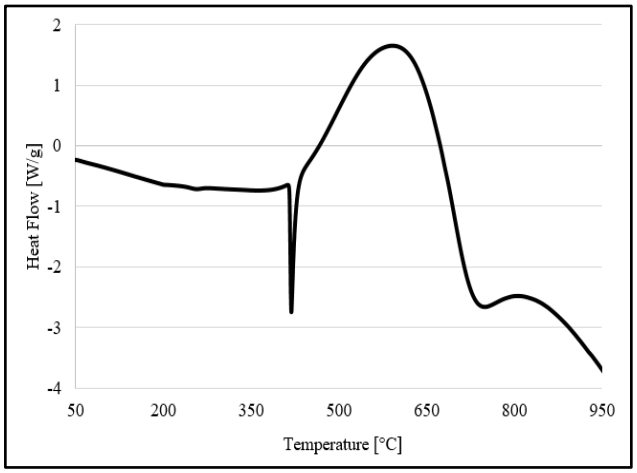

Figure 3.3 (left) & Figure 3.4 (right). Thermogravimetric profile (left) and differential scanning calorimetry profile (right) for zinc powder fuel. Increase in temperature, from 50 to 950 °C, at a constant 10 °C/min heating rate (in air).

Based on the DSC profile, the majority of the heat emitted during oxidation occurs immediately after the endotherm of melting (heat input required for the phase transition), which confirms that zinc combustion takes place in the liquid phase. Following exothermic heat release due to zinc oxidation, the heat flow signature becomes increasingly negative at higher temperatures due to inert material characteristics of metal oxides. The TGA profile for zinc powder combustion indicates sample weight increase during formation of metal oxide, which is characteristic of metal oxidation and aligns directly with the DSC exotherm temperature range. Slight weight decrease,

prior to the onset of zinc combustion, occurs at approximately 250 °C and can be attributed to decomposition of trace impurities within the sample. Integration of the DSC profile over the full zinc combustion temperature range yielded 3617±217 J/g of heat emitted during metal oxidation, which is more than five times the energy produced per gram of cornstarch.

The reader might expect the measured explosibility data shown in Table 3.2 to correlate directly with the reactivity and severity of combustion. In other words, augmented explosibility parameters would typically lead one to anticipate an increase in the amount of heat released during fuel combustion. This, however, was not the case. In reality, organic cornstarch exhibited a two-fold increase in the K_{St} during 1 m^3 sphere explosibility testing but released five times less energy per gram than zinc powder during combustion. Metal dusts have higher burning temperatures, heats of combustion, and radiation heat transfer rates compared with organic fuels; therefore, the assessment of severity and spontaneity of metal dust propagation using exclusively the explosibility index (K_{St}) is an unreliable means of evaluating overall fuel reactivity potential. The explosibility measurements for iron and aluminum powder fuels are documented in Chapter 4.

Table 3.2. Cornstarch and zinc powder fuel explosibility results at optimum suspended concentration and standard ignition delay, reported via analysis in 1 m^3 sphere combustion vessel.

Fuel	K_{St} [barg-m/s]	Pmax [barg]
Cornstarch	196	8.48
Zinc	97	5.97

As demonstrated by the iron powder TGA profile in Figure 3.5, sample mass increase due to iron oxidation occurs from approximately 200 to 800 °C (prior to iron's melting point at 1538 °C), verifying that iron is indeed a solid-phase combusting metal.[67]

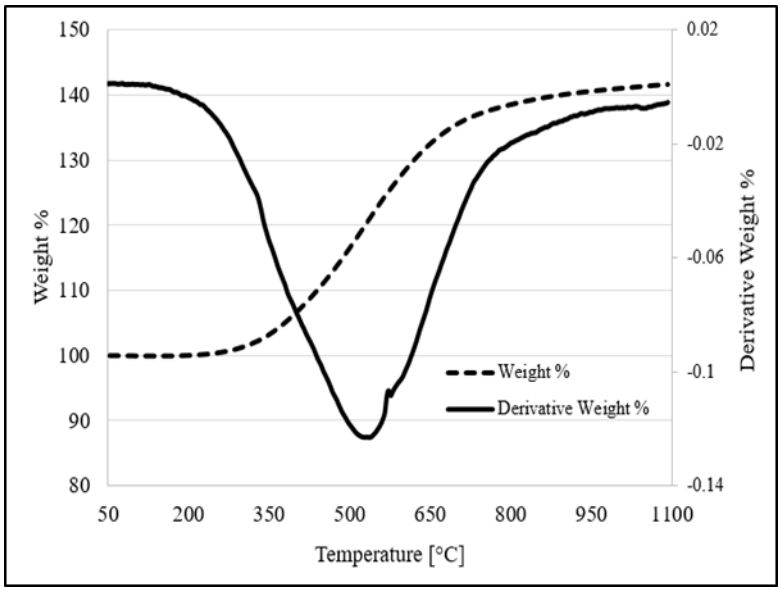

Figure 3.5. Thermogravimetric profile for iron powder fuel. Increase in temperature, from 50 to 1100 °C, at a constant 10 °C/min heating rate (in air).

3.4. Predicted Inhibitor Performances via TGA/DSC

3.4.1. Cornstarch as Fuel

In order to predict the combustion inhibition performance of various suppressant agent inhibitors, 1:1 wt % mixtures of cornstarch and inhibitors were analyzed using TGA and DSC. The heat flow signatures for each DSC profile (Appendix C; Figures C.6, C.7, and C.8) were integrated to calculate the amount of heat released during mixture decomposition. The difference between the heat released by the fuel and the heat released by the mixture directly indicates the heat effectively absorbed by the suppressant agent. The lower the total heat flow throughout the combustion temperature zone, the more efficient the inhibition during combustion. Prior to integration, all heat flow data were appropriately normalized by treating the cornstarch heat flow

signature, before and after the fuel combustion range, as the baseline. The integration results for all cornstarch and inhibitor mixture decompositions are provided in Table C.1. Compared to the heat released during exothermic fuel decomposition (659 J/g), potassium bicarbonate (PK) mixed with cornstarch exhibited the lowest heat release (-850 J/g) of all five inerting materials tested in this study when integrated from room temperature to 800 °C. The heat absorption performance for sodium bicarbonate (SBC), with a mixture heat release of -184 J/g, was slightly lower compared to PK.

The DSC profiles for cornstarch and carbonate/cornstarch mixtures are shown in Figure C.6. SBC and PK display similar behaviors when allowed to decompose in a 1:1 wt % mixture with organic cornstarch. The heat flow profiles for both agent mixtures indicate the release of moisture from cornstarch when heating to 100 °C (endothermic heat flow) and show a catalyzed exothermic mixture decomposition occurring between 250 and 325 °C, which is well before the onset of the characteristic cornstarch combustion range. Not apparent with PK, the DSC profile for the cornstarch and SBC mixture decomposition produces a secondary fuel combustion step, which corresponds to a narrow, high-magnitude exotherm, at approximately 570 °C. In regard to the way that these agents behave as the mixture degrades, the main difference between PK and SBC is the slope of the heat signature following the initial heat release for the mixture. For the PK mixture, a greater negative slope signifies that this inert material has an increased capability to absorb the exothermic heat from the sustained fuel combustion. For higher fuel to agent mixture ratios, the linear segment would be expected to approach a zero slope as the capacity to absorb additional heat decreases. Confirmed by literature and the corresponding TGA profile shown in Figure B.2, the degradation mechanism for PK is as follows.[56]

$$2KHCO_{3_{(s)}} \rightarrow K_2CO_{3_{(s)}} + CO_{2_{(g)}} + H_2O_{(g)} \qquad \text{(R4)}$$

$$K_2CO_{3_{(s)}} \rightarrow CO_{2_{(g)}} + K_2O_{(s)} \quad \text{(R5)}$$

The first inhibitor decomposition step takes place between 100 to 200 °C and produces water vapor and carbon dioxide, which act as gaseous inert heat sinks and offer mass transport resistance by reducing diffusion of oxygen onto the solid surface via dilution. Potassium carbonate (K_2CO_3) is the solid-state material present during the cornstarch decomposition temperature range and has a constant pressure molar heat capacity of 114.4 J/mol^{-1} K^{-1} at 298 K, which is slightly higher than that of sodium carbonate (112.3 J/mol^{-1} K^{-1} at 298 K) and provides potassium carbonate an advantage for thermal inhibition.[67] The second step involves the dissociation of potassium carbonate at higher temperatures (850 to 1200 °C) into potassium oxide. This decomposition step occurs after the cornstarch combustion temperature range and therefore does not affect the inhibition efficiency of the agent. The mechanism for SBC decomposition is identical to that of PK, except for the substitution of Na for K.

MAP, DAP, and Met-L-X provided minimal inhibition of cornstarch combustion. The DSC profile for the mixture of cornstarch and Met-L-X (shown in Figure C.8) illustrates that sodium chloride appears to promote intensified exothermic fuel decomposition, with the mixture releasing more heat (986 J/g) than emitted during cornstarch combustion without inhibitor. The inability of these agents to mitigate the fuel combustion may be attributed to the position of their decomposition temperature range. As shown by inhibitor TGA profiles (Figures B.3, B.4, and B.5), the decomposition of these three agents occurs toward the end of the cornstarch decomposition temperature range (or completely afterwards, as in the case of Met-L-X). Principal agent decomposition at temperatures greater than the fuel combustion temperature range eliminates the potential for chemical inhibition which can reduce free radicals that sustain continued growth of the propagating flame front. In the case of these three agents, the inhibition is primarily physical;

inerting relies solely on the heat capacity, thermal conductivity, and absorptivity of the agent but lacks assistance from gaseous volatiles which would normally impede the combustion kinetically.

Oxidation modes for organic fuels are less complex than those for metal powders. Direct overlap of agent and organic fuel decomposition is not always necessary to achieve effective combustion suppression through only physical inhibition. As long as dissociation of the suppressant agent occurs prior to the onset of fuel combustion, inert gas decomposition products have the potential to complement the thermal absorption properties of the agent or of any other solid state decomposition products. However, metal fuel propagation has more complicated mechanisms of combustion and requires enhanced techniques for inerting, including dependency on chemical inhibition as an effective supplement to standard physical mitigation.

3.4.2. Zinc Powder (Zn-101) as Fuel

Applying the same analytical technique as described in Section 3.4.1, 1:1 wt % mixtures of zinc powder and inhibitors were assessed using TGA and DSC. Similar to the organic fuel/agent mixture evaluation, the DSC profiles shown in Figures C.9, C.10, and C.11 were integrated to yield the effective amount of heat released (or absorbed) during mixture decomposition. Lower heat flow over the combustion temperature zone results in a more efficient the inhibition of the fuel combustion. The DSC peak integrations were performed over the entire liquid-phase zinc combustion range (400 to 750 °C). The cumulative results of these peak integrations are provided in Table C.2.

In comparison to the heat released during zinc decomposition (3617 J/g), suppressant candidates SBC, PK, and Met-L-X demonstrate limited suppression of zinc combustion due to their predisposition toward physical mitigation (agent decomposition only exists before or after the fuel combustion window). Heat flow signatures for zinc powder mixed with carbonate

inhibitors, SBC and PK, are shown in Figure C.9. The primary mixture combustion exotherm is within the original zinc oxidation temperature range. Relying on physical inhibition (as discussed for SBC and PK in Section 3.4.1) worked well for cornstarch combustion mitigation but only slightly reduces the quantity of heat released during zinc powder combustion. The DSC profile for zinc powder mixed with the Met-L-X inhibitor is shown in Figure C.11. The agent appears to catalyze the onset of fuel combustion at lower temperatures and does little to reduce the exothermic heat released during fuel decomposition. Liquid-phase sodium chloride decomposition in the mixture occurred after the metal combustion (between the melting point and 1100 °C), therefore reducing the potential for partial chemical inhibition. The unexceptional efficiency of sodium chloride as a suppressant for zinc combustion relies solely on the thermal absorption properties of the agent (constant pressure heat capacity of 50.5 J/mol^{-1} K^{-1} at 298 K).[67]

Phosphate-based suppressant agents MAP and DAP exhibit substantially improved suppression performance, reducing the quantity of heat released over the fuel combustion range to 806 J/g and 203 J/g, respectively, as shown in Figure C.10. When the DAP and zinc mixture is heated, the principal exothermic peak is nearly nonexistent, essentially demonstrating full suppression of the fuel oxidation. The efficiency of combustion mitigation can also be assessed by examining the increase in the mass of the mixture as zinc oxide is generated (see zinc/inhibitor mixture TGA profiles, Appendix B). Larger percent mass increase during zinc combustion indicates that the reaction progresses uninterrupted and that the inhibitor is less effective in dampening the oxidation rate. During combustion, mixtures of zinc fuel with DAP, MAP, SBC, and PK demonstrate an equivalent rise in mixture mass percent of 4, 7, 9, and 11 wt %, respectively. This trend of increasing sample weight change through the combustion zone correlates well with the increase in heat released (and decrease in inhibition effectiveness), as

shown by the integration results in Table C.2. Amplified heat absorption efficiency for MAP and DAP can be explained in part by the corresponding agent decomposition mechanism:

$$(NH_4)_2HPO_{4(s)} \rightarrow NH_{3(g)} + NH_4H_2PO_{4(s)} \quad \text{(R6)}$$

$$(NH_4)_2HPO_{4(s)} \rightarrow 2NH_{3(g)} + H_3PO_{4(l)} \quad \text{(R7)}$$

$$NH_4H_2PO_{4(s)} \rightarrow NH_{3(g)} + H_3PO_{4(l)} \quad \text{(R8)}$$

$$4H_3PO_{4(l)} \rightarrow 2H_2O_{(g)} + 2H_4P_2O_{7(l)} \quad \text{(R9)}$$

$$2H_4P_2O_{7(l)} \rightarrow 4H_2O_{(g)} + P_4O_{10(s)} \quad \text{(R10)}$$

Reaction mechanism steps R6 through R10 are applicable for DAP decomposition, while MAP dissociation occurs exclusively via steps R8 through R10. In comparison to MAP, DAP has a larger constant pressure molar heat capacity (141.4 J/mol^{-1} K^{-1} and 188 J/mol^{-1} K^{-1} for MAP and DAP, respectively, at 298 K) and greater potential for physical heat absorption.[67,68] Both sets of decomposition reactions produce the inert gas ammonia (as per reaction stoichiometry, four times more ammonia generation following DAP dissociation), which acts as a buffer against sustained mass and heat transfer on the particle surface. Obstruction of active reaction sites successfully limits diffusion of oxygen, restricting continued fuel particle preheating and volatilization. In industrial prevention or mitigation application, this corresponds to arrested flame temperatures and lower concentrations of oxidant, which thereby introduces significant ignition time delay. However, the ability to inhibit chemically, combined with the aforementioned physical inhibition characteristics, is what distinguishes the performance of MAP and DAP. The degree of chemical inhibition corresponds to the proximity of primary inert decomposition in relation to the fuel combustion zone. Since the primary agent decomposition (approximately 35% reduction of total sample weight for MAP and 45% reduction of total sample weight for DAP, as supported by TGA profiles in Figures B.3 and B.4, respectively) directly overlaps with the fuel combustion

temperature zone (400 to 750 °C), intermediate species of ammonia and amino radicals are actively present to consume oxygen and other free radicals (·O, ·OH, ·H) that would normally prolong fuel propagation. Although these intermediate reactants and products exist in low concentrations due to their relative instability, radical-consuming intermediate reactions compete for oxygen and are nevertheless vital for enhancing the efficiency of chemical inhibition. Unlike the mixture trials containing SBC or PK, greater availability of oxygen-consuming intermediate reactions during MAP and DAP decomposition allows for reduced oxygen radical concentrations within the reaction zone, resulting in regulated exothermic heat and limited flame temperatures.[58] Examples of such transient intermediate mechanisms are shown in Reactions R11 through R15:

$$NH_3 + \cdot OH \rightarrow \cdot NH_2 + H_2O \quad \text{(R11)}$$

$$NH_3 + \cdot H \rightarrow \cdot NH_2 + H_2 \quad \text{(R12)}$$

$$NH_3 + \cdot O \rightarrow \cdot NH_2 + \cdot OH \quad \text{(R13)}$$

$$\cdot NH_2 + O_2 \rightarrow NHO + \cdot OH \quad \text{(R14)}$$

$$\cdot NH_2 + \cdot O \rightarrow \cdot NH + \cdot OH \quad \text{(R15)}$$

3.4.3. Iron Powder (Fe-101) as Fuel

Preliminary suppression testing on iron powder deflagrations in the 1 m^3 sphere combustion chamber demonstrated nearly equivalent performance for SBC and PK at the same agent concentration. Additionally, DAP exhibited extremely poor bulk flow properties upon injection into the combustion volume and lacked functionality on an application setting (minimal agent dispersion results in inadequate flame coverage during system discharge). For these reasons, all continued thermal analysis and eventual suppression testing will utilize SBC, MAP, and Met-L-X as the primary suppressant agent candidates. DSC analysis of iron powder decomposition is overlaid with DSC analysis of iron/inhibitor mixtures in Figure 3.6. Integration of DSC heat flow

profiles over the iron powder combustion temperature range (200 to 800 °C) yielded the total heat release during sample decomposition and was performed via analytical techniques, as illustrated in Figure 3.7. Results from the integration of these DSC heat flow signatures are documented in Table 3.3.

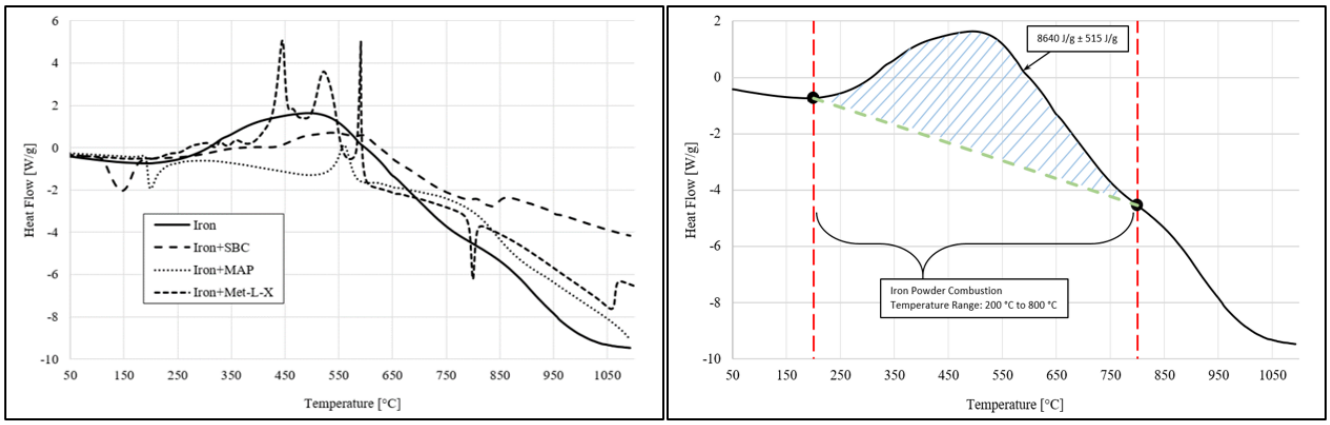

Figure 3.6 (left) & Figure 3.7 (right). Differential scanning calorimetry profile for iron powder fuel and 1:1 wt % iron/inhibitor mixtures (left), and illustration of DSC integration technique (right). Temperature range from 50 to 1100 °C, at a constant 10 °C/min heating rate (in air).

Relative to the heat released during iron powder combustion (8640 J/g), the decomposition of iron/inhibitor mixtures yielded a lower heat release over the temperature range of interest. This consequence is reasonable based on deconstructive interference occurring between exothermic and endothermic heat flow signatures of the fuel and suppressant agent, respectively. The outcome of reduced combustion rate is directly attributable to the degree of physical and chemical inhibition of the inert material. Releasing only 499 J/g through the iron powder combustion range, the mixture comprising of iron powder and MAP exhibited a substantially improved heat absorption efficiency when compared with suppressant agents SBC and Met-L-X.

Table 3.3. Total heat released per gram of sample during decomposition of iron powder and iron/inhibitor mixtures; integration of Figure 3.6 over the primary iron solid-phase combustion temperature range (200 to 800 °C).

Sample Composition	Σ(Peak Areas within Combustion Range) [J/g]	Average Deviation [J/g]
Fe	8640	515
Fe+SBC	4086	29
Fe+MAP	499	48
Fe+Met-L-X	5649	47

Justification for the increased inhibition efficacy of MAP is hypothesized to be dependent on the extent of overlap between fuel combustion range and the primary decomposition temperature range of the agent. Confirmed through TGA, principal MAP sample mass loss occurs from 500 to 750 °C, directly atop the iron powder combustion region (see TGA profile for MAP, Appendix B; Figure B.3). Such overlap is theorized to prompt an amplified chemical inhibition effectiveness due to increased competition for radical intermediates, which would otherwise stimulate continued fuel combustion, by transient MAP decomposition reaction intermediates (NH_3, $\cdot NH_2$).[69] Primary endothermic agent decomposition of SBC and Met-L-X, however, occurs outside of the iron powder oxidation window, as confirmed through suppressant agent TGA profiles (Appendix B; Figures B.1 and B.5, respectively), such that the agents are able to operate solely through physical inhibition mechanisms as a result of their solid-state heat capacity and dilution of oxygen content near the fuel particle surface.

3.4.4. Aluminum Powder (Al-100) as Fuel

Similar techniques for the prediction of suppressant agent performance were not possible for aluminum powder fuel due to the high fuel particle burning temperature. Met-L-X (sodium chloride) decomposes at high temperature in the liquid phase, from approximately 800 to 1000 °C (see the TGA profile for Met-L-X; Appendix B, Figure B.5), and is hypothesized to exhibit improved flame extinction effects during aluminum deflagrations. The shift of agent decomposition toward temperatures closer to high temperature aluminum powder combustion

offers an increased likelihood for chemical inhibition effectiveness via introduction of transient sodium and chloride ions. However, such theories were not verifiable through TGA and DSC analysis, as was done with iron powder and iron/inhibitor mixture samples. Figure 3.8 shows partial TGA/DSC of aluminum powder sample under air, carried out on a NETZSCH STA 449 F5 Jupiter simultaneous thermal analyzer equipped with a SiC furnace capable of operating from 25 to 1600 °C.

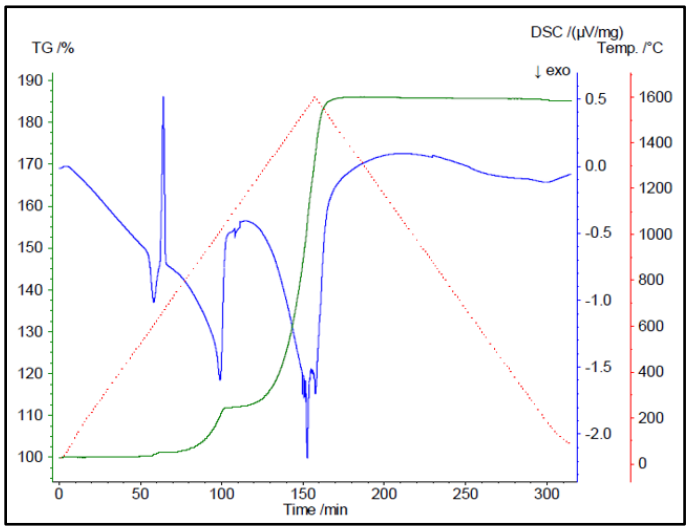

Figure 3.8. Simultaneous thermogravimetric analysis and differential scanning calorimetry profiles for aluminum powder fuel. Temperature range from 25 to 1600 °C, at a constant 10 °C/min heating rate (in air). Results courtesy of NETZSCH testing facilities.

Primary sample heat release begins within the liquid phase, following the endotherm of melting at 660 °C.[67] The sample exhibited three mass gain steps totaling approximately 71% when heated at a constant 10 °C/min rate. All mass gain rate peaks coincide with DSC exotherm peaks at 604 °C, 1017 °C, and 1553 °C. However, instrument operation up to only 1600 °C was unable to reveal complete sample oxidation; thus, the analysis of aluminum and inhibitor mixtures would not exhibit useable data since higher-temperature liquid- and vapor-phase exotherms are not visible.

3.5. Analysis of Suppressant Decomposition Products via Mass Spectrometry

Prior to suppression testing on a large scale, appropriate measures were taken to assess the toxicity concerns associated with heating a substantial quantity of metal/inhibitor mixture to high burning temperatures. To appropriately identify the agent decomposition volatiles, TGA-DSC experiments were performed, with evolved gas analysis via mass spectrometry (MS). All samples were measured on the NETZSCH STA 449F1 Jupiter thermal analyzer coupled with the NETZSCH QMS 403 Aeolos mass spectrometer. All MS ion-current curves are shown within the Appendix D. Such curves for thermal decomposition of SBC under air are displayed in Figure D.1. Evolutions at mass numbers 18 and 44 can be attributed to water (H_2O: MW – 18) and carbon dioxide (CO_2: MW – 44), respectively. Both of these peaks show upmost intensity during the initial decomposition of sodium bicarbonate at approximately 150 °C. Carbon dioxide is evolved at higher temperatures (maximum peak intensity at 669 and 1147 °C) during the secondary decomposition of sodium carbonate. Mass numbers of fragmented ions associated with water (mass number 17) and carbon dioxide (mass number 12) are also present on the MS curve profile. This evolved species analysis aligns directly with literature proposed decomposition mechanism shown in Reactions R16 and R17 below.[69]

$$2NaHCO_{3_{(s)}} \rightarrow Na_2CO_{3_{(s)}} + CO_{2_{(g)}} + H_2O_{(g)} \quad \text{(R16)}$$

$$Na_2CO_{3_{(s)}} \rightarrow CO_{2_{(g)}} + Na_2O_{(s)} \quad \text{(R17)}$$

MS ion-current curves for thermal decomposition of Met-L-X under air are displayed in Figures D.2, D.3, and D.4. As with SBC decomposition, thermal degradation of Met-L-X releases CO_2 and H_2O, with greatest peak intensity at multiple temperatures below 600 °C (see Figure D.2). The TGA and associated MS curves for mass numbers 35, 36, 37, and 38 are plotted in Figure D.3. The most probable evolutions attributed to these mass numbers are hydrogen chloride (HCl: MW

– 36) and its associated fragmented ions. HCl evolution reaches maximum peak intensities at approximately 270 and 1100 °C. The TGA and associated MS curves for mass numbers 70, 72, and 74 are plotted in Figure D.4. The most probable evolution attributed to these mass numbers is chlorine (Cl_2: MW – 70), or other chlorinated organic species. Chlorine evolution reaches maximum peak intensity exclusively at the high temperature degradation region (1100 °C), during which approximately 90% of the sample weight loss occurs.

MS ion-current curves for thermal decomposition of MAP under air are displayed in Figures D.5, D.6, and D.7. The TGA and associated MS curves for mass numbers 15, 17, 18, and 19 are plotted in Figure D.5. The most probable evolutions attributed to these mass numbers are H_2O and ammonia (NH_3: MW – 17), as well as accompanying fragmented ions, with maximum peak intensities occurring at 215, 350, and 455 °C. The TGA and associated MS curves for mass numbers 30 and 44 are plotted in Figure D.6. The most probable evolutions attributed to these mass numbers are nitric oxide (NO: MW – 30) and nitrous oxide (N_2O: MW – 44), with trace quantities evolving between 200 and 600 °C. The TGA and associated MS curves for mass numbers 35, 36, 48, and 64 are plotted in Figure D.7. The intensities of these evolutions are trivial relative to other evolved species. The mass numbers can likely be attributed to the species HCl and sulfur dioxide (SO_2: MW – 64), as well as the related fragments of these components. Both SO_2 and fragmented ion SO_2 (mass numbers 64 and 48, respectively) show maximum peak intensity at 390 and 475 °C. Both HCl and fragmented ion HCl (mass numbers 36 and 35, respectively) show a slight increase in MS signal intensity above 800 °C. Although monoammonium phosphate contains no single molecules of chlorine or sulfur, it is likely that trace quantities of these evolved species are introduced via thermal degradation of the chemical additives and flow-promoting materials present within commercially acquired MAP. The mass loss step at approximately 600

°C does not seem to correlate with a particular mass number intensity change, signifying that the evolved species (likely a form of phosphorus oxide based on original sample composition) may have condensed to liquid phase despite a heated transfer line integrating the TGA with the MS. This evolved species analysis can be compared with the literature proposed MAP decomposition mechanism shown in Reactions R8 through R10 (Section 3.4.2).[69]

With hazards appropriately identified, agents are ready for suppression testing on a large scale using a 1 m^3 combustion sphere. The 1 m^3 combustion sphere is allowed to cool to equilibrium following suppression, and an open exhaust line provides for sufficient ventilation of potentially harmful fuel and agent decomposition products. To maintain personnel safety, use of respirators was required for post-test inspection of combustion chamber internals.

3.6. Kinetic & Thermodynamic Assessment of Fuel Combustion via DSC

Estimation of the kinetic parameters for the exothermic combustion of cornstarch, zinc, and iron is necessary for understanding of the spontaneity of these fuel decomposition reactions. Aluminum powder combustion was excluded from this assessment, as the full aluminum oxidation temperature range was not visible during DSC analysis up to 1600 °C (discussed in Section 3.4.4). According to ASTM E698, the relationship between fluctuation in heating rate and corresponding shift in exotherm peak temperature can be used to approximate the Arrhenius kinetic constants for thermally ignitable materials.[70,71] To apply this standard, the combustion reactions of cornstarch, zinc, and iron were assumed to follow first-order reaction kinetics. For all fuels, multiple DSC profiles were compiled at heating rates (β) of 5 °C/min, 10 °C/min, 20 °C/min, and 30 °C/min, and the maximum exotherm peak temperatures (T_{MAX}) were recorded. Cornstarch decomposition consisted of two primary peaks along the exotherm, while zinc and iron powder decomposition

each consisted of a single primary peak along the exotherm, as shown by DSC in Figures 3.2, 3.4, and 3.6, respectively. Based on these consolidated data sets, plots of $-Ln\,(\beta/T_{MAX}{}^2)$ versus $1/T_{MAX}$ were created for each exotherm peak. The data were fitted with a linear trend line, and the activation energy (E_a) for each decomposition peak was determined using the slope, as shown below in Equation E5:

$$slope = -\frac{E_a}{R} \tag{E5}$$

where R is the gas constant. The assumption of first-order kinetics was confirmed based on the linearity of the data points. The pre-exponential factor (A) was calculated using Equation E6 as described in ASTM E698:

$$A = \beta \frac{E_a}{RT_{MAX}^2} e^{E_a/RT_{MAX}} \tag{E6}$$

The rate constant (k), as a function of system temperature, can be calculated using the activation energy and pre-exponential factor, as shown in Equation E7. This analysis assumes that rate constants are measured in the absence of both internal and external mass transfer limitations.

$$k = Ae^{-E_a/RT} \tag{E7}$$

Once rate constant correlations were established for each exotherm peak, transition state theory and the Eyring-Polanyi equation (Equation E8) were utilized, in which k_B and h represent the Boltzmann's constant and Planck's constant, respectively.[70-72] A plot of $-Ln\,(k/T_{MAX})$ versus $1/T_{MAX}$ was generated for all exotherm peaks. Following linear fitting of the data, the slope was utilized to determine the enthalpy of activation (ΔH), and the y-intercept was utilized to determine the entropy of activation (ΔS).

$$Ln\left(\frac{k}{T_{MAX}}\right) = -\frac{\Delta H}{R}\frac{1}{T_{MAX}} + Ln\left(\frac{k_B}{h}\right) + \frac{\Delta S}{R} \tag{E8}$$

The Gibbs free energy of activation (ΔG) for each decomposition peak can then be calculated using the following fundamental thermodynamic relationship:

$$\Delta G = \Delta H - T\Delta S \tag{E9}$$

Positive values for Gibbs free energy of activation represent an endergonic reaction, in which the system requires an input of energy. In a dynamic combustion environment, larger values for ΔG signify more free energy available to promote flame front propagation and heating of surrounding particles. The activation entropy describes how energy must be redistributed through the molecule before reaction initiation is able to occur. Molecular geometry, orientation in space, and viable degrees of freedom exhibit substantial influence on the entropy of activation. Transition state theory offers explanation for rates of elementary reactions by assuming quasi-chemical equilibrium between reactants and higher-energy activated transition state complexes.[72,73] In support of this concept, activation enthalpy signifies the change in enthalpy from the initial reactant state to the reactant-product hybrid transition state and is typically comparable in magnitude to the activation energy. Higher values of activation enthalpy and activation energy indicate a reduced reaction rate, as is the case for the second peak in cornstarch decomposition (see DSC profile, Figure 3.2). This peak represents incomplete combustion and leads to formation of carbon monoxide due to insufficient presence of oxidizer and poor mixing of the fuel/air interface. Utilizing methodology from ASTM E698 followed by application of the Eyring-Polanyi equation, kinetic parameters and thermodynamic state functions were modeled for all fuel combustion peaks and are shown in Table 3.4.

Table 3.4. Calculated activation energies and thermodynamic state quantities for cornstarch, zinc, and iron powder combustion; values derived from analysis of DSC heat signatures by means of the technique documented within ASTM E698 and through utilization of the Eyring-Polanyi Equation.

Fuels	**E_a [kJ/mol]**	**ΔH [kJ/mol]**	**ΔS [J/K/mol]**	**ΔG [kJ/mol]**
CS Peak 1	20.4	21.2	-217.1	167.8
CS Peak 2	60.3	60.5	-149.6	179.4
Zinc Powder	41.9	41.5	-207.5	232.0
Iron Powder	32.4	26.4	-236.8	243.8

Other modelling techniques can be additionally employed to assess the degree of combustion rate control by diffusion and kinetics. The shrinking particle model is commonly utilized for simplistic non-catalytic irreversible first-order reactions between solid fuel and surrounding gas film. Another more complicated technique, known as the shrinking unreacted core model, assumes that a reaction front moves from the surface through the solid particle interior and leaves behind a permeable product layer. Unlike the previous model which only considered the chemical reaction rate and diffusion of oxygen through the gas film boundary, the shrinking unreacted core model takes diffusion through a porous product layer (between the gas film and unreacted solid core) into account as well. Depending on the combination of transport and kinetic resistances, a principal aim of these models is to establish correlations for fuel burnout time. From an application standpoint, longer particle burning durations may require extended suppressant agent discharge, such that the inertant injection continues for the entirety of the fuel combustion. These considerations are crucial to large-scale mitigation designs, especially when suppressant agents of varying packed densities tend to exhibit unique dispersion rates and cloud profiles.

3.7. Conclusion

Metal dusts explosion hazards continue to present a significant threat in a wide variety of process industries. Utilizing the DSC heat flow signature of pure metal fuel sample as a baseline, peak integration analysis yielded that the 1:1 wt % mixture of ammonia-based agents (diammonium phosphate [DAP] and monoammonium phosphate [MAP]) with zinc and iron metal powder samples demonstrated the greatest reduction in exothermic heat release in comparison to other suppressant agent materials tested. Significant endothermic DAP and MAP decomposition (>30% of initial sample weight) occurs over the same temperature range during which zinc and iron oxidation takes place. Similar principal decomposition temperature ranges for the fuel and agent provide greater potential to inhibit combustion chemically through consumption of free radicals that would ordinarily sustain ongoing fuel propagation. The results of this study support the need for explosion protection design solutions which exploit particular suppressant materials uniquely tailored toward specific fuel types.

The overlap of fuel and agent decomposition temperature range increases the inhibition effectiveness of the agent and brings industrial applications closer to a refined solution for preventative inerting and active explosion mitigation. An increase in chemical inhibition moderates the necessity for physical (thermal) inhibition. For deflagration mitigation through active suppression, this corresponds with lower agent concentrations required to achieve tolerable (relative to equipment design strength) suppression pressures after system activation. If performance can be maintained by using reduced quantities of inertant material and fewer hardware components, this offers a less expensive and thus more attractive option for customers conveying reactive metal dusts. Currently, active suppression designs for metal dust fuels

commonly utilize SBC at high concentrations, attempting to compensate physically for the agent's lack of chemical inhibition capability.

The notion of heightened chemical inhibition due to overlap of the decomposition temperature range may be applicable to other more reactive metal fuels. Aluminum powder displays a progressively complex and spontaneous combustion mechanism due to failure of the particulate oxide shell at measured ignition temperatures as high as 2100 °C.[74] As demonstrated in the TGA profile for Met-L-X (Appendix B, Figure B.5), sodium chloride decomposition is shifted toward higher temperatures (800 to 1000 °C), amplifying the probability for chemical inhibition during high-temperature aluminum powder combustion. Inhibition materials best-suited for mitigation of iron and aluminum fuel propagation will be examined further through suppression testing in Fike Corporation's 1 m^3 combustion sphere. Results and discussion pertaining to this effort are presented in Chapter 4. Emphasis on agents with anticipated performance, as predicted from thermal analysis, allows for a more intensive suppression test program. Thus, continued large-scale testing will only assess the efficacy of suppressant agent candidates SBC, MAP, and Met-L-X.

Material flow properties such as gas permeability, bulk density, cohesiveness, floodability, and compressibility are important characteristics to consider for effectively dispersing agents into the protected volume during high-rate pressurized injection at the onset of deflagration development. Although DAP appeared to exhibit optimal anticipated mitigation performance for mid-range oxidation metals, it does not demonstrate ideal bulk flow characteristics. From an application standpoint, limitation in agent discharge velocity is likely to either put system response time in jeopardy or reduce the rate of agent concentration provided during injection. Suppressant agents SBC, MAP, and Met-L-X seem to demonstrate adequate bulk fluidization with no concerns of

material agglomeration. However, such qualitative observations will be confirmed prior to active suppression experiments. Results pertaining to open-air dispersion testing and high-speed videography analysis are presented in Chapter 4.

As described in NFPA 69, active explosion suppression designs shall be based on the following key factors: time required for detection, suppressant discharge pattern, suppressant concentrations as a function of time (injection duration), suppressant efficiency, explosibility of the combustible material, and physical characteristics of the protected enclosure.[30] A majority of these variables are limited by the hardware of the explosion protection system manufacturer or by the application in question, but the fourth item in this list (suppressant efficiency) is predominantly dependent on physical and chemical inhibition capacity of the suppressant material, which acts as the primary focus of this study. In light of escalating doubts surrounding the scalability of 20 L sphere explosibility and inerting testing, this work offers a novel analytical technique for characterization and screening of suppression agents based on efficiencies predicted through integration of fuel and fuel/agent mixture DSC heat flow profiles.[75,76]

Chapter 4: Large-Scale Validation Testing of Suppressant Performance

4.1. Experimental Objectives and Procedures

4.1.1. Open-Air Dispersion

Suppressant materials of different chemical composition have the potential to exhibit significant variation in physical properties such as cohesiveness, gas permeability, bulk density, compressibility, and floodability. When injected into an open volume under high pressure, these characteristics can often correlate to fluctuating dispersion profiles, flow distributions, and discharge velocities. Before utilizing new inhibitor materials in a contained volume for the mitigation and extinction of developing deflagrations, open-air dispersion testing is necessary to validate the injection performance of all three suppressant agents (SBC, Met-L-X, and MAP). If a particular agent does not meet expectations during suppression testing, it may be difficult to decide whether the cause is limited dispersion during injection or poor inhibition effectiveness. Open-air discharge testing beforehand will eliminate such doubts. To fairly evaluate suppression data, open-air dispersion shots are required to ensure that the plume of injected inhibition material behaves similarly for all three agents under analysis, with SBC acting as the benchmark for comparison.

A total of six tests were performed, with two identical tests for each agent to confirm repeatability of discharge performance. A 10 L high-rate discharge (HRD) container was utilized for all experiments to retain a uniform agent delivery rate. To maintain equivalent nitrogen headspace volume in all tests, a constant powder volume of 6.8 L was charged into the container. Based on the measured packed densities for all materials (Appendix E, Table E.1), this volume coincides with fill weights of 9.07 kg, 5.90 kg, and 4.08 kg for SBC, Met-L-X, and MAP, respectively. Once loaded with powder and sealed, the HRD container was mounted onto a custom-built test gantry at a firing angle of 45° and pressurized with nitrogen to 900 psig (62.1

barg), which served as the primary driving force for high-rate discharge of suppressant agent through a Fike standard spreader nozzle assembly. The container was equipped with a pressure transducer to measure the pressure inside the HRD headspace as a function of time following system activation. Vertical and horizontal markers with one foot spacing increments were positioned in front of the gantry and are necessary when calibrating high-speed experimental software utilized during post-test videography analysis. Initiation of HRD container discharge in all tests was a result of gas cartridge actuator (GCA) remote firing via a 24 VDC power supply. A visual representation of the experimental mounting setup is shown in Figure 4.1.

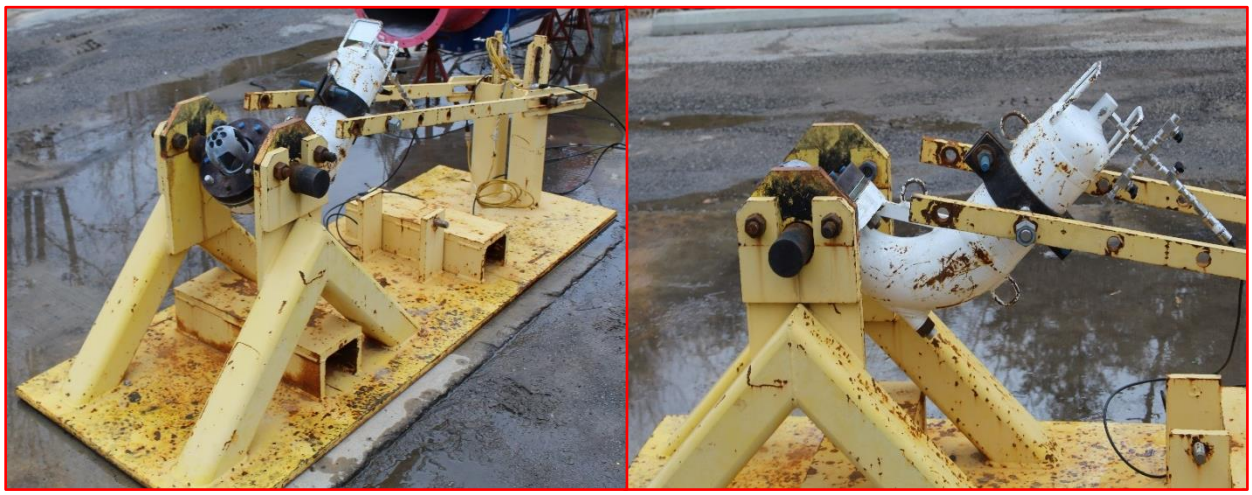

Figure 4.1. Test setup for open-air dispersion testing, overall setup (left) and container detail (right); a 10 L HRD container with a standard Fike spreader nozzle assembly, mounted to the gantry at a 45° firing angle.

All tests were recorded with a real-time video camera running at 30 frames per second and with a high-speed video camera running at 1,000 frames per second. High-speed videography was necessary for post-test analysis. A flash bulb, placed in view of the cameras, was activated at the time of GCA initiation, allowing for the synchronization of data acquisition and high-speed video. Using the flash bulb frame as “time zero”, reciprocal (inverse) velocity calculations were made at multiple agent throw distances (from origin out to 4.57 meters) based on data points pulled from high-speed video analysis using “i-Speed” software suite.

In addition to inverse velocity measurements, data captured from the HRD pressure transducer and qualitative visual inspection subsequent to discharge were necessary for complete assessment of agent dispersion through comparison of the following post-test deliverables:

- T90, the time required to reduce the nitrogen pressure within the HRD container to 10% of the initial preactuation pressure (90% discharged),
- T03, the time required to reduce the nitrogen pressure within the HRD container to 97% of the initial preactuation pressure (3% discharged),
- Weight of residual powder left in the container following discharge,
- Confirmation that the rupture disc opening is complete and non-fragmenting, and
- Visual comparison of dispersion profile through inspection of high-speed videography at specific time frames

4.1.2. 1 m^3 Sphere Explosibility and Suppression

Displayed in Figure 4.2, the 1 m^3 combustion sphere is a high-strength enclosure (21 barg equipment design pressure) comprised of two carbon steel hemispherical sections and used primarily for closed-vessel fuel explosibility analysis as per international standard ISO 6184-1 and ASTM E1226.[77,78] The 1 m^3 combustion chamber is capable of being reconfigured with HRD container mounting, a requirement for suppression testing. Details on the concept of active suppression as a deflagration mitigation strategy were introduced in Section 1.4. Such discussion includes the potential use of measurable TSP as a direct indicator for suppressant agent performance. For both explosibility and suppression testing, ignition energy was consistently provided using two 5 kJ chemical igniters positioned in the center of the sphere.

Unsuppressed explosibility analysis is essential for determination of fuel reactivity in the form of maximum observed pressure (P_{max}) and deflagration index (K_{St}), which is proportional to the maximum rate of pressure rise within the contained volume during fuel combustion. At constant ignition energy and initial pressure, the deflagration reactivity is dependent on the ignition time

delay following initiation of fuel dispersion. Reduced ignition time delay induces more aggressive K_{St} due to added effects of injection turbulence. Increased ignition delay allows turbulence dissipation and a portion of the injected fuel particles to fall out of suspension, leading to suspended concentrations lower than anticipated and resulting in a restricted measurement of K_{St}. Larger concentrations of suspended fuel require dual dispersion (injection via two separate dispersion vessels) to ensure that all fuel is fully injected into the combustion volume prior to ignition, as was the case for all iron deflagration explosibility and suppression tests performed at an increased suspended fuel concentration of 2,250 g/m³. To guarantee complete injection of fuel, the initial fuel load mass was equally divided among, and simultaneously injected from, each of the two injectors. Fuel injection points were positioned on opposing sides of the 1 m³ combustion sphere, with dispersion nozzles placed at contrary vertical and horizontal orientations in order to provide a uniform distribution of fuel.

Figure 4.2. Fike Corporation 1 m^3 combustion test vessel, utilized for fuel explosibility and active suppression testing.

4.2. Discussion of Results

4.2.1. Open-Air Dispersion

The results of this test program act as a necessary supplement for continued application of novel agents toward metal dust deflagration suppression research. Despite varying flow properties and particulate densities, dispersion of all three agents appeared visually sufficient to move forward with suppression testing in the 1 m^3 combustion sphere. Although this study was meant to be primarily a qualitative check on the injection proficiency, quantitative deliverables and analysis mentioned in Section 4.1.1 produced a similar assessment.

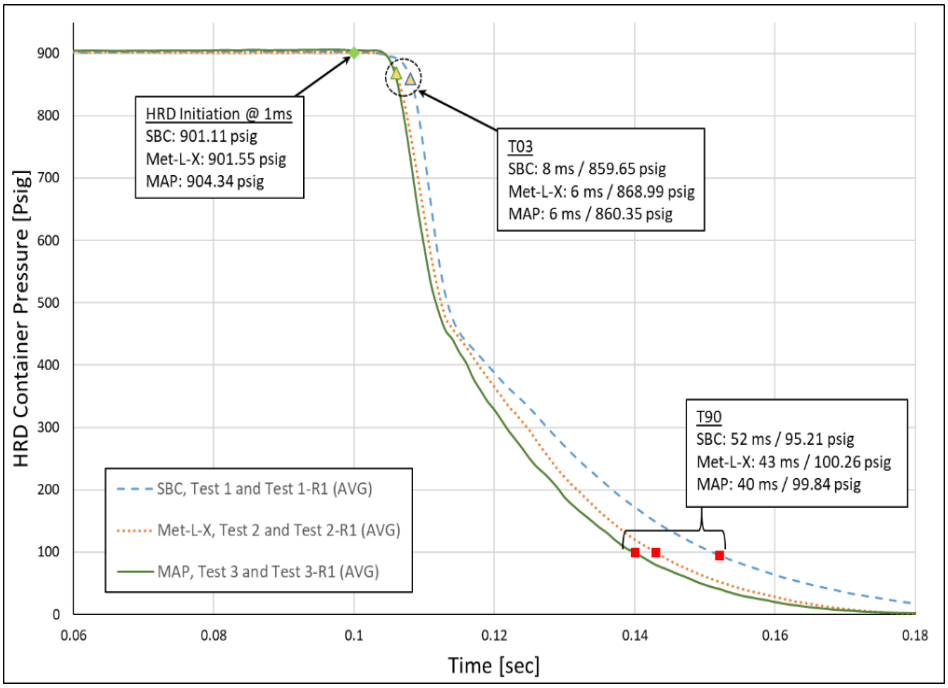

Figure 4.3. Average container pressure as a function of time following HRD initiation (data reported from t = 0.06 to 0.18 s), acting as a qualitative assessment of T03 and T90 differentiations between tests of varying agent types.

Pressure transducer measurements of the container headspace pressure as a function of time allowed for determination of T03 and T90 for all tests. Discharge of suppressant agents MAP and Met-L-X exhibited a lower T03 (6 ms) compared to that of SBC (8 ms), likely a consequence of variable powder decompression rates. Immediately following rupture disc opening, bridging of

compressed powder begins to propagate toward the headspace volume. As the agent packing begins to break apart, interparticulate expansion and expulsion of bulk agent (as plug flow) promptly follow. Dissimilarities in T03 thus describe differences in the time to effectively fluidize the compressed agent, which is hypothesized to be a function of variable agent particulate densities. Additionally, the average T90 times for MAP and Met-L-X (40 ms and 43 ms, respectively) were significantly lower than that of SBC (52 ms), a direct result of lesser initial mass charged into the HRD container. The average HRD container pressure as a function of time following HRD initiation is demonstrated in Figure 4.3 for all three suppressant agents under investigation, with T03 and T90 results for each individual test documented in Table 4.1.

Table 4.1. Post-test deliverables for open-air dispersion testing, including measured T90 and T03, suppressant weight left in the container following discharge, and confirmation of complete, non-fragmenting rupture disc opening.

Test No.	Container Size	Suppressant Agent	Actual Suppressant Fill Weight (kg)	Measured T90 (ms)	Measured T03 (ms)	Post-Test Residual Powder Weight (lbs)	Complete and Non-Fragmenting RD Opening (Y/N)
1	10L HRD	SBC	9.07	52	8	0.054	Y
1-R1	10L HRD	SBC	9.07	56	8	0.082	Y
2	10L HRD	Met-L-X	5.90	44	6	0.018	Y
2-R1	10L HRD	Met-L-X	5.90	46	6	0.036	Y
3	10L HRD	MAP	4.08	44	6	0.018	Y
3-R1	10L HRD	MAP	4.08	40	6	0.023	Y

Qualitative evaluation of plume geometry likewise demonstrates adequate agent dispersion relative to SBC and eases reservations in regard to continued suppression testing. Figure 4.4 illustrates images captured from high-speed videography at 75 ms following HRD initiation and offers a direct visual comparison of plume distribution for each agent. Plume geometries of SBC and Met-L-X discharge appear nearly identical; all three plume segments are well-formed and comparable in extent. The plume for MAP discharge possesses less distinguishable plume segments (rather, identifies as one single cloud) but still covers roughly the same distances at short times follow system initiation (increased dispersion lag apparent at larger time/throw). Thus, the

high-pressure driving force appears to outweigh differences in agent flow properties, such that all agents display similar coverage behavior during discharge.

Figure 4.4. Comparison of plume geometries during open-air discharge testing, including Test No. 1-R1 with SBC (left), Test No. 2 with Met-L-X (middle), and Test No. 3 with MAP (right); images captured at 75 ms following system activation.

Figure 4.5 offers visual depiction of a characteristic cloud profile. Subdivisions of the plume are labeled accordingly as Track Point 1 (lower segment), Track Point 2 (middle/primary segment), and Track Point 3 (upper segment). This nomenclature is essential for data set identification and proper review of inverse velocity data. Annotation lines are also evident, on which data points were collected at 5 ms increments following HRD initiation.

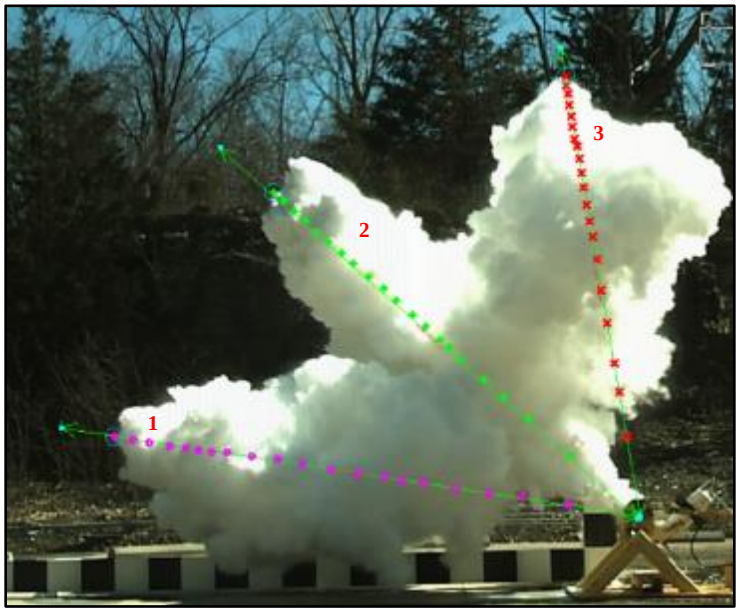

Figure 4.5. Illustration of dispersion profile during open-air discharge testing (Test No. 2-R1, with Met-L-X powder); subdivisions of the plume (Track Point 1, Track Point 2, and Track Point 3) labeled accordingly in red.

Table E.2 within Appendix E displays reciprocal velocity data for the central segment of the cloud profile (Track Point 2). The values reported are calculated averages of both the original test and the repeat test for the same agent type. Values are provided at arbitrary throw distances of 0.91, 1.83, 2.74, 3.66, and 4.57 meters. Inverse velocities were determined with respect to the previous frame (instantaneous inverse velocity) and with respect to the user-defined custom origin position (bulk average inverse velocity). This custom origin position is expressed as the location where powder first exits the HRD container. For instantaneous inverse velocity measurements at higher target throw distances, the relative impact of perturbations increases as the dispersed agent loses momentum and is prone to influence by non-stagnant air flow from the surrounding environment.

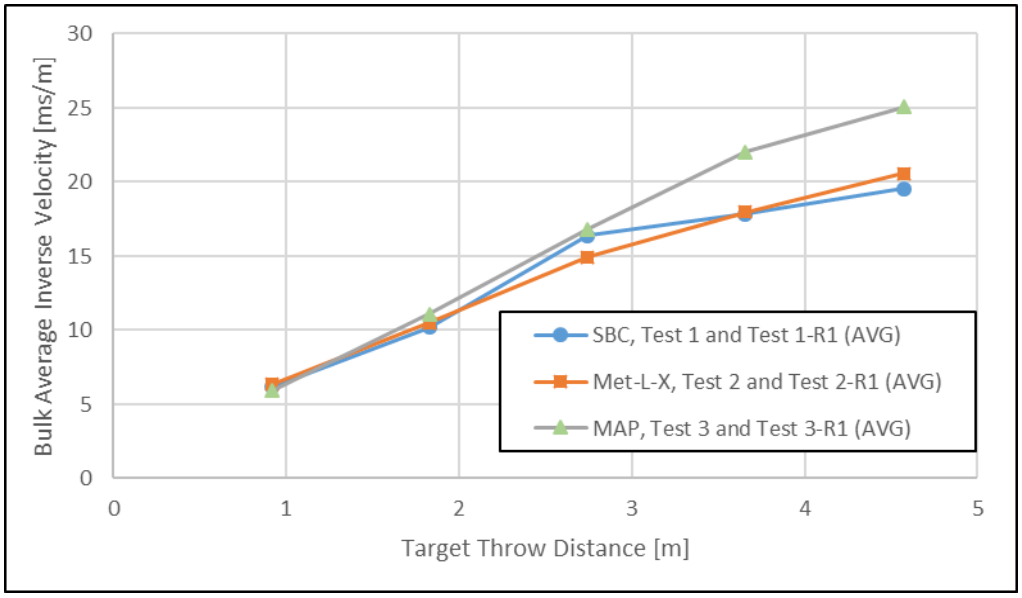

Figure 4.6. Bulk average inverse velocity results (measured with respect to custom user-defined origin) plotted for all suppressant agent as a function of increasing target throw distance.

The average bulk inverse velocity data with respect to the custom origin are plotted in Figure 4.6. Results exhibit extremely similar inverse velocities for SBC and Met-L-X. This consistency in inverse velocity between SBC and Met-L-X, even at a larger target throw distance of 4.57 meters

(± 1.44 ms/meter), is seemingly due to their comparable particulate crystal densities (2.20 and 2.16 g/cm³ for SBC and sodium chloride, respectively).[67] As a result of a considerably lower crystal density (1.80 g/cm³ for MAP), measured inverse velocities for MAP dispersion showed greater deviation from SBC dispersion, more noticeably so at throw distances greater than 2.74 meters (± 4.17 ms/meter at 3.66 meters and ± 5.51 ms/meter at 4.57 meters). At larger target throw distances, the discharge of MAP coincided with an increased time-to-cover and a limited penetration power, again likely due to the significantly lower particulate density compared to the other agents tested. All aforementioned deviations are based on the average bulk inverse velocity data reported in Table E.2 within Appendix E.

Figure 4.7. Post-test evaluation; validation that HRD rupture disc opening is complete and non-fragmenting; Test No. 1-R1 with SBC.

Post-test quantification of the residual suppressant weight left in the container was recorded as another auxiliary deliverable and is presented within Table 4.1. All SBC open-air dispersion tests resulted in >0.05 kg of residual powder left in the container (an average of 0.75% of the initial mass), while all MAP and Met-L-X tests resulted in <0.05 kg of residual powder left in the

container (an average of 0.50 and 0.47% of the initial mass, respectively). This minor difference is likely a product of lesser agent mass loaded into the HRD initially; the residual mass in the container in all cases is deemed insignificant, and injection is considered to be full and complete.

Photographs of rupture disc opening were taken for all tests as part of post-test documentation. Discharge of all agent types resulted in complete, non-fragmenting rupture disc opening. An illustration of standard rupture disc opening is provided in Figure 4.7 (Test No. 1-R1; SBC).

Throw distance across the major diameter of the 1 m³ combustion sphere (to be utilized for suppression testing) is approximately 1.24 meters. Upon review of Figure 4.6, all three agents display nearly equivalent bulk average inverse velocities at throw distances less than 2.74 meters, signifying a uniform time-to-cover over this target throw range. In addition to the qualitative plume geometry observations and the deductions rationalized from container pressure transducer measurements, these outcomes encourage the dependability of upcoming 1 m³ sphere suppression test results.

Open-air dispersion testing at particular agent fill weights sets restrictions on the structure of the suppression test plan. Discharge performance and agent injection capability have not been validated for container fill weights larger than that which have been tested. Demonstrating the lowest crystal density of all agents tested, dispersion of MAP at a 4.08 kg fill weight acts as the limiting factor in this regard. During suppression testing, agent concentrations must remain equivalent for proper comparison of inhibition efficiency. All 10 L HRD containers are to be filled with no greater poundage of suppressant agent than was tested in this open-air study.

4.2.2. 1 m^3 Sphere Explosibility and Suppression

Explosibility testing in the 1 m^3 combustion sphere, as described in Section 4.1.2, was performed for both iron and aluminum powder fuels prior to suppression testing. K_{St} and P_{max}

results, as well as tested fuel concentration and ignition delay, are documented in Table 4.2. Higher concentrations of fuel were preferable, offering a superior representation of the metal dust flame reactivity. Ignition delay was adjusted accordingly over multiple tests in order to confirm that injection and combustion of fuel were complete. Even at high concentration of suspended iron, inspection of dispersion vessels following tests at a 500 ms ignition delay indicated no excess fuel following the event and resulted in no combustion back-pressure through the ball valve. Inspection of the $1m^3$ sphere after each explosibility test at this time delay also exhibited complete combustion of all fuel while in suspension, with no smoldering nests or unburnt fuel on the walls or bottom of the vessel. While this time delay is slightly shorter than that used for standard explosibility testing of typical industrial fuels in this particular vessel (600 ms, calibrated to ASTM standard methods), it was deemed necessary to ensure complete combustion as metal dust fuels inject significantly faster than lower density organics that are commonly used for vessel calibration.

Fuel concentration must also be tuned to ensure that the fuel severity was appropriately demanding of the agents. If the fuel is too aggressive, the agents would be overwhelmed, and the deflagration would be unsuppressed. If not challenging enough, it may be difficult to assess deviations in inhibitor performance during suppression testing. At 2,250 g/m^3 fuel concentration, iron explosibility testing yielded an average K_{St} and P_{max} of 61 barg-m/s and 4.52 barg, respectively, while aluminum explosibility testing at only 500 g/m^3 yielded an average K_{St} and P_{max} of 170 barg-m/s and 8.12 barg, respectively. Such an increase in severity at significantly lower fuel concentration reflects the spontaneity and intensity commonly associated with aluminum powder combustion.

Suppression testing in the 1 m^3 combustion sphere was performed on both iron and aluminum deflagrations with the three agents under analysis (SBC, Met-L-X, and MAP). Test conditions and

results from this study are documented for iron and aluminum suppression within Table 4.3 and Table 4.4, respectively. All iron deflagration suppression testing was executed at a 70 mbarg set pressure, and atmospheric pressure as the target ignition pressure, to allow for moderate deflagration development prior to suppression. Based on agent load constraints from open-air dispersion testing, a constant applied suppressant concentration of 4.08 kg/m^3 required a single 10 L HRD to be utilized for all experiments.

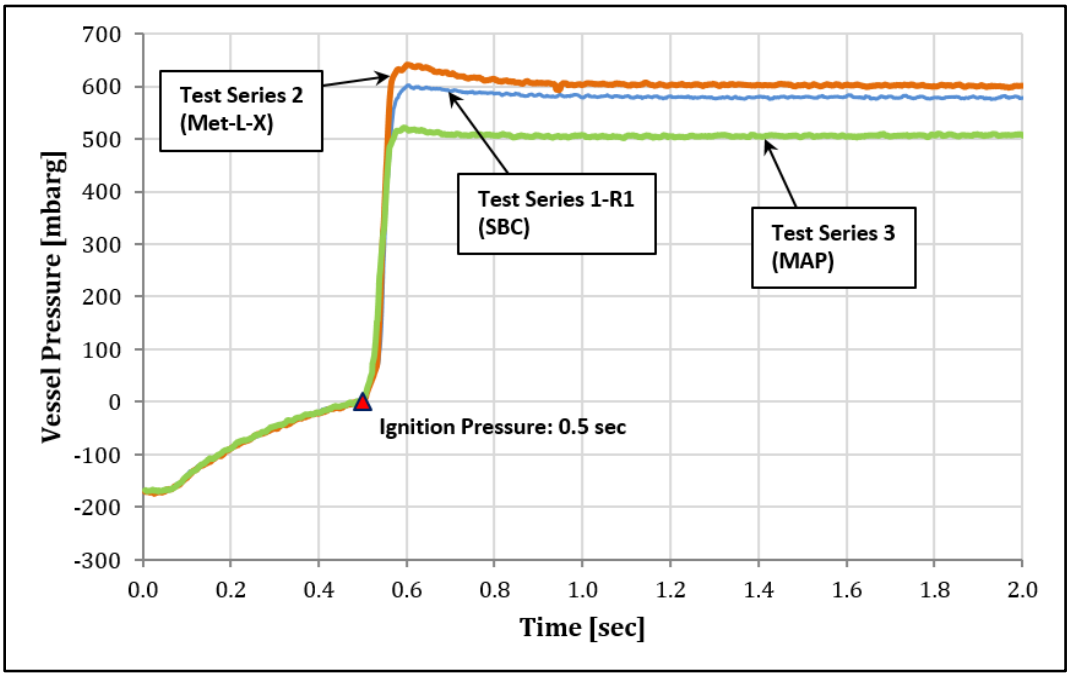

Figure 4.8. Vessel pressure versus time curves for select active suppression experiments with iron powder.

Following suppression of iron combustion via injection of SBC and Met-L-X, analysis of vessel pressure versus time curves (Figure 4.8) yielded effective average TSPs of 0.60 barg and 0.62 barg, respectively. Suppression with MAP at the same concentration of agent yielded an average effective TSP of 0.51 barg. This reduction can be attributed to chemical inhibition, exploited as a supplement to standard physical inhibition. As discussed in Section 3.4.3, thermal analysis of iron and iron/inhibitor mixture samples indicated promising mitigation performance for MAP (which demonstrated nearly 95% reduction in heat released during iron powder

combustion) due to amplified degree of overlap between fuel oxidation and primary agent decomposition temperature ranges. Principal decomposition of SBC and Met-L-X occurs either before or after the solid-phase iron powder oxidation range, indicating that these two suppressant agents exhibit roughly the same physical inerting potential and do not function effectively through chemical means for this specific fuel composition.

All aluminum powder deflagration suppression testing was executed at a relatively lower set pressure of 35 mbarg and an agent concentration of 8.16 kg/m^3. Atmospheric pressure was targeted as the initial ignition pressure. Compared to applications conveying organic dusts or normally reactive metals, aluminum processing requires protection solutions designed at significantly lower detection thresholds. In the case of ignition of an extremely reactive metal, prompt system activation at low set pressure allows for introduction of suppressant before the deflagration is able to develop energy.

Figure 4.9. Test setup for 1 m^3 suppression testing with two 10 L HRD containers.

Although suppression with SBC required a single 10 L HRD container, suppression with Met-L-X and MAP, both with decreased particulate density relative to SBC, required simultaneous activation of two 10 L HRD containers to maintain a constant suppressant concentration, to retain adequate nitrogen headspace for accelerating the suppression agents during discharge, and to preserve the same timescale for discharge as with SBC (T90). The 1 m^3 combustion chamber setup, equipped with two 10 L HRD containers, is depicted in Figure 4.9. Both HRDs were mounted on the same hemispherical section of the combustion sphere, so as to not introduce agent throw distance as a potential variable influencing inhibition performance.

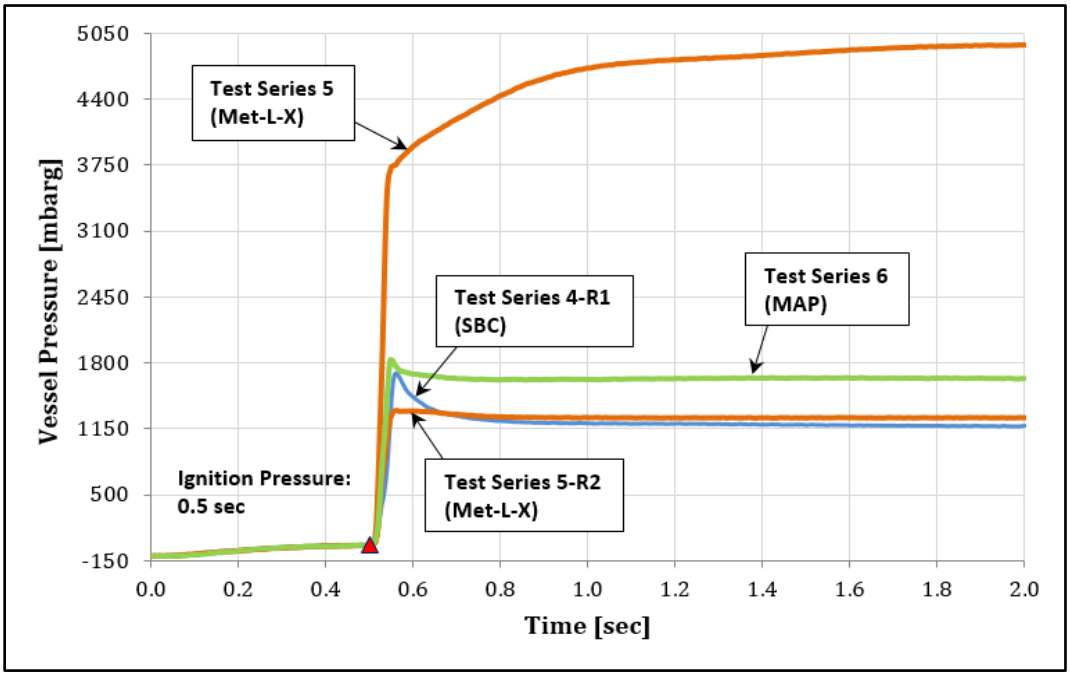

Figure 4.10. Vessel pressure versus time curves for select active suppression experiments with aluminum powder.

Following suppression of aluminum combustion via injection of SBC and MAP, the analysis of vessel pressure versus time curves (see Figure 4.10) yielded effective average TSPs of 1.61 barg and 1.63 barg, respectively. Although complete thermal analytical predictive techniques were not available for aluminum powder (see Section 3.4.4), Met-L-X was anticipated to chemically inhibit aluminum combustion due to its high-temperature agent decomposition. However, aluminum

deflagration suppression with Met-L-X seemed to demonstrate inconsistent outcomes, with TSPs ranging from 1.33 barg (Test Series 5-R2) to 4.95 barg (Test Series 5).

Figure 4.11. Residual combustion deposit following active suppression of aluminum powder deflagration with Met-L-X suppressant agent; Test Series 5.

The post-test combustion residue associated with Test Series 5 is shown in Figure 4.11. As described in Section 3.1.3, Met-L-X is primarily composed of sodium chloride and thermoplastic polymer additive used to form a protective layer preventing further diffusion of oxygen to the burning metal surface. Upon inspection of the burnt mixture internal to the combustion chamber, a dark coating was visible atop a partially oxidized fuel and agent mixture. While effective for fire suppression application, the polymer coating appeared to induce a confined smoldering nest when employed for explosion suppression. Continued partial combustion of unsuspended fuel allowed for steady build of pressure until the end of data collection approximately 1500 ms after the initial ignition of fuel. As long as bulk flow properties are not compromised, removal of the thermoplastic polymer additive from Met-L-X would potentially add performance stability during application as

an explosion suppressant. During high-temperature aluminum flame propagation, agent decomposition volatiles likely dissociate and are less inclined to participate chemically in the combustion reaction inhibition. Reliance on physical inhibition and dilution mechanisms, through increased concentrations of suppressant, is vital for the effective suppression of deflagrations which display increasingly substantial burning temperature and reactivity.

Table 4.2. Iron and aluminum powder fuel particle size statistical analysis and fuel explosibility results via 1 m³ sphere testing, presented as the average of two identical tests.

Fuel Type	Particle Size Distribution			1 m³ Explosibility Testing			
	< 5 um	< 40 um	Mean Size	Fuel Concentration [g/m³]	Ignition Delay [ms]	K_{St} [barg-m/s]	P_{max} [barg]
Al-100	79%	100%	3.51	500	500	170	8.12
Fe-101	11%	76%	26.97	2250	500	61	4.52

Table 4.3. 1 m³ sphere suppression test results for iron powder fuel (Fe-101), with variable suppressant composition.

Test Series	Fuel Type	Fuel Concentration [g/m³]	Ignition Delay [ms]	Suppressant Type	Suppressant Concentration [kg/m³]	P_{set} [mbarg]	P_{ign} [mbarg]	TSP [barg]
1	Fe-101	2250	500	SBC	4.08 [10L HRD container x1]	70	1.5	0.59
1-R1	Fe-101	2250	500	SBC	4.08 [10L HRD container x1]	70	0.7	0.60
2	Fe-101	2250	500	Met-L-X	4.08 [10L HRD container x1]	70	0.2	0.64
2-R1	Fe-101	2250	500	Met-L-X	4.08 [10L HRD container x1]	70	5.6	0.60
3	Fe-101	2250	500	MAP	4.08 [10L HRD container x1]	70	-0.4	0.52
3-R1	Fe-101	2250	500	MAP	4.08 [10L HRD container x1]	70	1.6	0.50

Table 4.4. 1 m³ sphere suppression test results for aluminum powder fuel (Al-100), with variable suppressant composition.

Test Series	Fuel Type	Fuel Concentration [g/m³]	Ignition Delay [ms]	Suppressant Type	Suppressant Concentration [kg/m³]	P_{set} [mbarg]	P_{ign} [mbarg]	TSP [barg]
4	Al-100	500	500	SBC	8.16 [10L HRD container x1]	35	11.3	1.54
4-R1	Al-100	500	500	SBC	8.16 [10L HRD container x1]	35	7.4	1.68
5	Al-100	500	500	Met-L-X	8.16 [10L HRD container x2]	35	3.0	4.95
5-R1	Al-100	500	500	Met-L-X	8.16 [10L HRD container x2]	35	-5.3	1.85
5-R2	Al-100	500	500	Met-L-X	8.16 [10L HRD container x2]	35	0.4	1.33
5-R3	Al-100	500	500	Met-L-X	8.16 [10L HRD container x2]	35	-2.0	1.98
6	Al-100	500	500	MAP	8.16 [10L HRD container x2]	35	2.9	1.83
6-R1	Al-100	500	500	MAP	8.16 [10L HRD container x2]	35	-8.2	1.42

Chapter 5: Conclusion

Dust explosions induced by the ignition of reactive metal powders continue to present a substantial hazard within metal handling and refining industries. High-rate injection of an inert agent material as the flame front begins to develop (i.e., active suppression) allows for deflagration extinction and effective mitigation of pressure growth within the protected enclosure volume. Inhibition of combustion propagation generally occurs via three routes: physical inhibition, chemical inhibition, and dilution of the preheat zone. However, due to characteristically intense severity and spontaneous burning mechanisms, mitigation of metal powder deflagrations at moderate total suppressed pressures (relative to the overall design strength of the vessel) and at low agent concentrations remains challenging. As demonstrated through TGA/DSC analysis of fuel and fuel/agent mixtures, specific suppressant agent compositions appear to exhibit heightened inhibition performance as a result of the greater overlap between agent decomposition and fuel oxidation temperature ranges. Such overlap prompts increased chemical inhibition effectiveness, which acts as a direct supplement toward standard physical inhibition mechanisms. This study reviews recent metal dust suppression testing in Fike Corporation's 1 m^3 sphere combustion chamber and evaluates the efficacy of multiple suppressant agents (sodium bicarbonate [SBC], sodium chloride [Met-L-X], and monoammonium phosphate [MAP]) for the mitigation of iron and aluminum powder deflagrations at suspended fuel concentrations of 2,250 g/m^3 and 500 g/m^3, respectively.

As predicted from thermal analytical studies, iron deflagration suppression experiments at a 70 mbarg set pressure and with MAP as the discharged suppressant agent yielded marginally lower reduced pressures (average TSP of 0.51 barg) relative to experiments with SBC (average TSP of 0.60 barg). According to the TGA profile for MAP, primary decomposition of the agent occurs

directly atop the solid-phase combustion temperature range of iron powder. Compared to SBC and Met-L-X, whose decomposition temperatures exist either above or below the iron combustion temperature window, MAP offers deflagration mitigation by both physical and chemical means, absorbing heat released via fuel oxidation and consuming free radicals which would otherwise prolong the combustion duration. Increased chemical inhibition effectiveness upon use of MAP thus justifies the apparent reduction in TSP. If adopted commercially, it is recommended to modify the composition of the suppressant mixture (increased content of flow-promoting silica) in order to stimulate enhanced dispersion of agent at higher target throw distances more representative of industrial application.

Aluminum deflagration suppression experiments at a 35 mbarg set pressure yielded TSPs greater than 1 barg for all agents tested. Relative to iron powder combustion (normally reactive), aluminum is considered a highly reactive metal and proved more difficult to suppress. Although Met-L-X was anticipated to demonstrate improved inhibition of aluminum combustion due to its high-temperature principal decomposition, suppression testing produced inconsistent results. Suppression of aluminum deflagration with Met-L-X yielded TSP as low as 1.33 barg and as high as 4.95 barg. Inspection of combustion chamber internals following Test Series 5 (Met-L-X, TSP = 4.95 barg) revealed a thin layer of material coating the top of a partially oxidized fuel/agent mixture. In this particular case, it is likely that the thermoplastic polymer additive within Met-L-X created ideal circumstances for a smoldering nest, which continued to burn and gradually generate pressure. As confirmed by the vessel pressure versus time profile for this test, the maximum suppressed pressure did not occur until several seconds after initiation of the event.

Chemical inhibition as a supplement to physical inhibition appeared to be less effective for the suppression of metal fuels with increasing reactivity. The influence of chemical inhibition on iron

powder deflagration extinction was evident but marginal. Fuels such as aluminum display exceedingly high burning temperatures, which may lead to dissociation of agent decomposition volatiles that would normally impede combustion chemically or participate in dilution of the preheat zone. Greater metal fuel reactivity requires over-reliance on physical inhibition mechanisms. From a suppression system design standpoint, this translates to saturation of the combustion volume with inert material at agent concentrations well beyond the standard requirements of an organic dust. For suppression applications requiring high agent concentrations, the use of multiple smaller HRDs rather than a larger one is an effective design approach providing improved agent delivery rate and optimized agent throw distances. Maintaining appropriate response time through low pressure activation set points allows the protection system an opportunity to extinguish the flame front before propagation accelerates to uncontrollable proportions. Combination venting with active suppression is also recommended for extremely reactive hazards in order to keep reduced pressures sufficiently below the enclosure design strength. Appropriate characterization of the hazard and conservative system design procedures are essential for proper protection of industrial processes conveying combustible metal dusts.

Nomenclature

K_{St} [=] Fuel Explosibility Index; Proportional to Maximum Rate of Pressure Rise

P_{max} [=] Maximum Pressure Observed upon Fuel Ignition in a Contained Enclosure

Maximum Adiabatic Flame Temperature [=] MAFT

MIE [=] Minimum Ignition Energy

MIT [=] Minimum Ignition Temperature

MEC [=] Minimum Explosible Concentration

LOC [=] Limiting Oxygen Content

DDT [=] Deflagration to Detonation Transition

SBC [=] Sodium Bicarbonate

MAP [=] Monoammonium Phosphate

PK [=] Potassium Bicarbonate

DAP [=] Diammonium Phosphate

STA [=] Simultaneous Thermal Analysis

TGA [=] Thermogravimetric Analysis

DSC [=] Differential Scanning Calorimetry

CFD [=] Computational Fluid Dynamics

DEM [=] Discrete Element Method

PSA [=] Particle Size Analysis

HRD [=] High-Rate Discharge Container

GCA [=] Gas Cartridge Actuator

TSP [=] Total Suppressed Pressure

Acknowledgements

This study represents a collaborative effort between Fike Corporation and the University of Kansas. The authors acknowledge the assistances of NETZSCH (Mike Hsu; Melinda Tucker) and the University of Kansas in providing simultaneous thermal analysis (STA) for all fuel and agent samples. This project recognizes the efforts of Rachel Speckin, Edward Reyes, and David Treviño for their experimental contributions, as well as the efforts of Dr. David Minnick for his invaluable assistance with TGA/DSC instrument training, calibration, and troubleshooting. Gilbert Ortiz is also recognized for his work on the design and creation of two graphics utilized by Industrial & Engineering Chemistry Research as journal cover art positions. Additionally, the author acknowledges the vital contributions of Fike Corporation's remote site testing facility staff and combustion test lab technicians in conducting open-air dispersion testing, fuel explosibility analysis, and 1 m^3 sphere active suppression experiments. The author recognizes the support of Fike Corporation in providing operational resources, continued funding of the test program, and consent to publish the results of this work.

References

(1) U.S. Chemical Safety and Hazard Investigation Board. *Combustible Dust Hazard Study*, 2006.

(2) U.S. Chemical Safety and Hazard Investigation Board. *Investigation Report No. 2004-01-I-IN*; Hayes Lemmerz International, Inc., Huntington, IN, 2003.

(3) U.S. Chemical Safety and Hazard Investigation Board. *Case Study No. 2011-3-I-WV*; AL Solutions, Inc., New Cumberland, WV, 2010.

(4) U. S. Chemical Safety and Hazard Investigation Board. *Case Study No. 2011-4-I-TN*; Hoeganaes Corporation, Gallatin, TN, 2011.

(5) Li, G.; Yang, H.-X.; Yuan, C.-M.; Eckhoff, R. K. A catastrophic aluminum-alloy dust explosion in China. *J. Loss Prev. Process Ind.* **2016**, *39*, 121-130.

(6) Eckhoff, R. K. *Dust Explosions in the Process Industries*, 3rd ed.; Gulf Professional Publishing: Amsterdam, 2003.

(7) Gao, W.; Mogi, T.; Yu, J.; Yan, X.; Sun, J.; Dobashi, R. Flame propagation mechanisms in dust explosions. *J. Loss Prev. Process Ind.* **2015**, *39*36 186-194.

(8) Reding, N.; Shiflett, M. B. Metal Dust Explosion Hazards: A Technical Review. *Ind. Eng. Chem. Res.* **2018**. *57* (34), 11473-11482.

(9) Taveau, J. Combustible Metal Dusts: A Particular Class. In *17th Annual International Symposium, Mary Kay O'Connor Process Safety Center*, College Station, TX, Oct 28-30, 2014; 594-606.

(10) Ogle, R. A. *Dust Explosion Dynamics*; Elsevier: Warrenville, IL, 2017.

(11) National Fire Protection Association. *NFPA 654: Standard for the Prevention of Fire and Dust Explosions from the Manufacturing, Processing, and Handling of Combustible Particulate Solids*, 2013.

(12) National Fire Protection Association. *NFPA 484: Standard for Combustible Metals*, 2015.

(13) Schwenzfeuer, K.; Glor, M; Gitza, A. Relation between Ignition Energy and Limiting Oxygen Concentration for Powders. In *Proceedings from the 10th International Symposium on Loss Prevention and Safety Promotion in the Process Industry*, Stockholm, Sweden, June 2001; Elsevier: Amsterdam, Netherlands, 2001; 909-916.

(14) Ballal, D. R. Ignition and flame quenching of quiescent dust clouds of solid fuels. *The Royal Society Publishing*. **1980**, *369* (1739).

(15) Myers, T. J. Reducing aluminum dust explosion hazards: Case study of dust inerting in an aluminum buffing operation. *J. of Hazard. Mater.* **2008**, *159*, 72-80.

(16) Miao, N.; Zhong, S.; Yu, Q. Ignition characteristics of metal dusts generated during machining operations in the presence of calcium carbonate. *J. Loss Prev. Process Ind.* **2016**, *40*, 174-179.

(17) Baudry, G.; Bernard, P.; Gillard, P. Influence of the oxide content on the ignition energies of aluminum powders. *J. Loss Prev. Process Ind.* **2007**, *20*, 330-336.

(18) Yuan, C.; Amyotte, P. R.; Hossain, M. N.; Li, C. Minimum ignition temperature of nano and micro Ti powder clouds in the presence of inert TiO_2 powder. *J. of Hazard. Mater*. **2014**, *275*, 1-9.

(19) Bernard, S.; Gillard, P.; Foucher, F.; Mounaïm-Rousselle, C. MIE and flame velocity of partially oxidised aluminum dust. *J. Loss Prev. Process Ind*. **2012**, *25*, 460-465.

(20) Gao, W.; Zhou, Q.; Sun, J. Flame propagation through zirconium particles coated with different ratios of Fe_3O_4. *Fuel* **2015**, *148*, 231-237.

(21) Chatrathi, K.; Going, J. Dust Deflagration Extinction. *Process Saf. Prog.* **2000**, *19* (3), 146-153.

(22) Dastidar, A. G.; Amyotte, P. R.; Pegg, M. J. Factors influencing the suppression of coal dust explosions. *Fuel* **1997**, *76* (7), 663-670.

(23) Amyotte, P. R. Solid inertants and their use in dust explosion prevention and mitigation. *J. Loss Prev. Process Ind*. **2006**, *19*, 161-173.

(24) Sun, J.; Dobashi, R.; Hirano, T. Structure of flames propagating through aluminum particles cloud and combustion process of particles. *J. Loss Prev. Process Ind.* **2006**, *19*, 769-773.

(25) Puri, P. Multiscale modelling of ignition and combustion of micro and nano aluminum particles. Ph.D. Dissertation; Pennsylvania State University, 2008.

(26) Gao, W.; Zhang, X.; Zhang, D.; Peng, Q.; Zhang, Q.; Dobashi, R. Flame propagation behaviours in nano-metal dust explosions. *Powder Technol*. **2017**, *321*, 154-162.

(27) Dreizin, E.; Hoffman, V. Constant Pressure Combustion of Aerosol of Coarse Magnesium Particles in Microgravity. *Combustion and Flame* **1999**, *118*, 262-280.

(28) Broumand, M.; Bidabadi, M. Modeling combustion of micron-sized iron dust particles during flame propagation in a vertical duct. *Fire Safety Journal* **2013**, *59*, 88-93.

(29) Going, J.; Snoeys, J. Explosion Protection with Metal Dust Fuels. *Process Saf. Prog.* **2002**, *21* (4).

(30) National Fire Protection Association. *NFPA 69: Standard on Explosion Prevention Systems*, 2014.

(31) Zhang, Q.; Liu, L.; Shen, S. Effect of turbulence on explosion of aluminum dust at various concentrations of air. *Powder Technol*. **2018**, *325*, 467-475.

(32) Christill, M.; Nastoll, W.; Leuckel, W. Der Einfluss von Strömungsturblenz auf den Explosionsablauf in Staub/Luft-Gemischen. *VDI-Beriche* **1989**, *701*, 123-141.

(33) Eckhoff, R. K.; Parker, S. J.; Gruvin, B. Ignitability and Explosibility of Silicon Dust Clouds. *J. of the Eletrochem. Soc.* **1986**, *133*, 2631-2637.

(34) Jacobson, M.; Cooper, A. R.; Nagy, J. Explosibility of Metal Powders. Report Inv. 6516. U.S. Bureau of Mines: Washington, D.C., 1964.

(35) Kadir, N.; Rusli, R.; Buang, A.; Rahim, N. 4th International Conference on Process Engineering and Advanced Materials: Investigation of the Explosion Behaviour Affected by the Changes in Particle Size. *Procedia Eng*. **2016**, *148*, 1156-1161.

(36) Boilard, S.; Amyotte, P.; Khan, F.; Dastidar, A.; Eckhoff, R. Explosibility of micron- and nano-size titanium powders. *J. Loss Prev. Process Ind.* **2013**, *26*, 1646-1654.

(37) Krietsch, A.; Scheid, M.; Schmidt, M.; Krause, U. Explosion behaviour of metallic nano powders. *J. Loss Prev. Process Ind.* **2015**, 36, 237-243.

(38) Beck, H.; Glienke, N.; Mohlman, C. *Combustion and explosion characteristics of dusts*. BIA-Report 13/97. Hauptverband der gewerblichen Berufsgenossenschafter: Sankt Augustin, 1997.

(39) Moore, P. E.; Cooke, P. L. Suppression of Metal Dust Explosions, Report No. 88/49. *British Material Handling Board*; Ascot, Berkshire, UK, 1988.

(40) Castellanos, D.; Carreto-Vazquez, V.; Mashuga, C.; Trottier, R.; Mejia, A.; Mannan, M. The effect of particle size polydispersity on the explosibility characteristics of aluminum dust. *Powder Technol*. **2014**, *254*, 331-337.

(41) Traoré, M.; Dufaud, O.; Perrin, L.; Chazalet, S.; Thomas, D. Dust Explosions: How Should the Influence of Humidity Be Taken Into Account? *Process Saf. And Envi Prot.* **2009**, *87*, 14-20.

(42) Cashdollar, K.; Zlochower, I. Explosion temperatures and pressure of metals and other elemental dust clouds. *J. Loss Prev. Process Ind.* **2007**, *20*, 337-348.

(43) Elsner, T.; Koneke, D.; Weinspach, P. Thermal radiation of gas/solid mixtures. *Chem. Eng. & Technol.* **1988**, *11* (1), 237-243.

(44) Leuschke, G. Beitrage zue Erforschung des Mechanismus der Flammenausbreitung in Staubwolken. *Staub* **1965**, *25*, 180-186.

(45) Christophe, P.; Rim, B. M.; Mohamed, G.; Khashayar, S.; Jérome, F. Thermal radiation in dust flame propagation. *J. Loss Prev. Process Ind.* **2017**, *49*, 896-904.

(46) Moussa, R.; Guessasma, M.; Proust, C.; Saleh, K.; Fortin, J. Thermal radiation contribution to metal dust explosions. *Procedia Eng.* **2015**, *102*, 714-721.

(47) Julien, P.; Vickery, J.; Whiteley, S.;Wright, A.; Goroshin, S.; Bergthorson, J.; Frost, D. Effect of scale on freely propagating flames in aluminum dust clouds. *J. Loss Prev. Process Ind.* **2015**, *36*, 230-236.

(48) Wang, Y.; Xu, K.; Li, L. Inhibition of the reaction between aluminum dust and water based on the HIM. *RSC Adv.* **2017**, *7*, 33327-33334.

(49) Lees, F. *Lees' Loss Prevention in the Process Industries: Hazard Identification, Assessment and Control*, 4th ed.; Elsevier Inc.: Waltham, MA, 2012.

(50) Mason, P.; Uhlig, F.; Vanek, V.; Buttersack, T.; Bauerecker, S.; Jungwirth, P. Coulomb explosion during the early stages of the reaction of alkali metals with water. *Nat. Chem.* **2015**, *7*, 250-254.

(51) Jiang, H.; Bi, M.; Gao, W.; Gan, B.; Zhang, D.; Zhang, Q. Inhibition of aluminum dust explosions by $NaHCO_3$ with different particle size distributions. *J. Hazard. Mater.* **2018**, *344*, 902-912.

(52) Chen, X.; Zhang, H.; Chen, X.; Liu, X.; Niu, Y.; Zhang, Y.; Yuan, B. Effect of dust explosion suppression by sodium bicarbonate with different granulometric distribution. *J. Loss Prev. Process Ind.* **2017**, *49*, 905-911.

(53) Rockwell, S.; Taveau, J. Studying the Effect of Sodium Bicarbonate on Hybrid Flames: Burner vs. 20-L sphere experiments. In *Proceedings of the Twelfth International Symposium on Hazards, Prevention and Mitigation of Industrial Explosions*, Kansas City, MO, USA, Aug 12-17, 2018.

(54) Taveau, J.; Vingerhoets, J.; Snoeys, J.; Going, J.; Farrell, T. Suppression of metal dust deflagrations. *J. Loss Prev. Process Ind.* **2015**, *36*, 244-251.

(55) Taveau, J.; Vingerhoets, J.; Snoeys, J.; Going, J.; Farrell, T. Explosion Protection with Metal Dust Fuels: New Experimental Evidence. In *Proceedings of the Seventh International Seminar on Fire and Explosion Hazards*, Providence, RI, USA, May 5-10, 2013.

(56) Kuang, K.; Chow, W. K.; Ni, X.; Yang, D.; Zeng, W.; Liao, G. Fire suppressing performance of superfine potassium bicarbonate powder. *Fire Mater.* **2011**, *35*, 353-366.

(57) Horacek, H.; Grabner, R. Advantages of flame retardants based on nitrogen compounds. *Polym. Degrad. Stab.* **1996**, *54*, 205-215.

(58) Jiang, H.; Bi, M.; Li, B.; Gao, W. Inhibition of aluminum dust explosion by $NH_4H_2PO_4$ and $NaHCO_3$. In *Proceedings of the Twelfth International Symposium on Hazards, Prevention and Mitigation of Industrial Explosions*, Kansas City, MO, USA, Aug 12-17, 2018.

(59) Luo, X.; Wang, T.; Ren, J.; Deng, J.; Shu, C.; Huang, A.; Cheng, F.; Wen, Z. Effects of ammonia on the explosion and flame propagation characteristics of methane-air mixtures. *J. Loss Prev. Process Ind.* **2017**, *47*, 120-128.

(60) Moore, P. E. Suppressants for the control of industrial explosions. *J. Loss Prev. Process Ind.* **1996**, *9* (1), 119-123.

(61) Amrogowicz, J.; Kordylewski, W. Effectiveness of dust explosion suppression by carbonates and phosphates. *Combust. Flame* **1991**, *85* (3-4), 520-522.

(62) Camino, G.; Costa, L.; Trossarelli, L. Study of the mechanism of intumescence in fire retardant polymers: Part V – Mechanism of formation of gaseous products in the thermal degradation of ammonium polyphosphate. *Polym. Degrad. Stab.* **1985**, *12* (3), 203-211.

(63) Castellanos, D.; Lewandowski, A.; Diaz, A.; Mejia, A.; Carreto, V.; Mashuga, C.; Rangwala, A.; Cheng, Z.; Mannan, M. Influence of Particle Size and Crystalline Level on the Efficiency of Dust Explosion Inhibitors. *Ind. Eng. Chem. Res.* **2014**, *53*, 11527-11537.

(64) Zalosh, R. Metal hydride fires and fire suppression agents. *J. Loss Prev. Process Ind.* **2008**, *21*, 214-221.

(65) Cao, X.; Ren, J.; Zhou, Y.; Wang, Q.; Gao, X.; Bi, M. Suppression of methane/air explosion by ultrafine water mist containing sodium chloride additive. *J. Loss Prev. Process Ind.* **2015**, *285*, 311-318.

(66) Poletaev, N. I.; Khlebnikova, M.Y.; Khanchych, K. Y. Producing and properties of zinc dust flames. *Comb. Sci. Tech.* **2018**, *190* (6), 1096-1109.

(67) *CRC Handbook of Chemistry and Physics*, 86th ed.; Lide, D. R., Ed.; CRC Press: Boca Raton, FL, 2005.

(68) Stephenson, C. C.; Zettlemoyer, A. C. The heat capacity of ammonium dihydrogen phosphate from 15 to 300 K. The anomaly at the Curie temperature. *J. Am. Chem. Soc.* **1994**, *66* (8), 1405-1408.

(69) Reding, N. S.; Shiflett, M. B. Characterization of Thermal Stability and Heat Absorption for Suppressant Agent/Combustible Dust Mixtures via Thermogravimetric Analysis/Differential Scanning Calorimetry. *Ind. Eng. Chem. Res.* **2019**, *58* (11), 4674-4687.

(70) Huang, D. H.; Tran, T. N.; Yang, B. Investigation on the reaction of iron powder mixture as a portable heat source for thermoelectric power generators. *J. Thermal Analy. Calor.* **2014**, *116* (2), 1047-1053.

(71) ASTM E698, Standard Test Method for Arrhenius Kinetic Constants for Thermally Unstable Materials Using Differential Scanning Calorimetry and the Flynn/Wall/Ozawa Method. *The American Society of Mechanic Engineers*, West Conshohocken, PA, 2001.

(72) Eyring, H. The activated complex in chemical reactions. *J. Chem. Phys.* **1935**, *3*, 107-115.

(73) Evans, M. G.; Polanyi, M. Some applications of the transition state method to the calculation of reaction velocities, especially in solutions. *Trans. Faraday Soc.* **1935**, *31*, 875-894.

(74) Beckstead, M. W. A Summary of Aluminum Combustion. In *Internal Aerodynamics in Solid Rocket Propulsion*, Rhode-Saint-Genèse, Belgium, May 27-31, 2002.

(75) Cashdollar, K. L. Overview of dust explosibility characteristics. *J. Loss Prev. Process Ind.* **2000**, *13*, 183-199.

(76) Dastidar, A. G. Influence of Scale on the Inerting of Dust Explosions. Ph.D. Dissertation, Dalhousie University, 2004.

(77) *ASTM E1226, Standard Test Method for Explosibility of Dust Clouds*; The American Society of Mechanic Engineers: West Conshohocken, PA, 2010.

(78) ISO 6184/1 “Explosion Protection System – Part 1: Determination of Explosion Indices of Combustible Dusts in Air”, International Organization for Standardization, Switzerland, 1985.

Appendix

Appendix A: Particle Size Distributions and Statistical Data for All Fuels and Agents

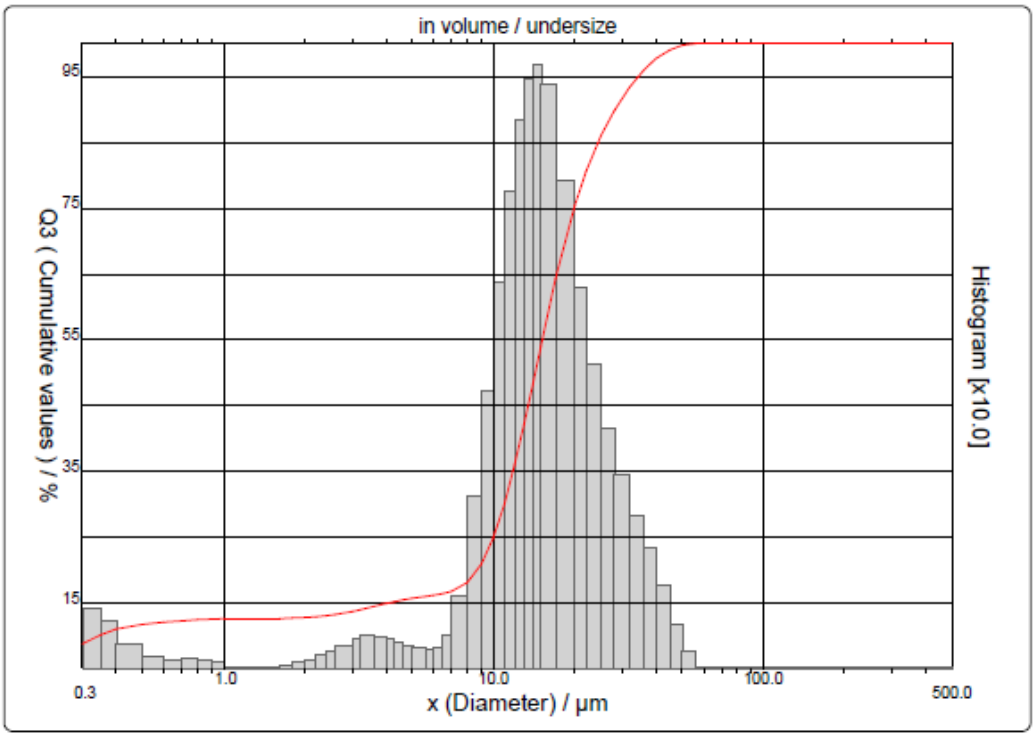

Figure A.1. Particle size distribution for cornstarch [CS].

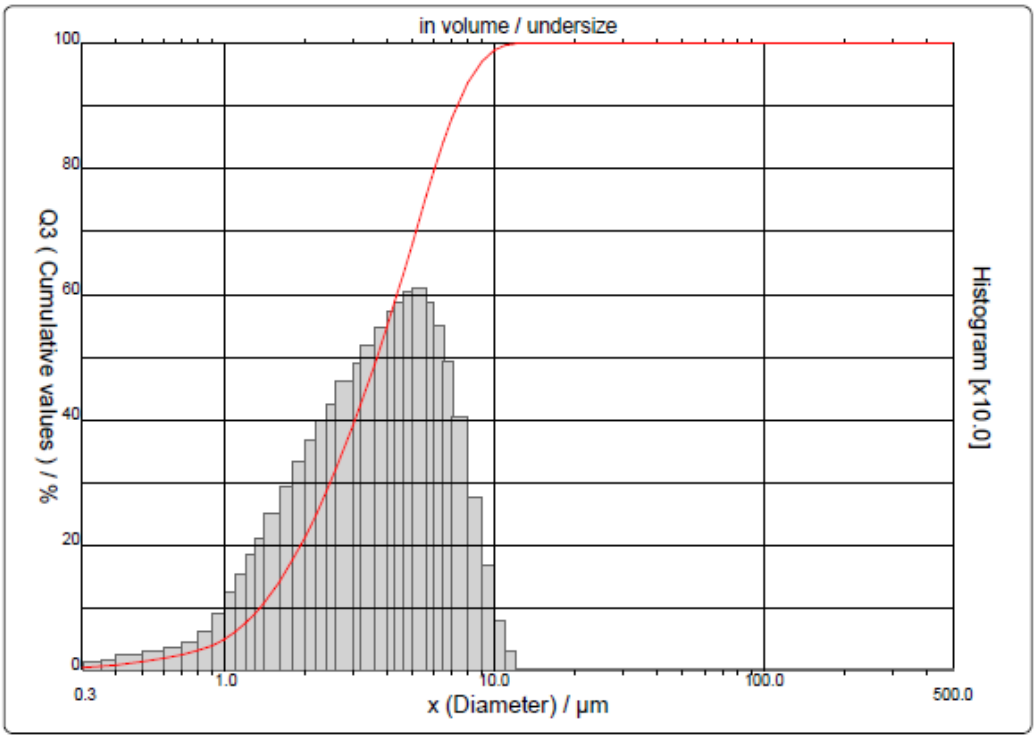

Figure A.2. Particle size distribution for zinc powder [Zn-101].

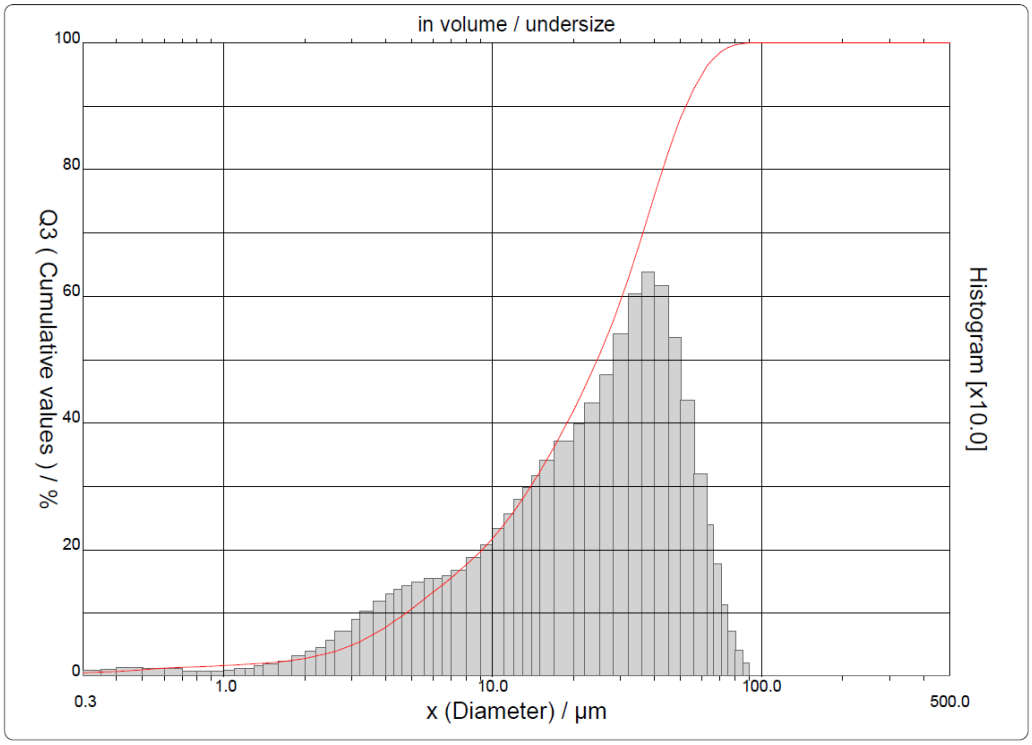

Figure A.3. Particle size distribution for iron powder [Fe-101].

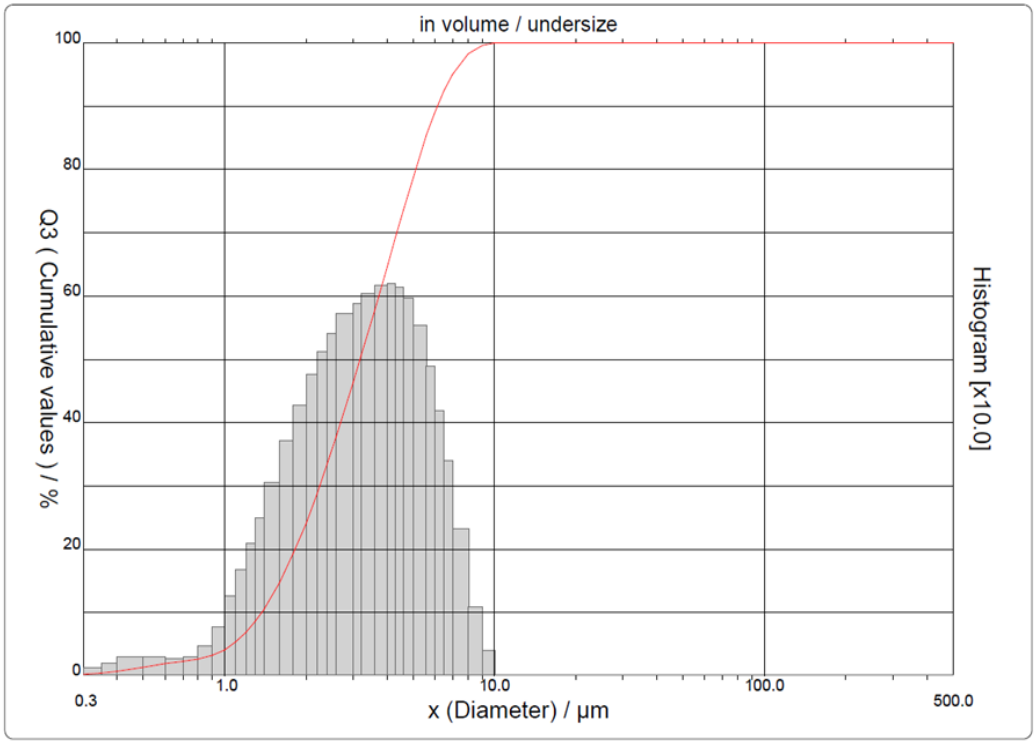

Figure A.4. Particle size distribution for aluminum powder [Al-100].

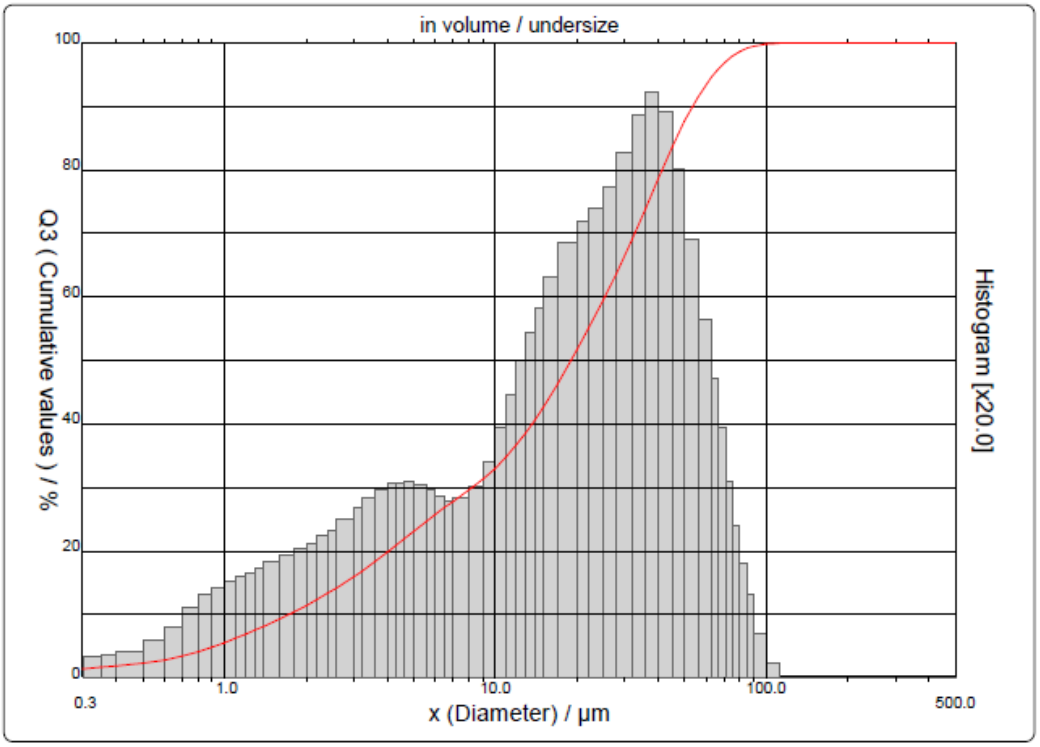

Figure A.5. Particle size distribution for sodium bicarbonate [SBC].

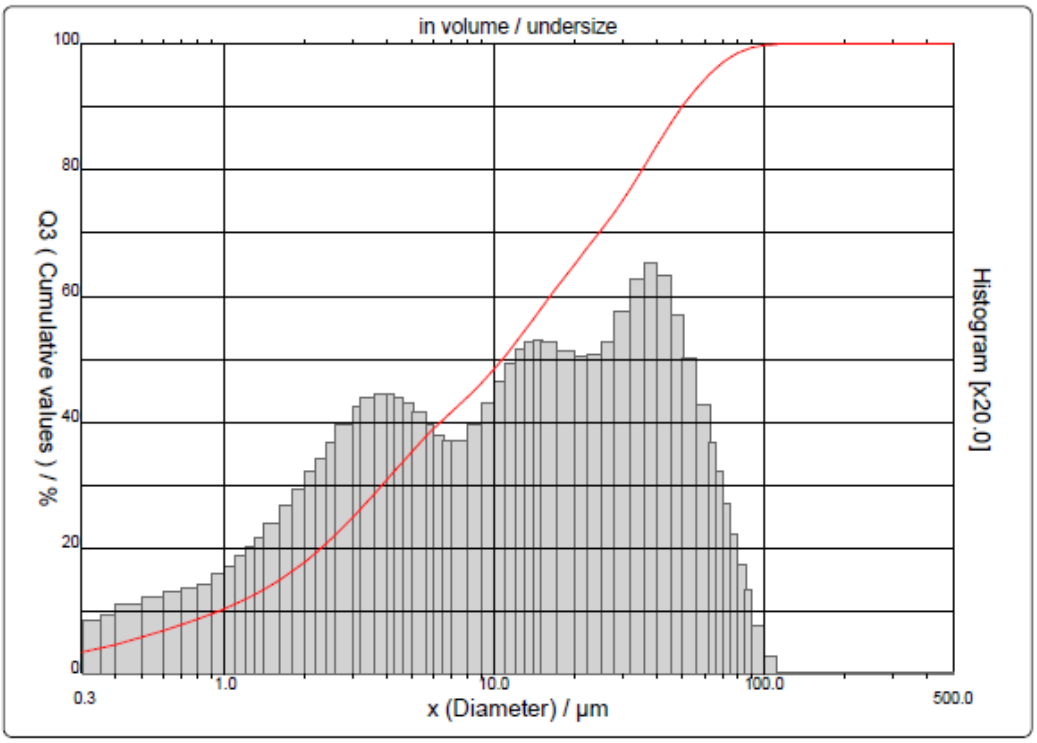

Figure A.6. Particle size distribution for potassium bicarbonate [PK].

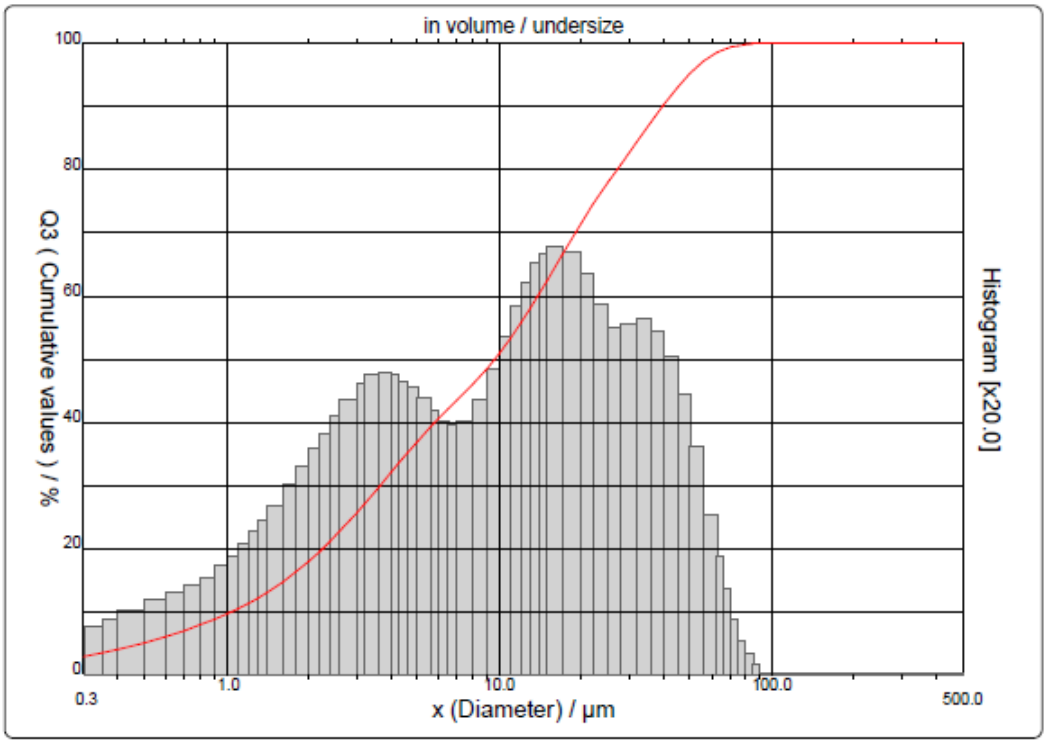

Figure A.7. Particle size distribution for monoammonium phosphate [MAP].

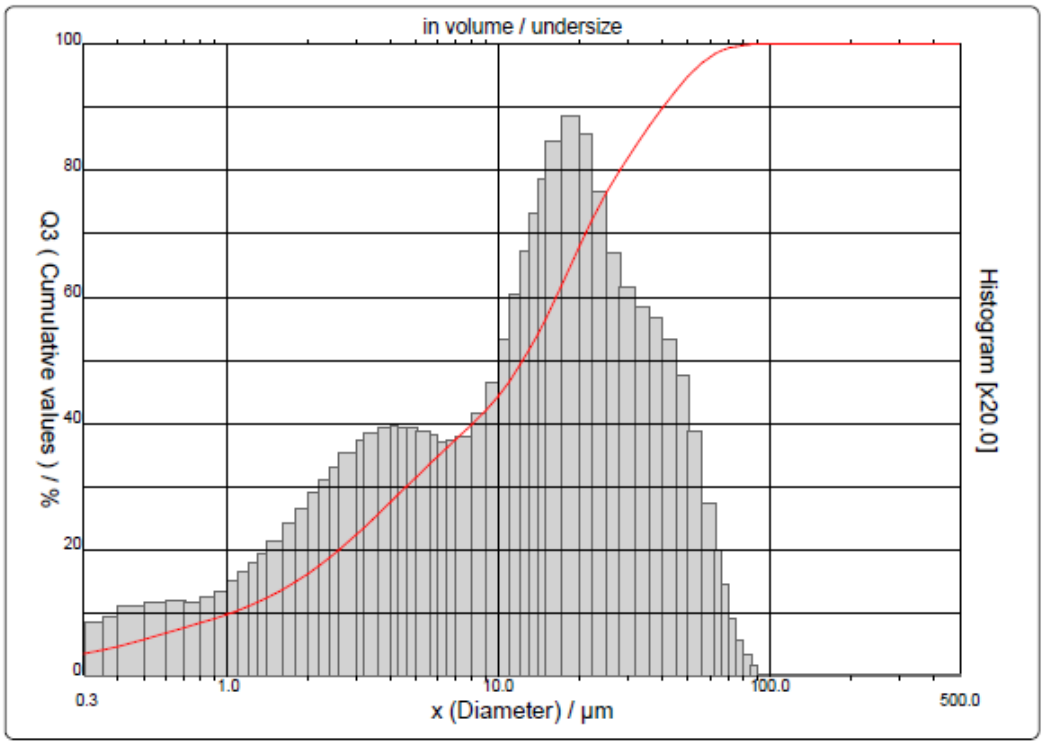

Figure A.8. Particle size distribution for diammonium phosphate [DAP].

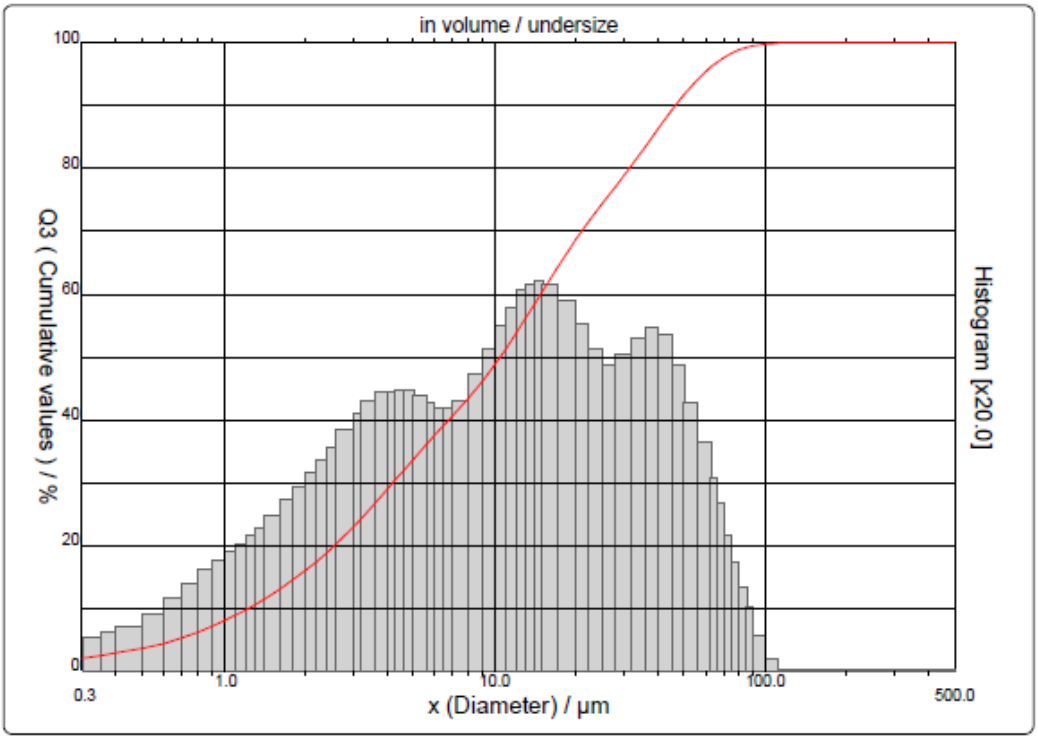

Figure A.9. Particle size distribution for Met-L-X.

Table A.1. Particle size statistical data for all suppressant agent powders.

Suppressant:	SBC	PK	MAP	DAP	Met-L-X
D10 [µm]	1.72	0.96	1.04	1.04	1.23
D50 [µm]	19.03	10.75	9.61	12.34	10.47
D90 [µm]	53.56	49.58	39.55	40.29	46.34
Mean Diameter [µm]	23.75	18.89	15.27	16.54	17.63

Table A.2. Particle size statistical data for all fuel powders.

Fuel:	Cornstarch (CS)	Zinc (Zn-101)	Iron (Fe-101)	Aluminum (Al-100)
D10 [µm]	0.34	1.36	4.76	1.37
D50 [µm]	14.29	3.68	24.49	3.18
D90 [µm]	28.18	7.31	52.30	6.15
Mean Diameter [µm]	15.28	4.04	26.86	3.51

Appendix B: Mass Loss Profiles (TGA) for All Inhibitors and 1:1 Fuel/Inhibitor Mixtures

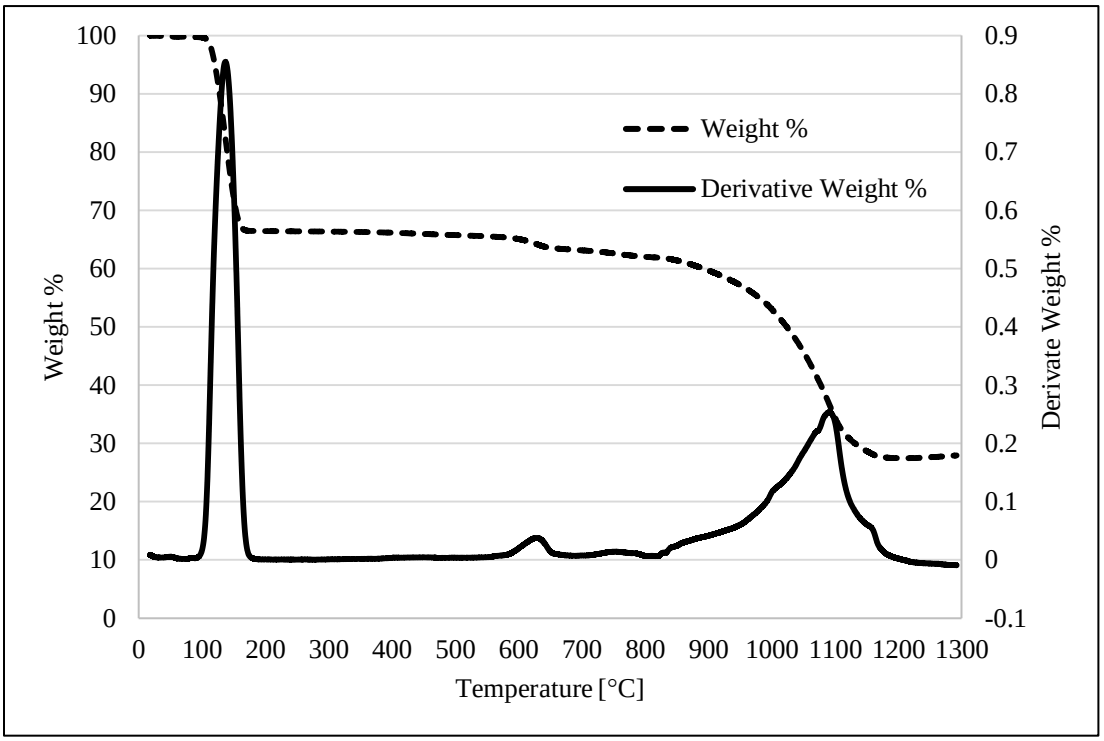

Figure B.1. Thermogravimetric profile of sodium bicarbonate. Increase in temperature, from room temperature to 1300 °C, at a constant 10 °C/min heating rate (in air).

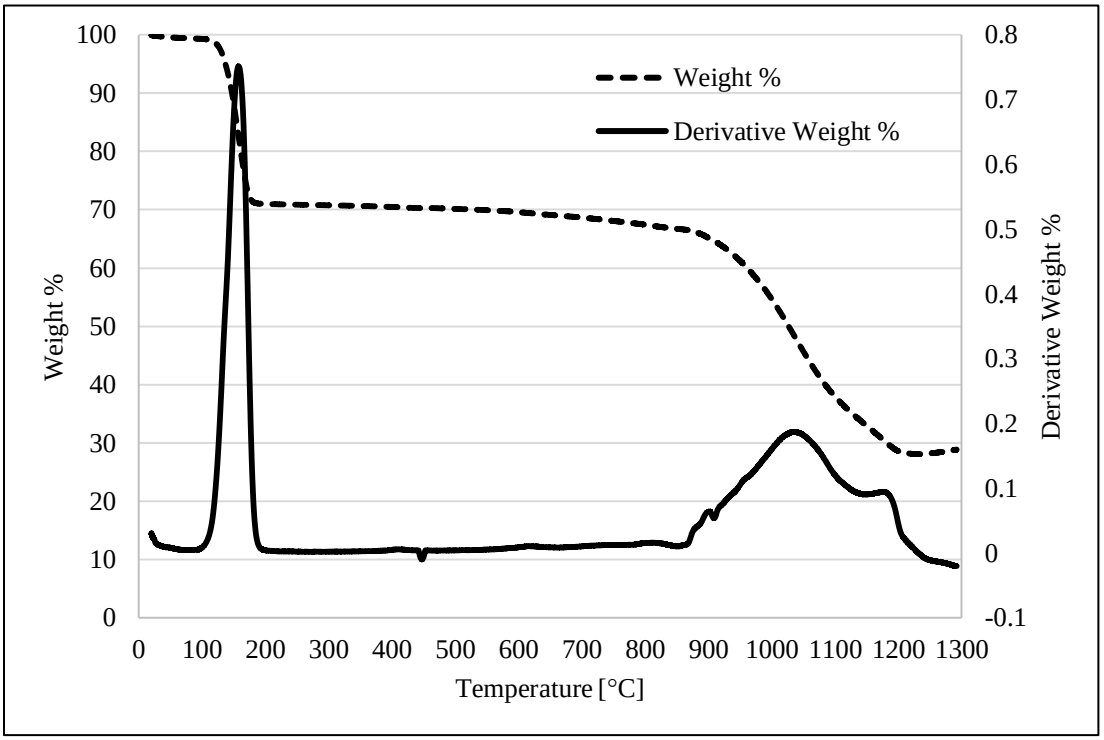

Figure B.2. Thermogravimetric profile of potassium bicarbonate. Increase in temperature, from room temperature to 1300 °C, at a constant 10 °C/min heating rate (in air).

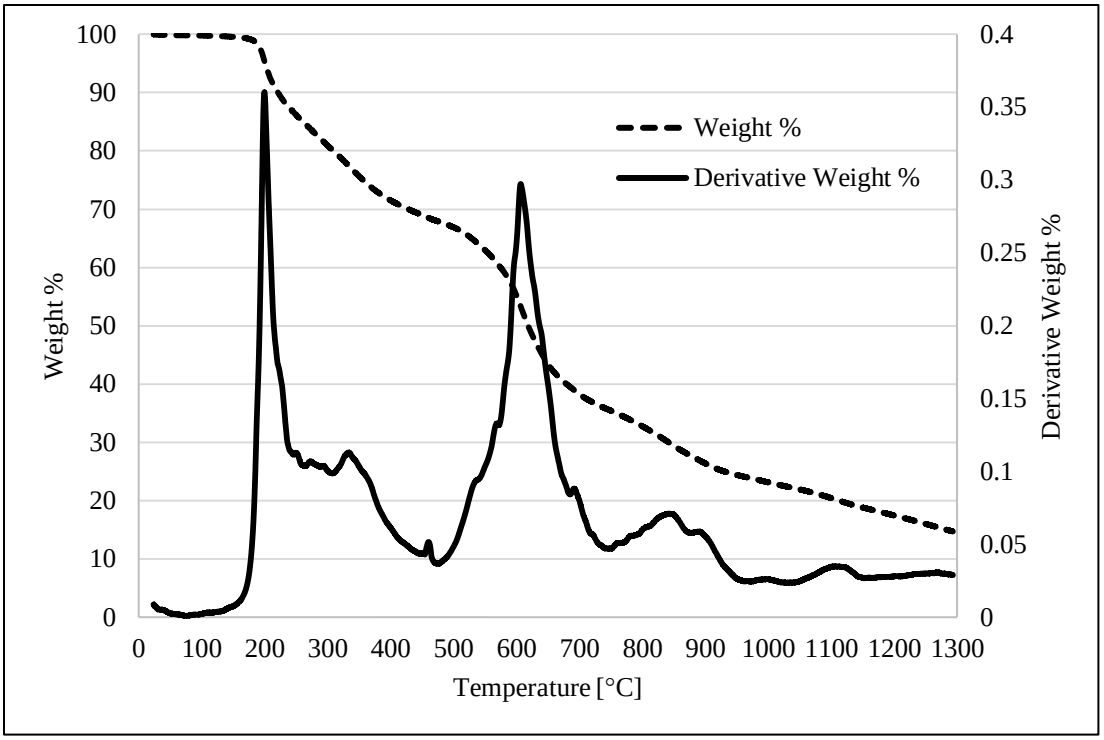

Figure B.3. Thermogravimetric profile of monoammonium phosphate. Increase in temperature, from room temperature to 1300 °C, at a constant 10 °C/min heating rate (in air).

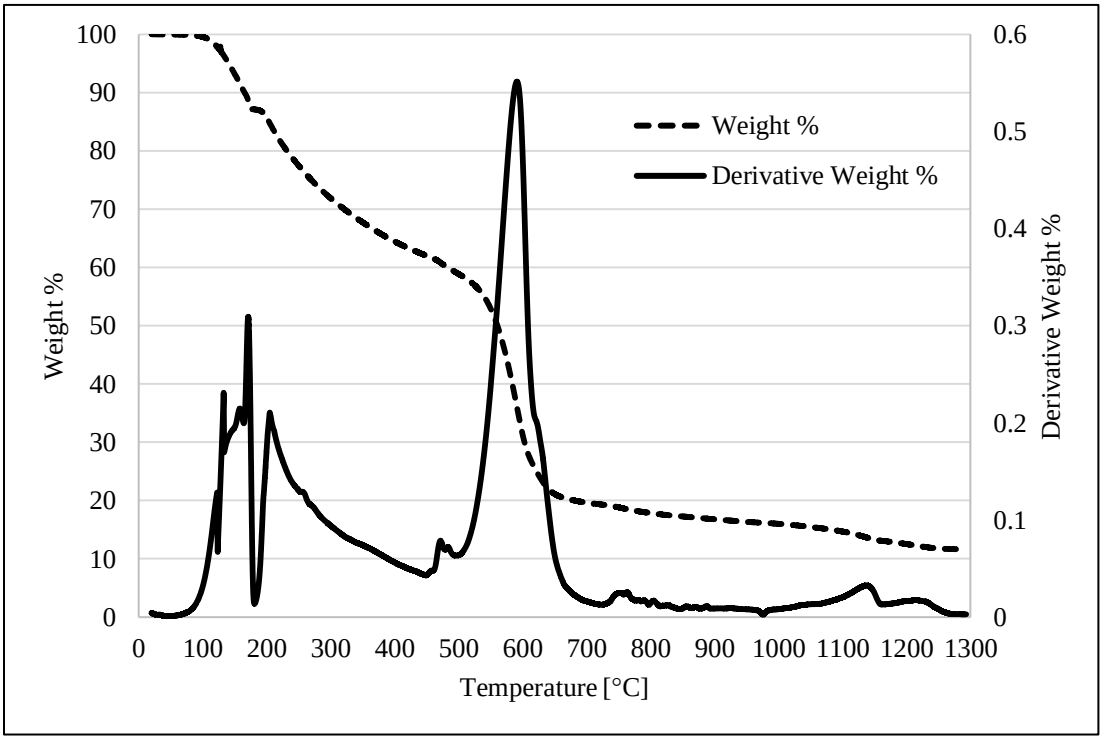

Figure B.4. Thermogravimetric profile of diammonium phosphate. Increase in temperature, from room temperature to 1300 °C, at a constant 10 °C/min heating rate (in air).

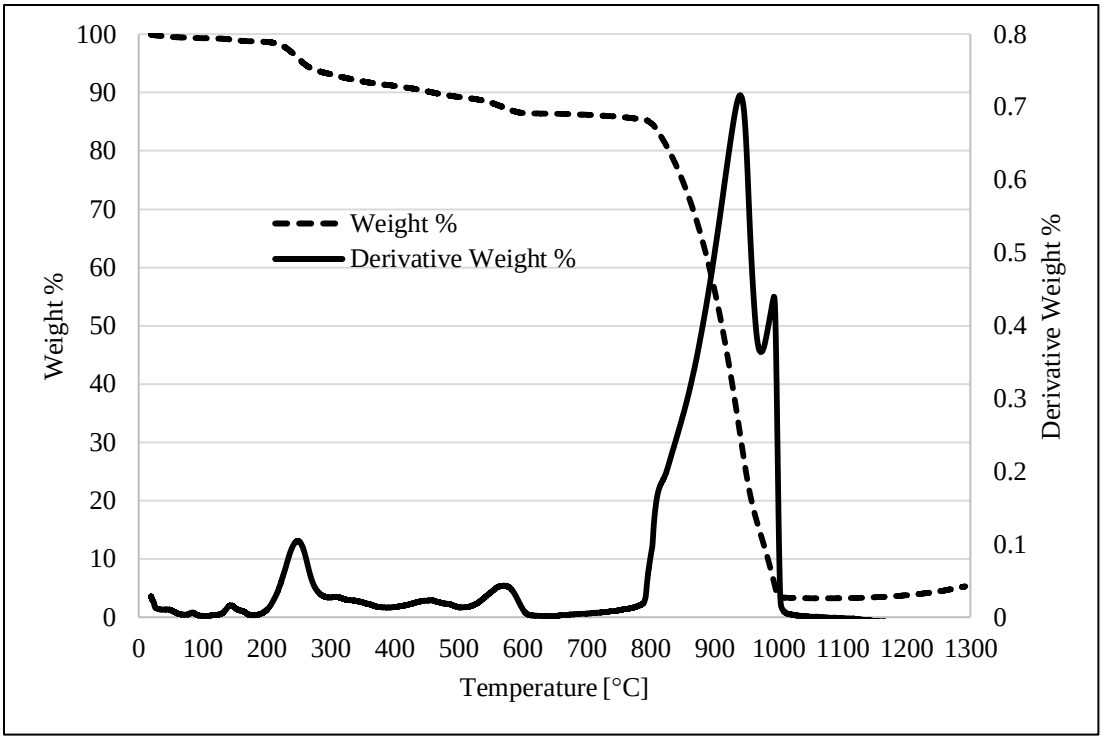

Figure B.5. Thermogravimetric profile of Met-L-X. Increase in temperature, from room temperature to 1300 °C, at a constant 10 °C/min heating rate (in air).

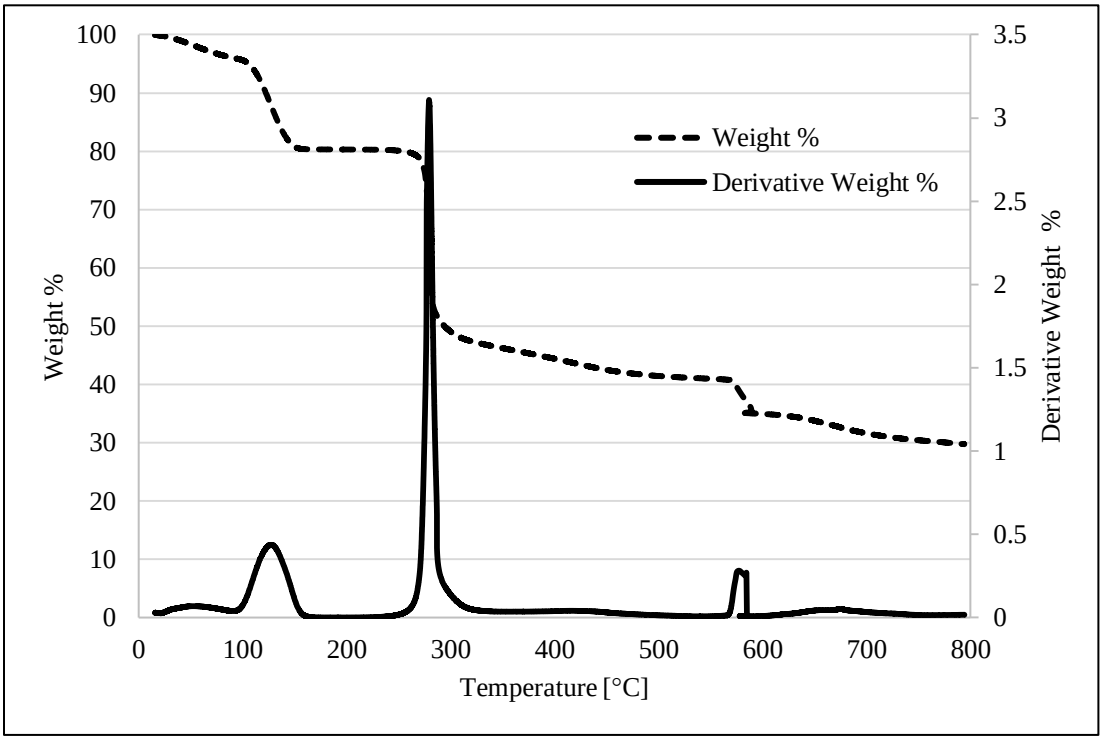

Figure B.6. Thermogravimetric profile of cornstarch mixed with sodium bicarbonate (1:1 ratio by weight). Increase in temperature, from room temperature to 800 °C, at a constant 10 °C/min heating rate (in air).

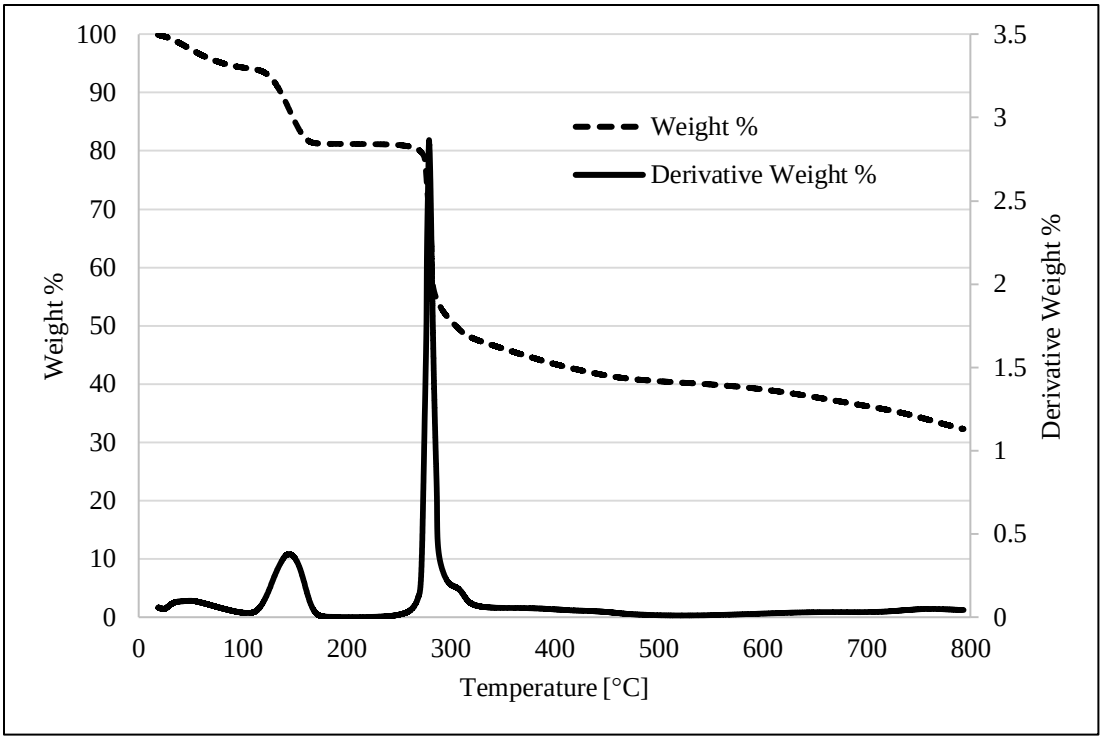

Figure B.7. Thermogravimetric profile of cornstarch mixed with potassium bicarbonate (1:1 ratio by weight). Increase in temperature, from room temperature to 800 °C, at a constant 10 °C /min heating rate (in air).

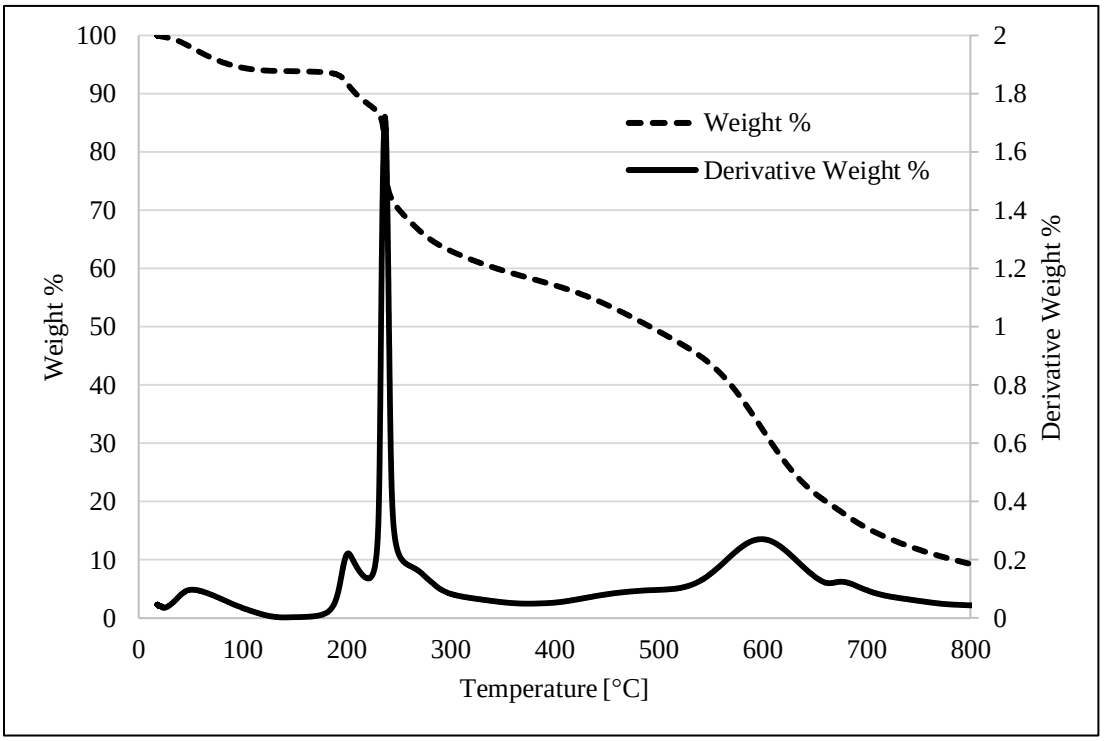

Figure B.8. Thermogravimetric profile of cornstarch mixed with monoammonium phosphate (1:1 ratio by weight). Increase in temperature, from room temperature to 800 °C, at a constant 10 °C /min heating rate (in air).

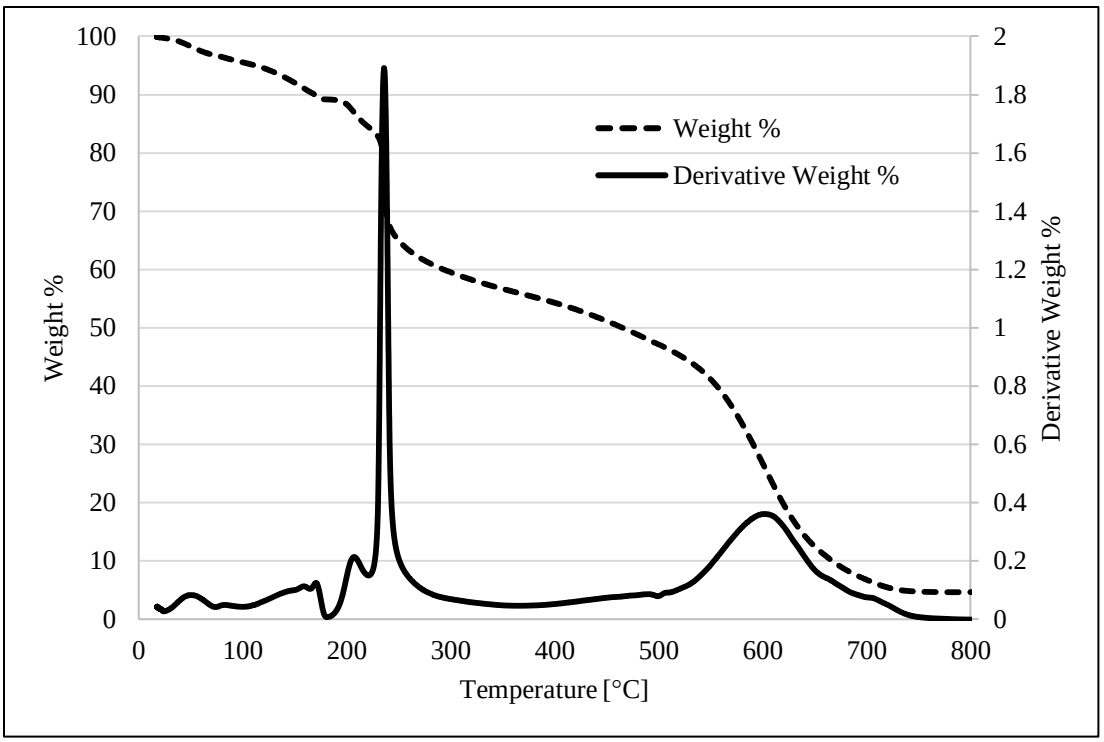

Figure B.9. Thermogravimetric profile of cornstarch mixed with diammonium phosphate (1:1 ratio by weight). Increase in temperature, from room temperature to 800 °C, at a constant 10 °C /min heating rate (in air).

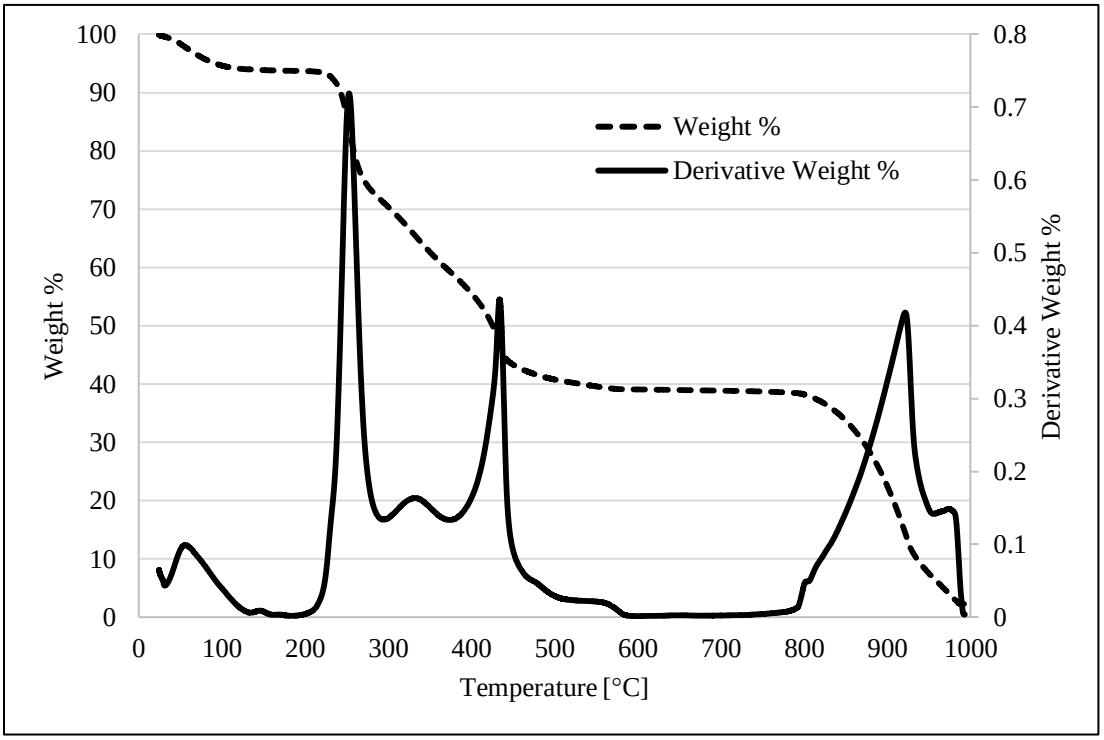

Figure B.10. Thermogravimetric profile of cornstarch mixed with Met-L-X (1:1 ratio by weight). Increase in temperature, from room temperature to 1000 °C, at a constant 10 °C /min heating rate (in air).

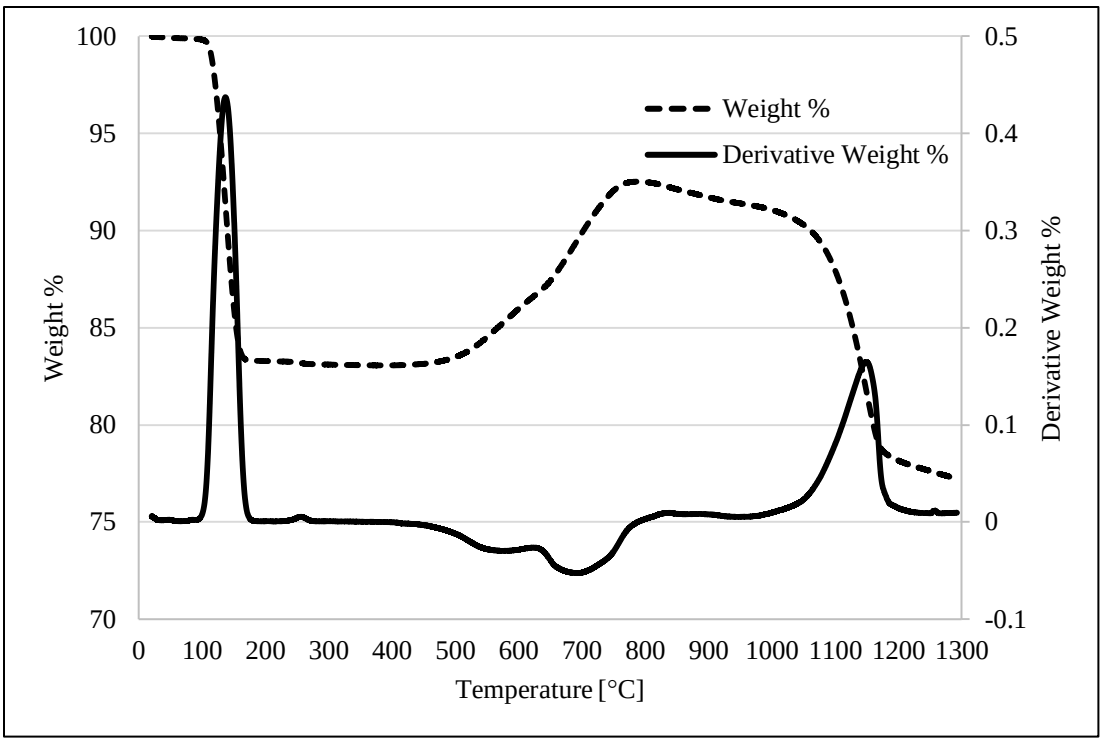

Figure B.11. Thermogravimetric profile of zinc powder mixed with sodium bicarbonate (1:1 ratio by weight). Increase in temperature, from room temperature to 1300 °C, at a constant 10 °C /min heating rate (in air).

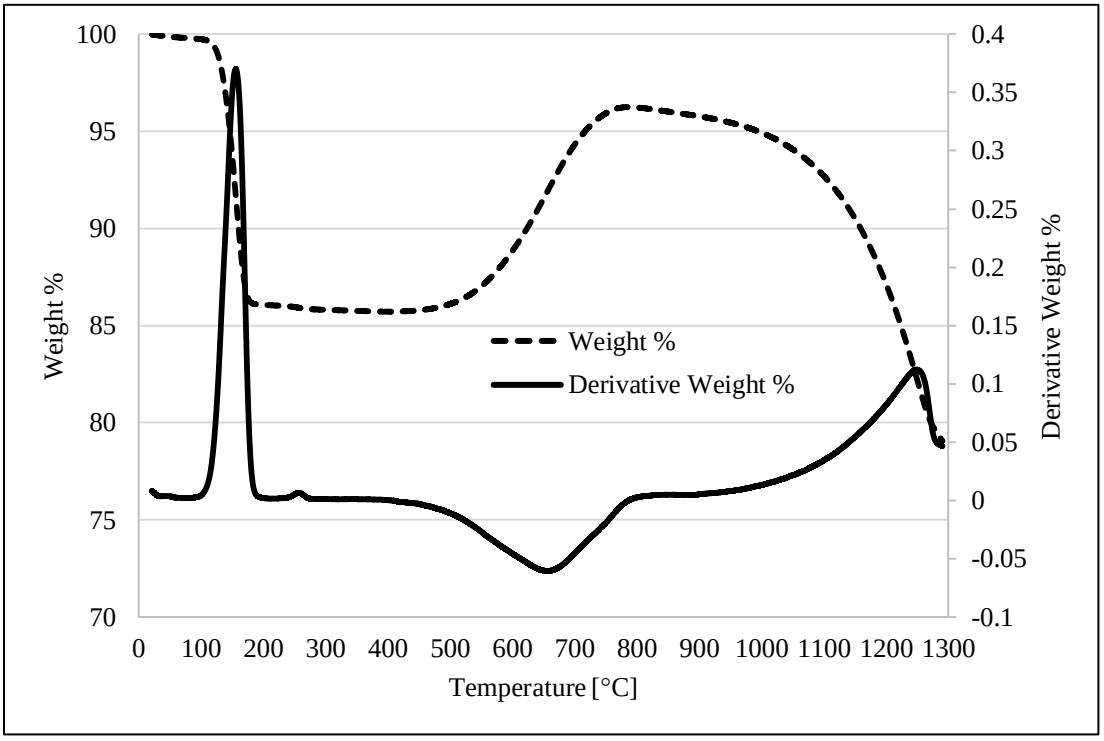

Figure B.12. Thermogravimetric profile of zinc powder mixed with potassium bicarbonate (1:1 ratio by weight). Increase in temperature, from room temperature to 1300 °C, at a constant 10 °C /min heating rate (in air).

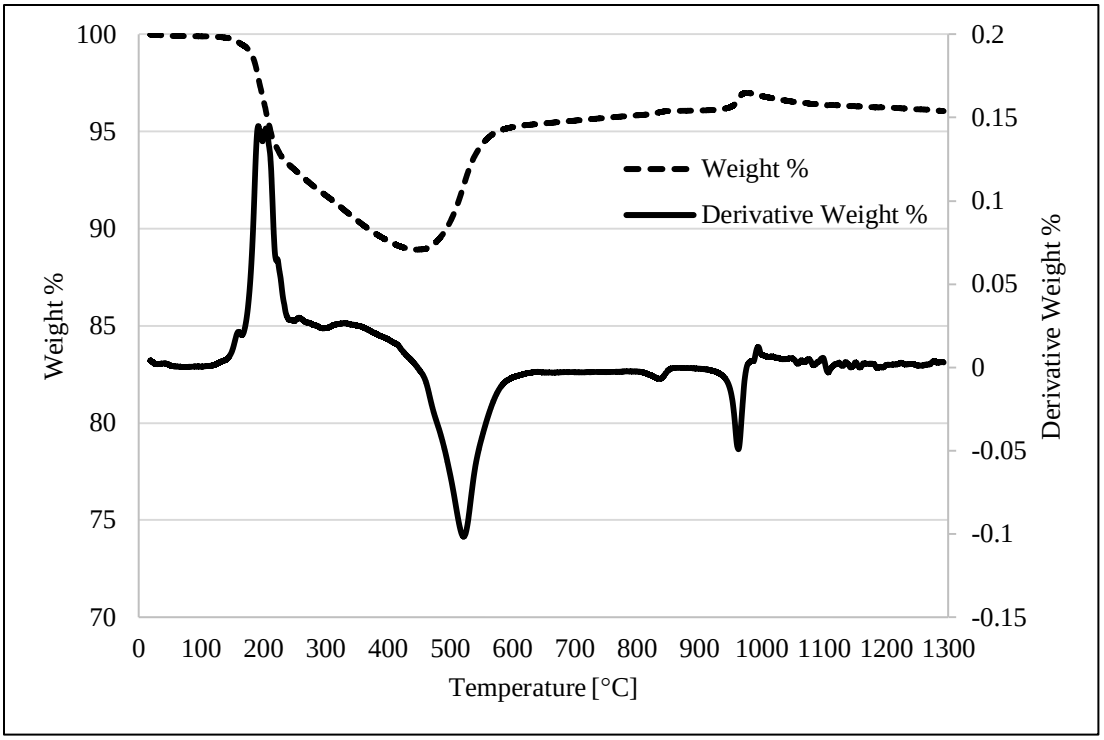

Figure B.13. Thermogravimetric profile of zinc powder mixed with monoammonium phosphate (1:1 ratio by weight). Increase in temperature, from room temperature to 1300 °C, at a constant 10 °C /min heating rate (in air).

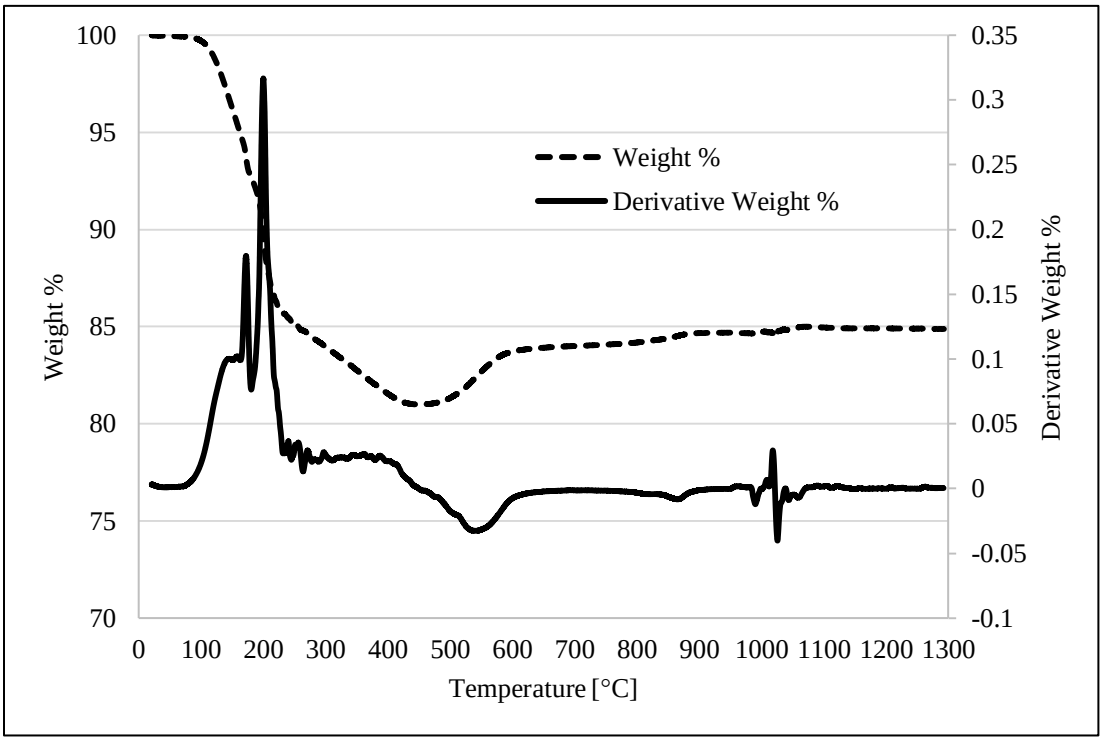

Figure B.14. Thermogravimetric profile of zinc powder mixed with diammonium phosphate (1:1 ratio by weight). Increase in temperature, from room temperature to 1300 °C, at a constant 10 °C /min heating rate (in air).

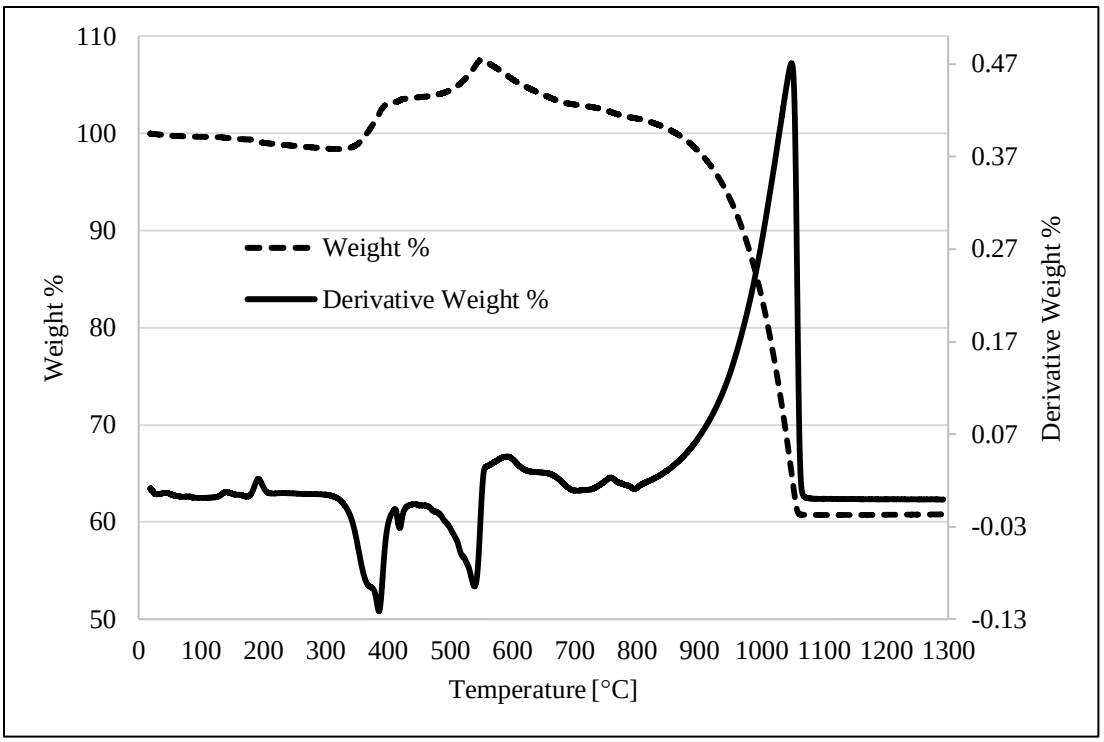

Figure B.15. Thermogravimetric profile of zinc powder mixed with Met-L-X (1:1 ratio by weight). Increase in temperature, from room temperature to 1300 °C, at a constant 10 °C /min heating rate (in air).

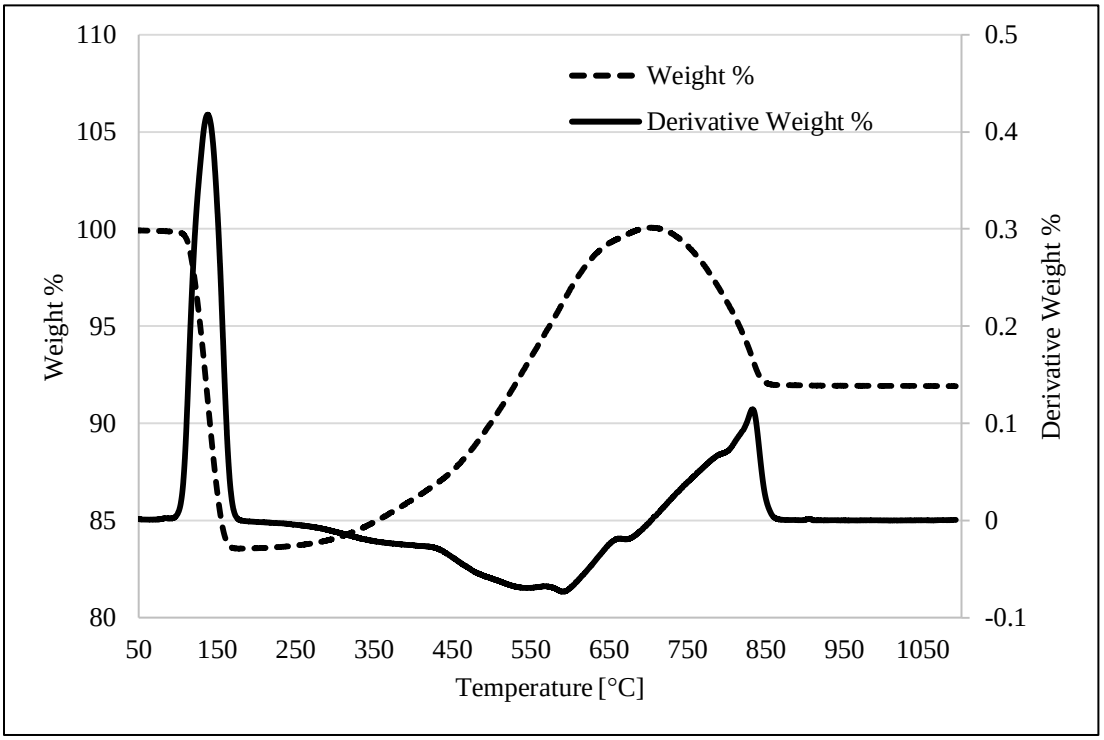

Figure B.16. Thermogravimetric profile of iron powder mixed with sodium bicarbonate (1:1 ratio by weight). Increase in temperature, from 50 to 1100 °C, at a constant 10 °C /min heating rate (in air).

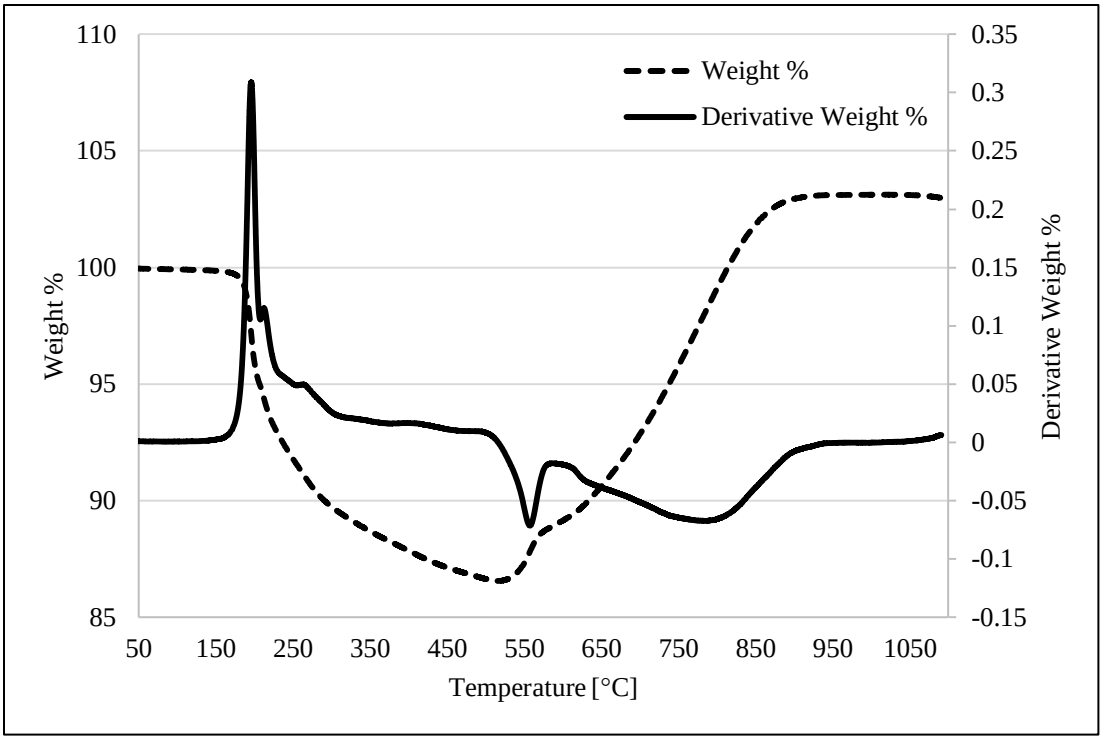

Figure B.17. Thermogravimetric profile of iron powder mixed with monoammonium phosphate (1:1 ratio by weight). Increase in temperature, from 50 to 1100 °C, at a constant 10 °C /min heating rate (in air).

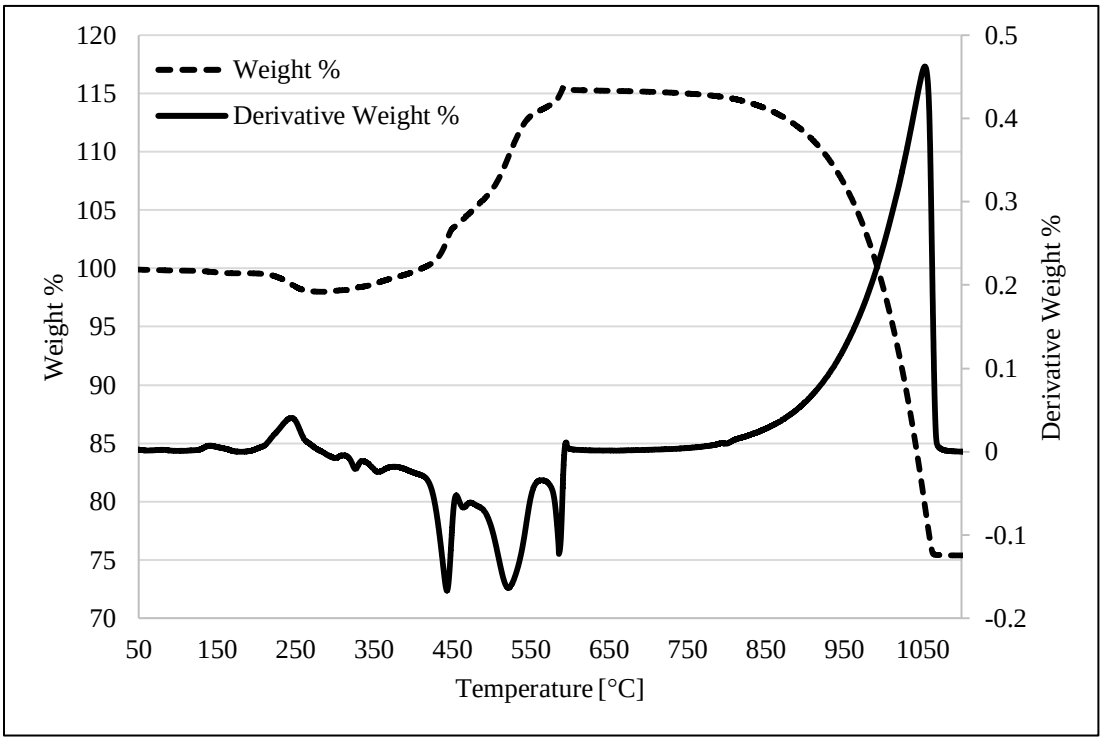

Figure B.18. Thermogravimetric profile of iron powder mixed with Met-L-X (1:1 ratio by weight). Increase in temperature, from 50 to 1100 °C, at a constant 10 °C /min heating rate (in air).

Appendix C: DSC Profiles for All Inhibitors and 1:1 Fuel/Inhibitor Mixtures

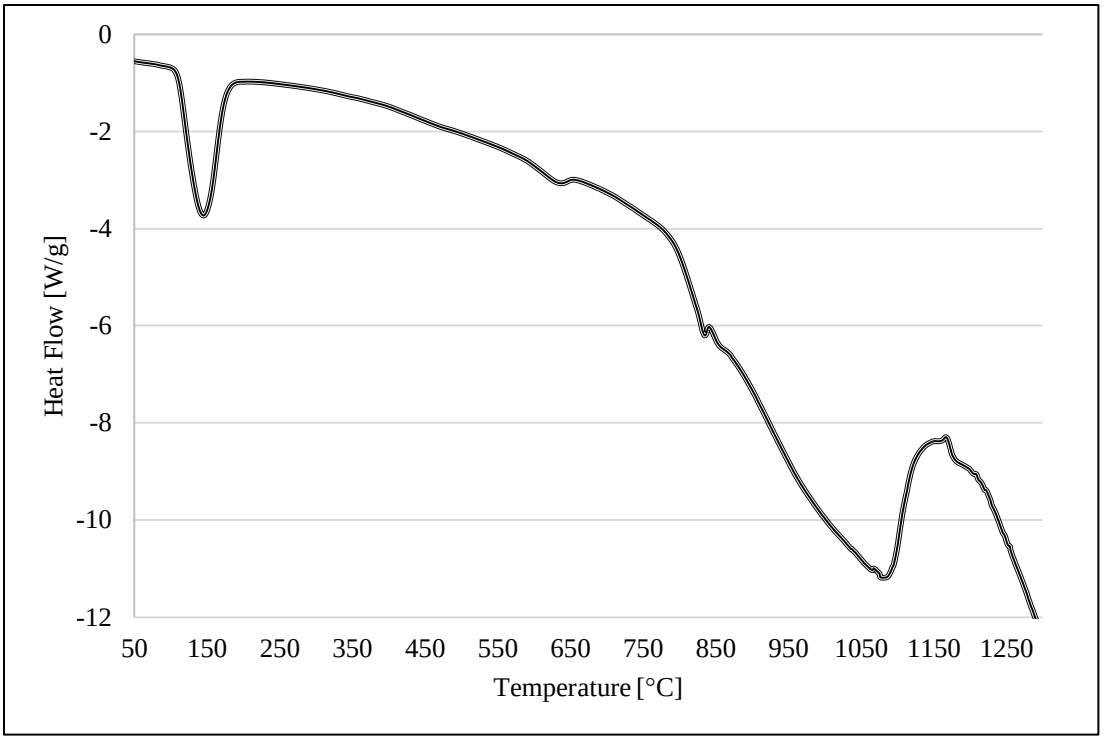

Figure C.1. Differential scanning calorimetry profile for sodium bicarbonate. Increase in temperature, from 50 to 1300 °C, at a constant 10 °C/min heating rate (in air).

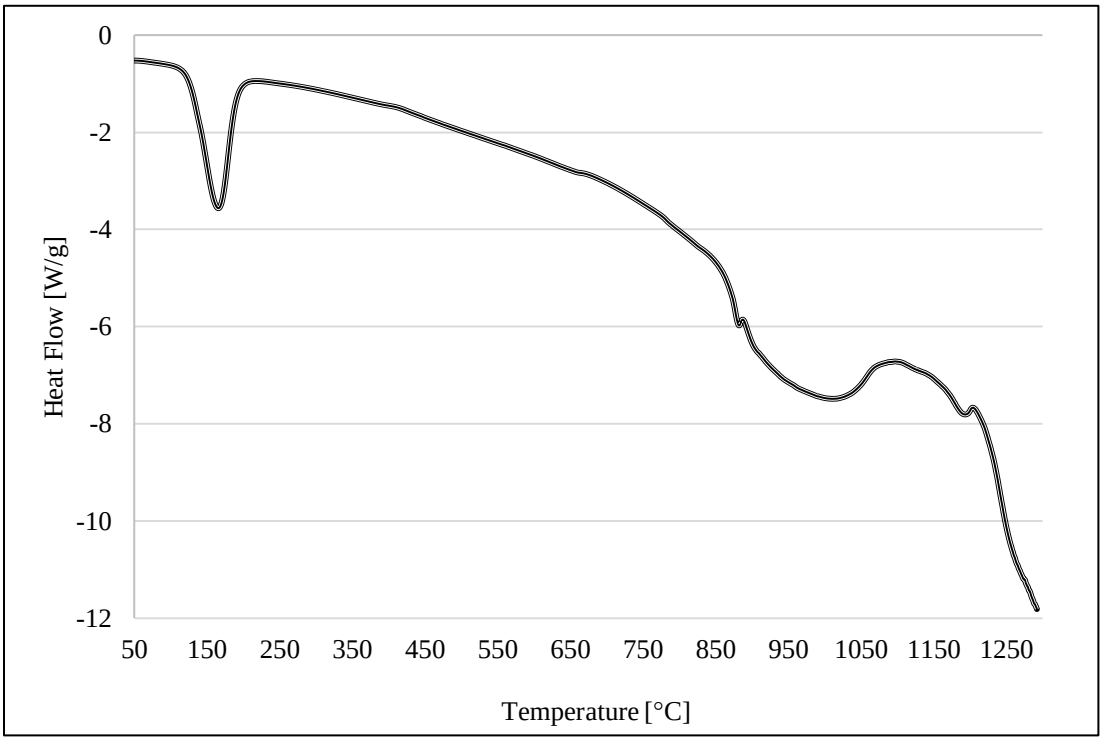

Figure C.2. Differential scanning calorimetry profile for potassium bicarbonate. Increase in temperature, from 50 to 1300 °C, at a constant 10 °C/min heating rate (in air).

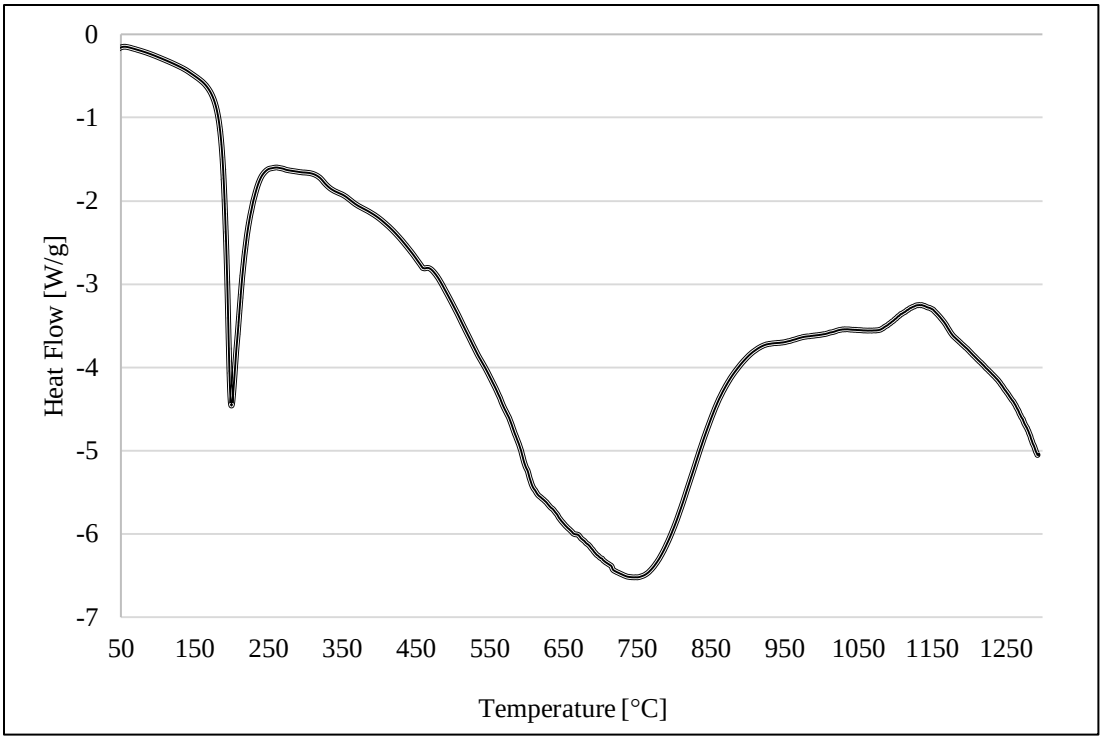

Figure C.3. Differential scanning calorimetry profile for monoammonium phosphate. Increase in temperature, from 50 to 1300 °C, at a constant 10 °C/min heating rate (in air).

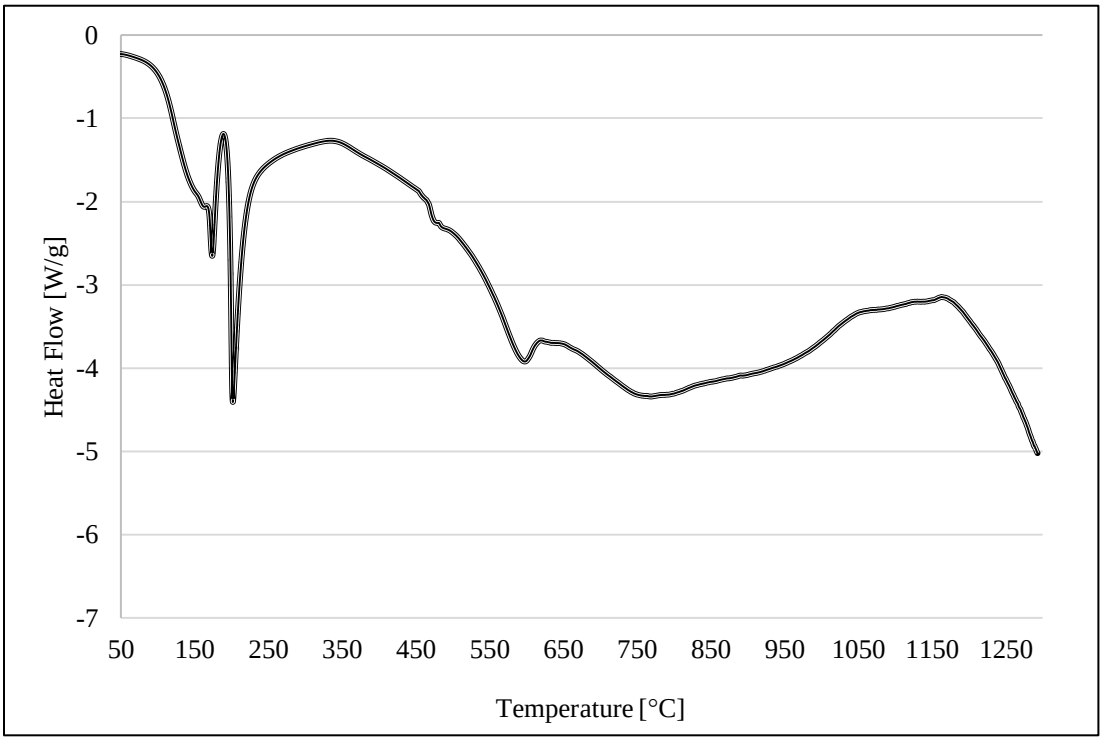

Figure C.4. Differential scanning calorimetry profile for diammonium phosphate. Increase in temperature, from 50 to 1300 °C, at a constant 10 °C/min heating rate (in air).

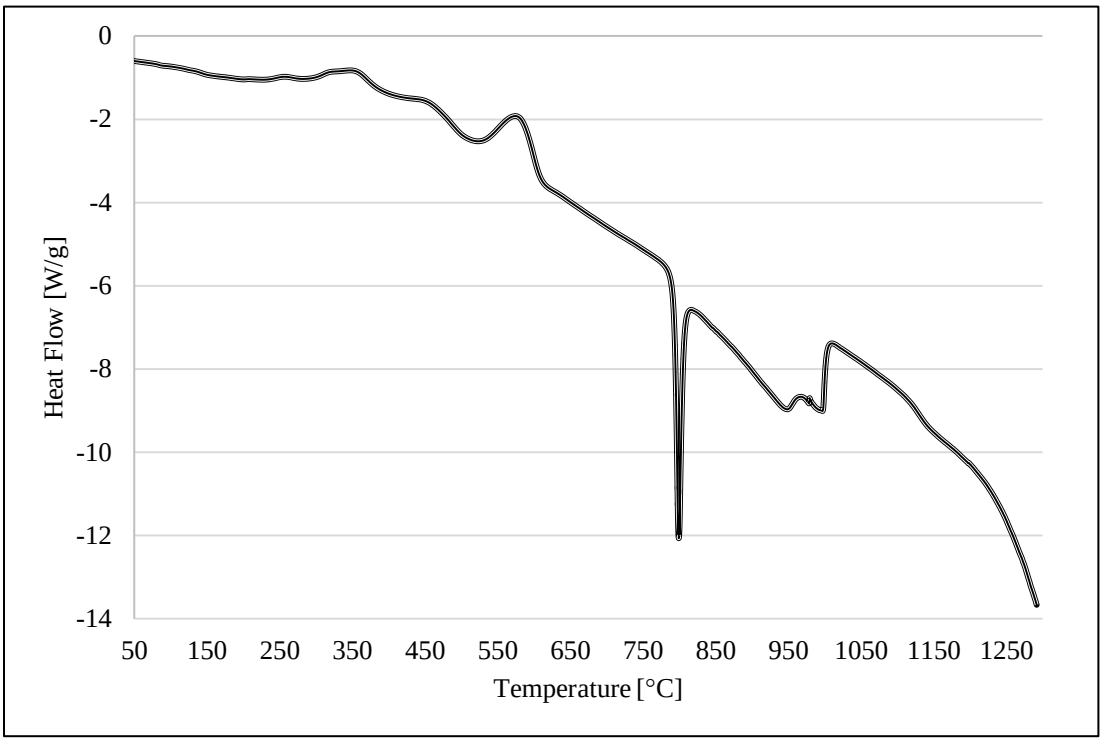

Figure C.5. Differential scanning calorimetry profile for Met-L-X. Increase in temperature, from 50 to 1300 °C, at a constant 10 °C/min heating rate (in air).

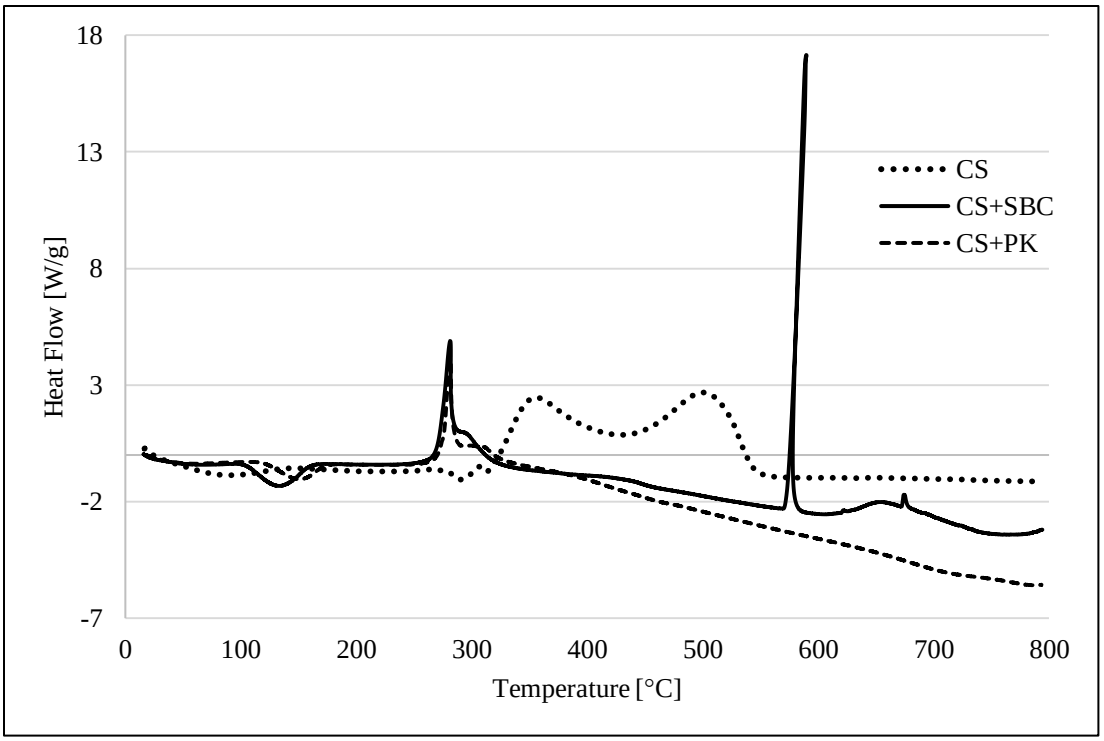

Figure C.6. Differential scanning calorimetry profile for cornstarch and cornstarch/carbonate inhibitor mixtures. Increase in temperature, from room temperature to 800 °C, at a constant 10 °C/min heating rate (in air).

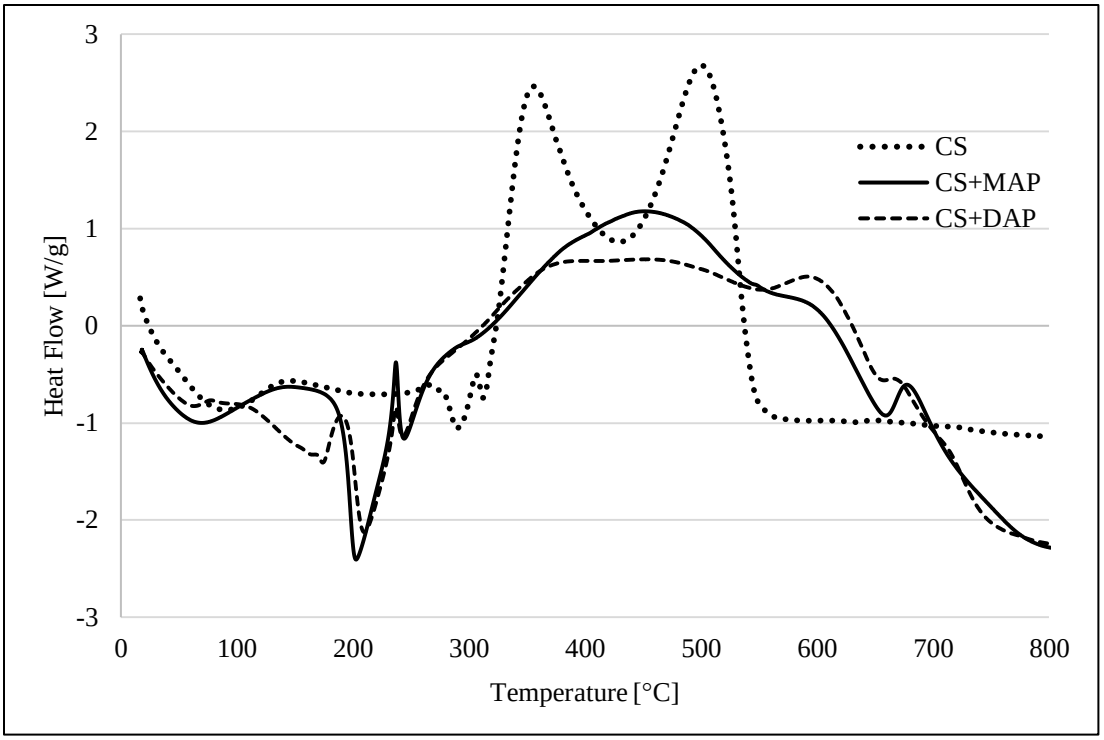

Figure C.7. Differential scanning calorimetry profile for cornstarch and cornstarch/phosphate inhibitor mixtures. Increase in temperature, from room temperature to 800 °C, at a constant 10 °C/min heating rate (in air).

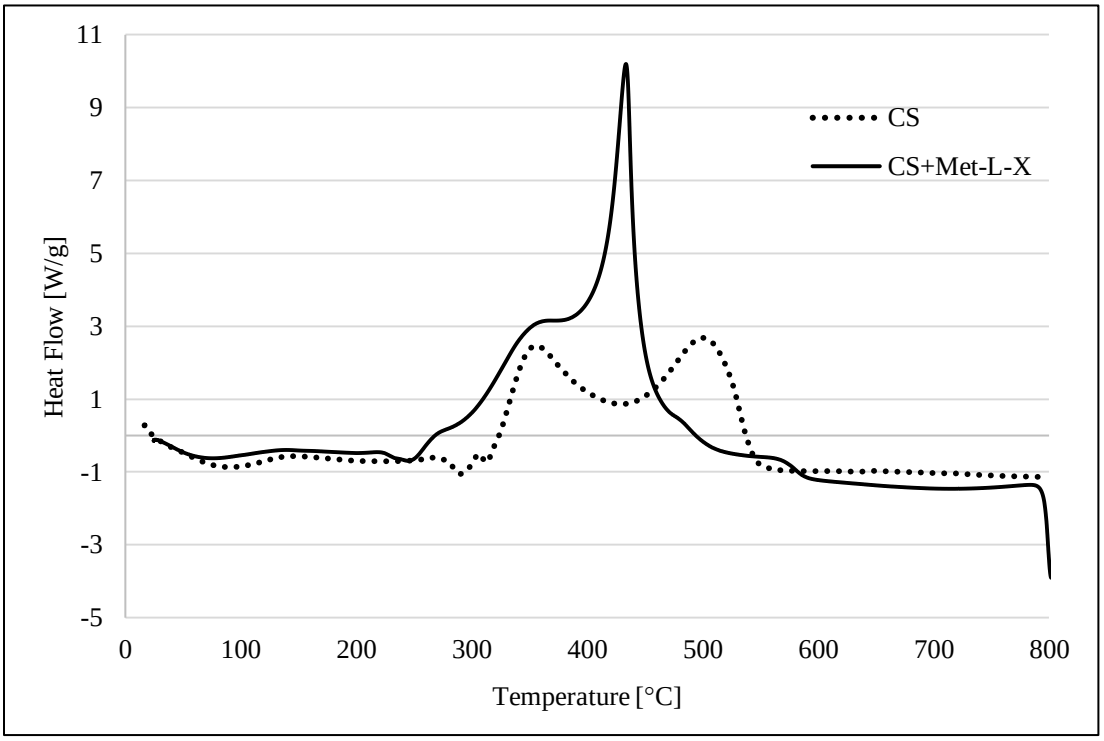

Figure C.8. Differential scanning calorimetry profile for cornstarch and cornstarch/Met-L-X inhibitor mixture. Increase in temperature, from room temperature to 800 °C, at a constant 10 °C/min heating rate (in air).

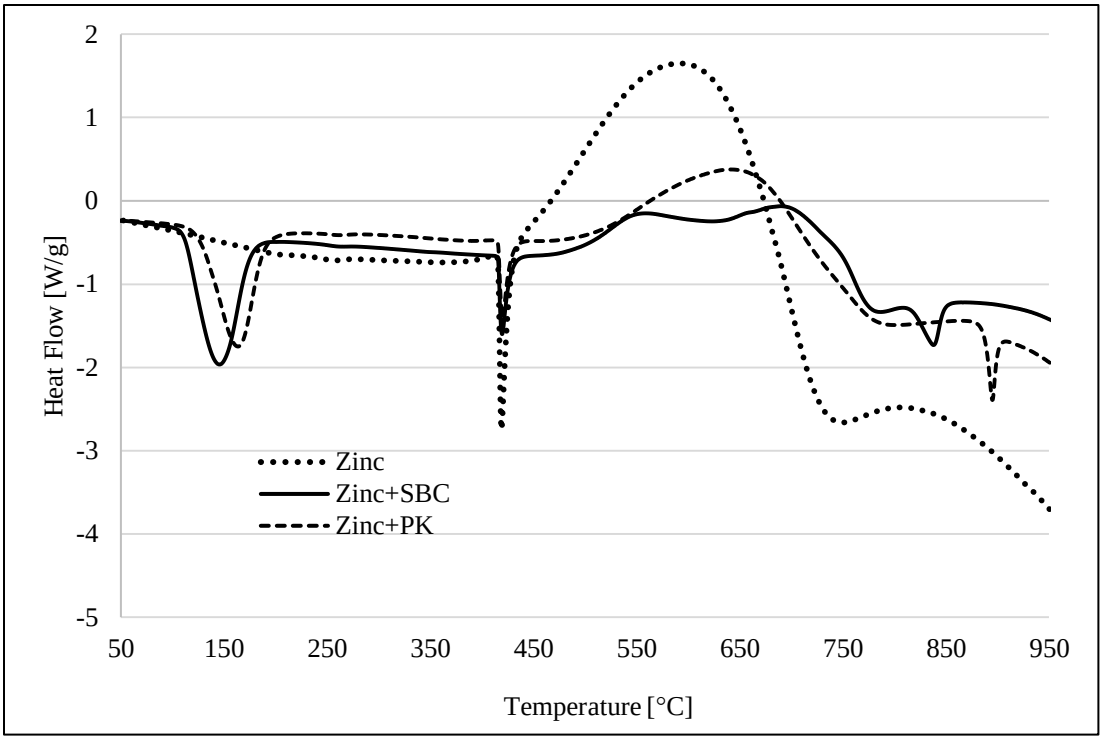

Figure C.9. Differential scanning calorimetry profile for zinc powder and zinc/carbonate inhibitor mixtures. Increase in temperature, from 50 to 950 °C, at a constant 10 °C/min heating rate (in air).

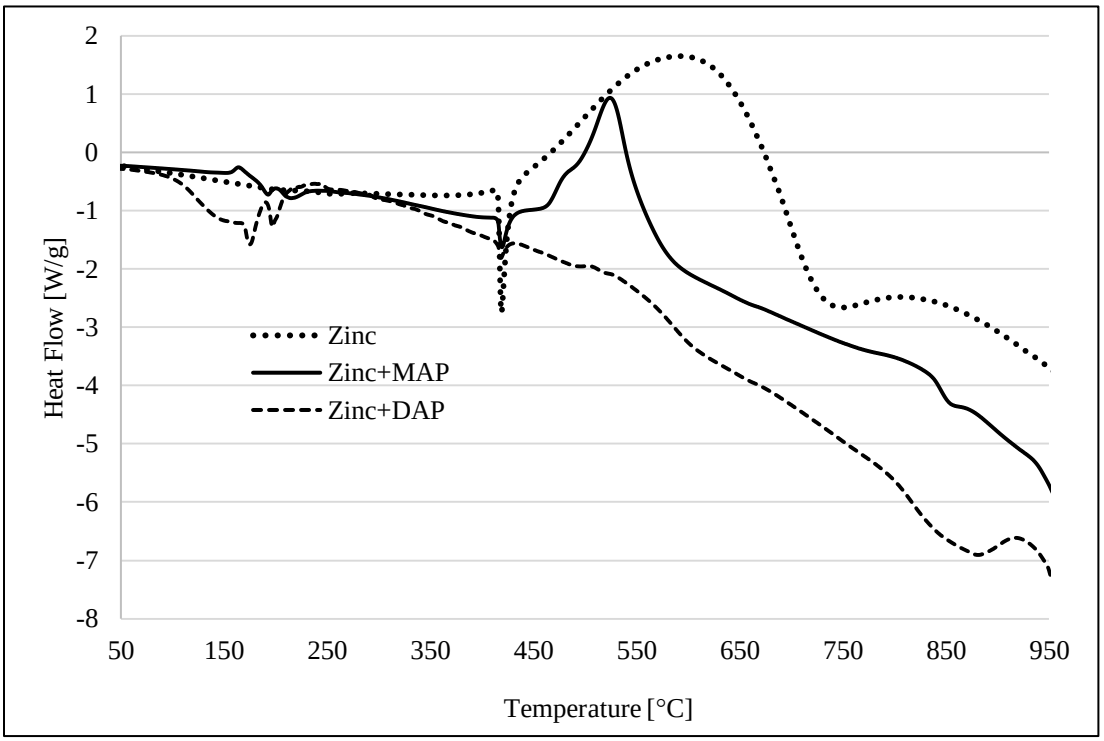

Figure C.10. Differential scanning calorimetry profile for zinc powder and zinc/phosphate inhibitor mixtures. Increase in temperature, from 50 to 950 °C, at a constant 10 °C/min heating rate (in air).

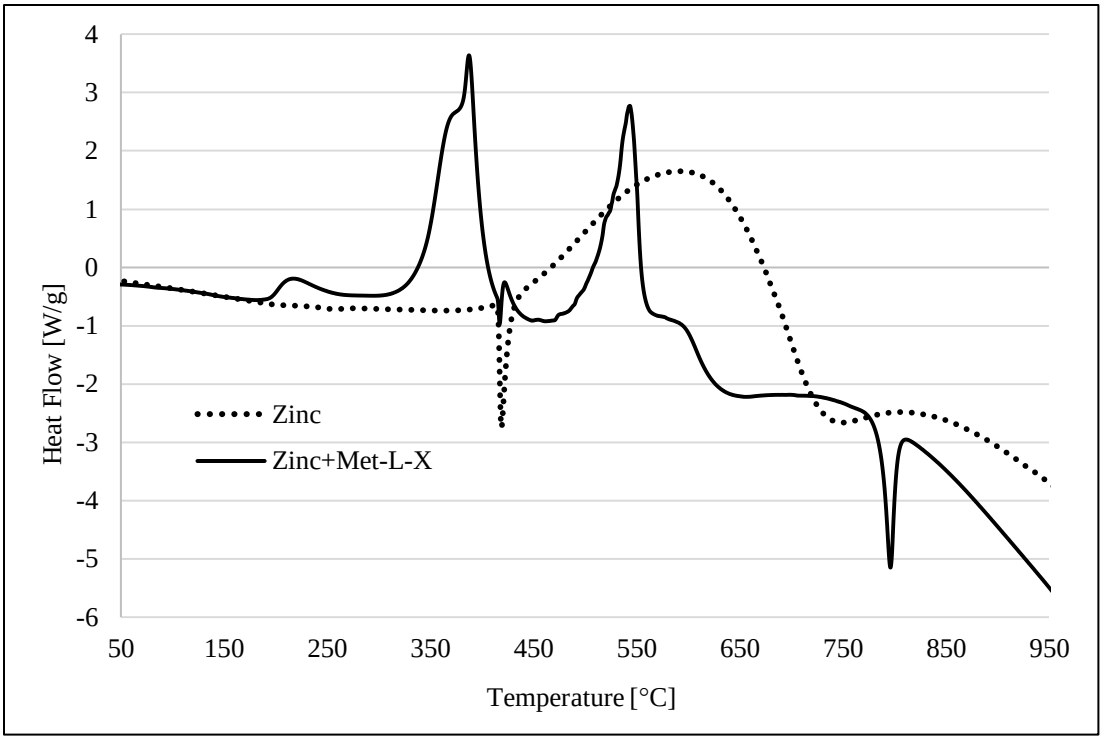

Figure C.11. Differential scanning calorimetry profile for zinc powder and zinc/Met-L-X inhibitor mixture. Increase in temperature, from 50 to 950 °C, at a constant 10 °C/min heating rate (in air).

Table C.1. Total heat released during decomposition of cornstarch and cornstarch/inhibitor mixtures; normalized integration of Figures C.6, C.7, and C.8, from room temperature to 800 °C.

Fuel/Inhibitor Mixture	Normalized DSC Curve Area [J/g]	Average Normalized Deviation [J/g]
CS	659	41
CS+SBC	-184	1
CS+PK	-850	139
CS+MAP	528	1
CS+DAP	681	194
CS+Met-L-X	986	61

Table C.2. Total heat released during decomposition of zinc powder and zinc/inhibitor mixtures; integration of Figures C.9, C.10, and C.11 over the zinc liquid-phase combustion range (400 to 750 °C).

Fuel/Inhibitor Mixture	Σ(Peak Areas within Combustion Range) [J/g]	Average Deviation [J/g]
Zn	3617	433
Zn+SBC	1149	14
Zn+PK	1342	49
Zn+MAP	806	84
Zn+DAP	203	46
Zn+Met-L-X	1243	41

Appendix D: Suppressant Agent Evolved Gas Analysis via Mass Spectrometry

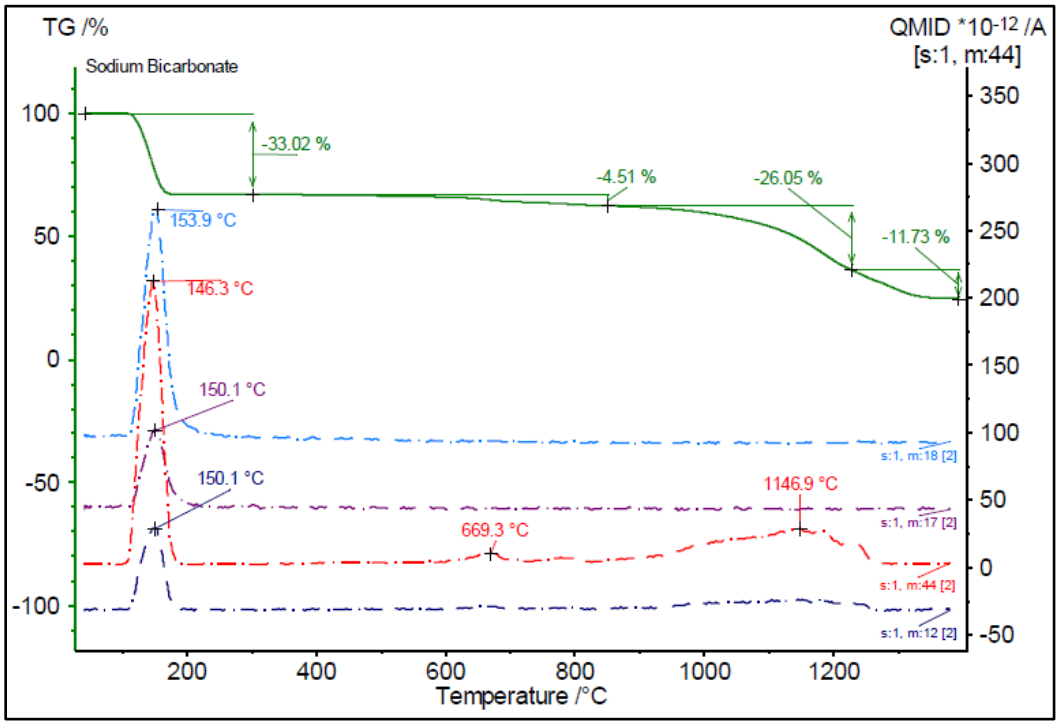

Figure D.1. TGA and MS ion-current curves for mass numbers 12, 17, 18, and 44 in SBC sample, heated from 40 to 1400 °C at 10 °C/min (in air).

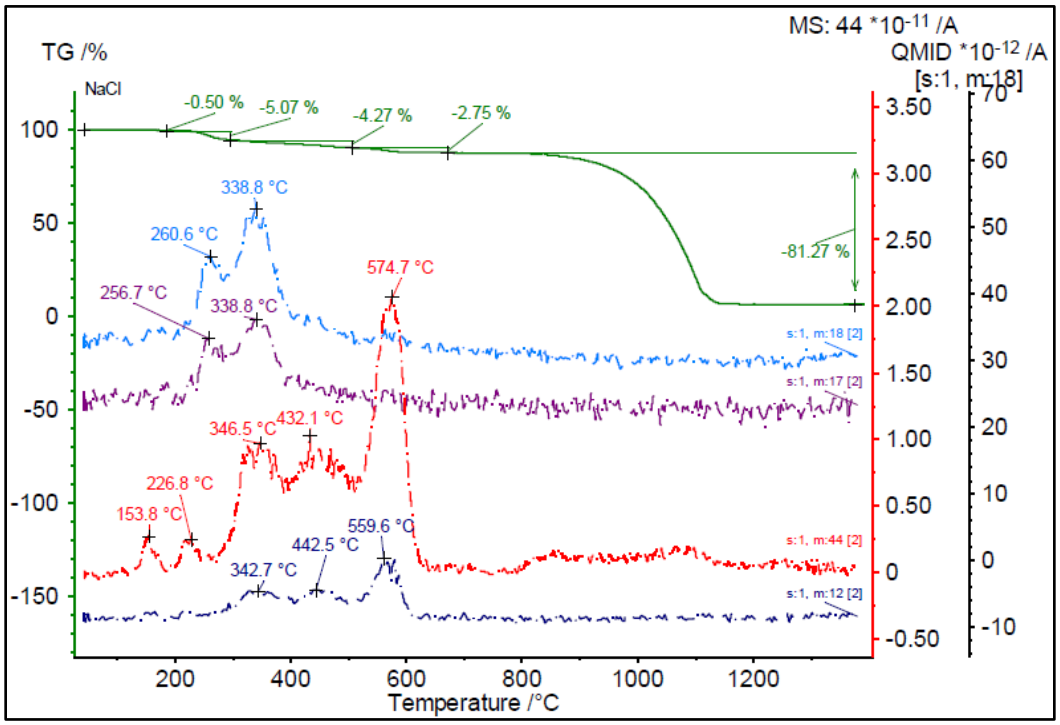

Figure D.2. TGA and MS ion-current curves for mass numbers 12, 17, 18, and 44 in Met-L-X sample, heated from 40 to 1400 °C at 10 °C/min (in air).

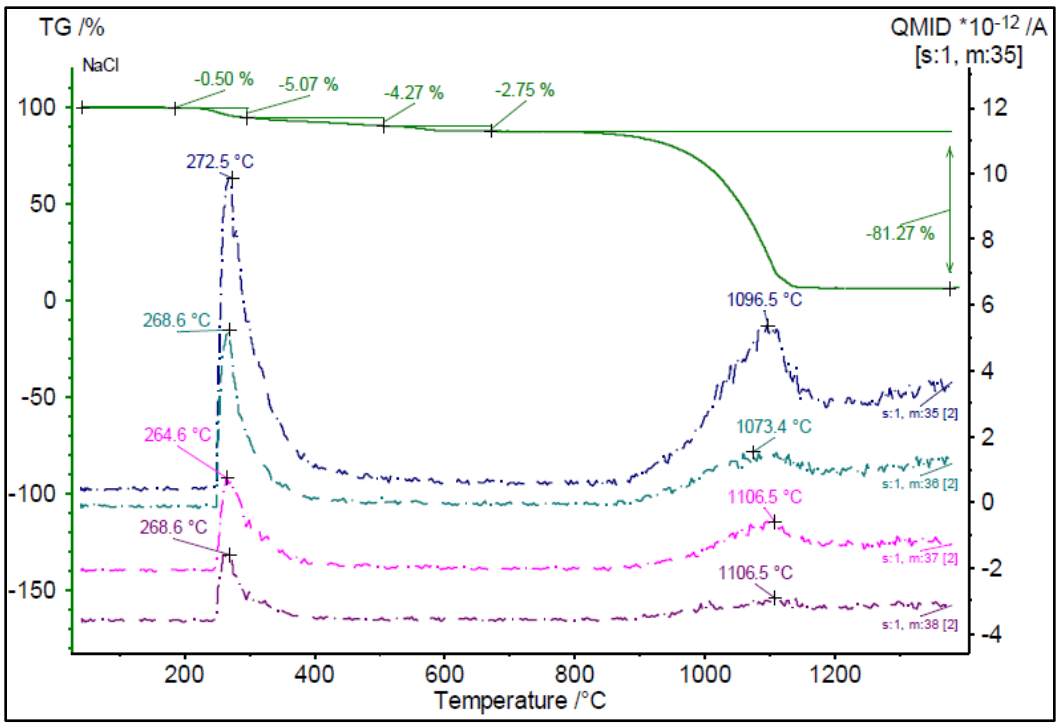

Figure D.3. TGA and MS ion-current curves for mass numbers 35, 36, 37, and 38 in Met-L-X sample, heated from 40 to 1400 °C at 10 °C/min (in air).

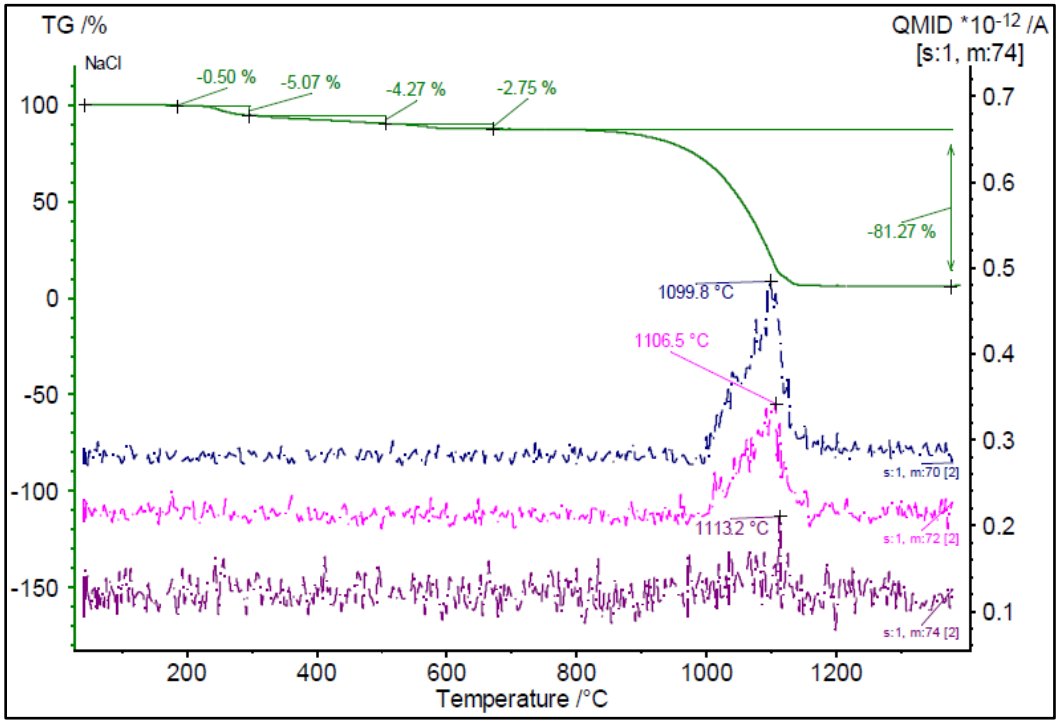

Figure D.4. TGA and MS ion-current curves for mass numbers 70, 72, and 74 in Met-L-X sample, heated from 40 to 1400 °C at 10 °C/min (in air).

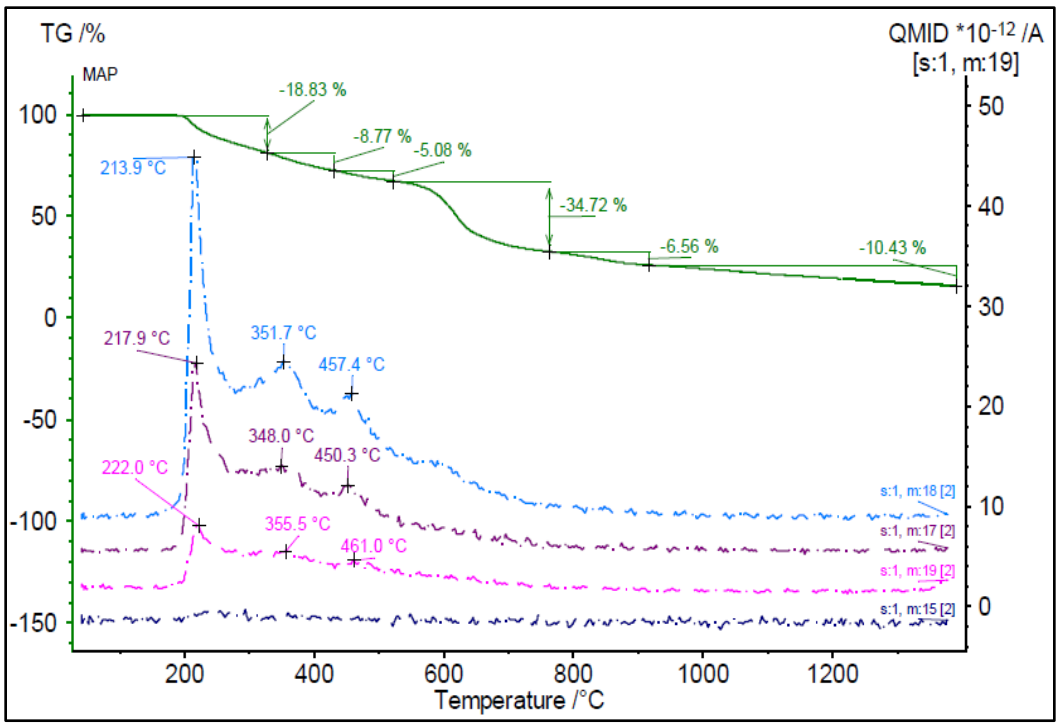

Figure D.5. TGA and MS ion-current curves for mass numbers 15, 17, 18, and 19 in MAP sample, heated from 40 to 1400 °C at 10 °C/min (in air).

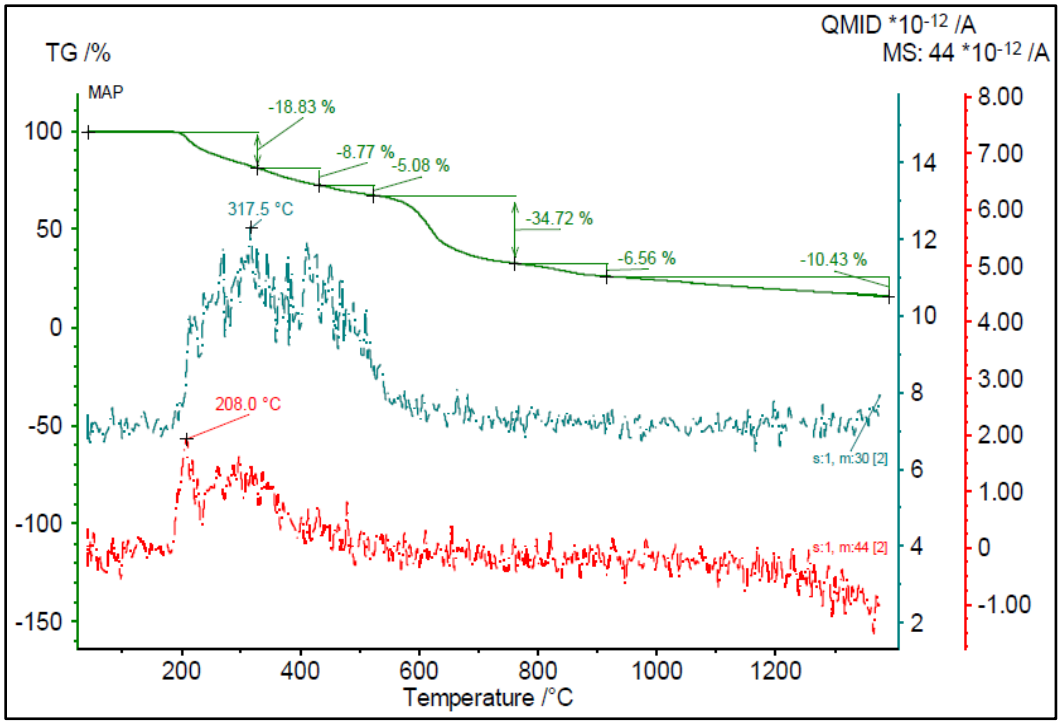

Figure D.6. TGA and MS ion-current curves for mass numbers 30 and 44 in MAP sample, heated from 40 to 1400 °C at 10 °C/min (in air).

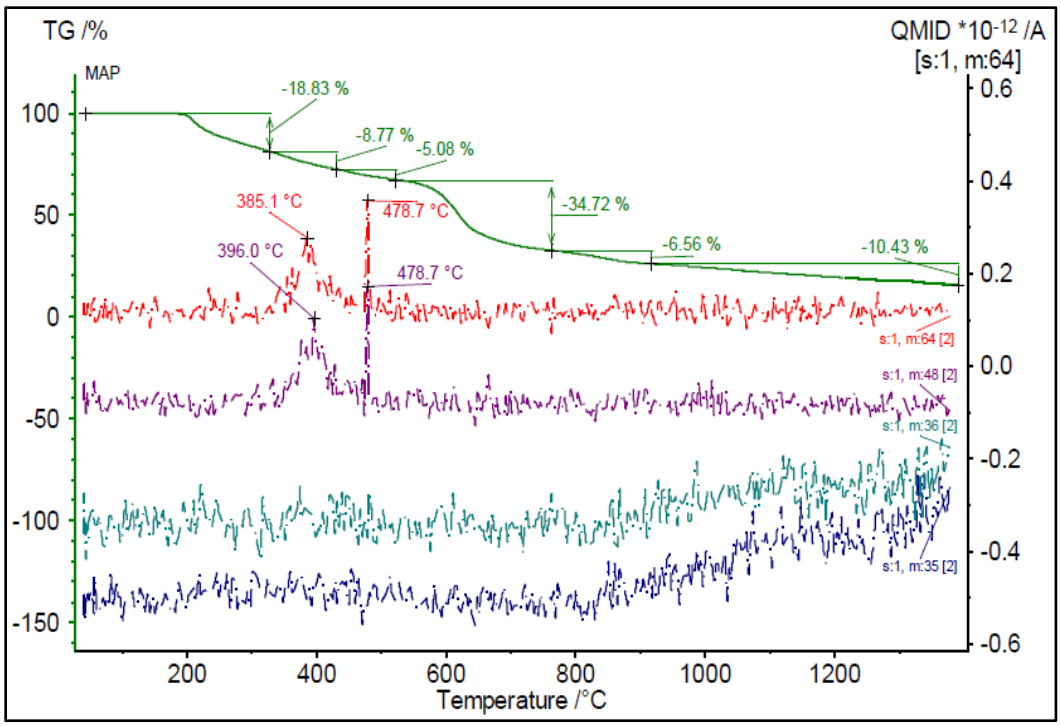

Figure D.7. TGA and MS ion-current curves for mass numbers 35, 36, 48, and 64 in MAP sample, heated from 40 to 1400 °C at 10 °C/min (in air).

Appendix E: Open-Air Dispersion Data

Table E.1. Measured packed densities for all three suppressant agents, and agent fill weights during open-air dispersion testing.

Suppressant Material	Packed Density (kg/L)	Agent Fill Weight (kg)
SBC	1.33	9.07
Met-L-X	0.89	5.90
MAP	0.63	4.08

Table E.2. Average inverse velocity measurements (in imperial units for open-air dispersion testing, reported exclusively along the central plume axis (Track Point 2) with respect to previous frame (instantaneous) and custom origin (bulk) reference states.

	SBC (Test 1 & 1-R1, AVG)		Met-L-X (Test 2 & 2-R1, AVG)		MAP (Test 3 & 3-R1, AVG)	
	Instantaneous Inverse Velocity	Bulk Inverse Velocity	Instantaneous Inverse Velocity	Bulk Inverse Velocity	Instantaneous Inverse Velocity	Bulk Inverse Velocity
Target Throw Distance (ft)	Inverse Velocity (ms/ft)	Inverse Velocity (ms/ft)	Inverse Velocity (ms/ft)	Inverse Velocity (ms/ft)	Inverse Velocity (ms/ft)	Inverse Velocity (ms/ft)
3	1.95	1.88	2.10	1.93	1.86	1.81
6	5.50	3.11	5.76	3.20	8.12	3.38
9	7.81	4.99	7.39	4.55	10.45	5.13
12	7.65	5.44	8.64	5.48	11.24	6.71
15	8.89	5.96	9.87	6.27	16.81	7.64